



**University of
Zurich**^{UZH}

Detection of floating plastic waste using imaging spectroscopy

GEO 511 Master's Thesis

Author

Sonja Bertschi
10-739-860

Supervised by

Dr. Andreas Hüni

Faculty representative

Prof. Dr. Michael Schaepman

29.09.2019

Department of Geography, University of Zurich



**University of
Zurich** ^{UZH}

Detection of floating plastic waste using imaging spectroscopy

GEO 511 Master's Thesis

Author

Sonja Bertschi
10-739-860

Supervised by

Dr. Andreas Hüni

Faculty representative

Prof. Dr. Michael Schaepman

29.09.2019

Department of Geography, University of Zurich



**University of
Zurich** ^{UZH}

Detection of floating plastic waste using imaging spectroscopy

GEO 511 MASTER'S THESIS

Author:

Sonja BERTSCHI

10-739-860

Supervised by:

Dr. Andreas HUENI

Faculty representative:

Prof. Dr. Michael SCHAEPMAN

29th September 2019

Department of Geography, University of Zurich

ABSTRACT

Is it possible to optically detect floating ocean plastic debris from space – or perhaps from data acquired by sensors on airborne platforms several thousand meters above the water surface? Ocean plastic waste is an exponentially increasing environmental issue at global scale, yet current knowledge about its quantity and distribution is principally based on projections and estimates from oceanographic modelling.

Knowing exactly, based on actual measurements, where and how much plastic waste is drifting at sea would be a compelling piece of information for the public and, with regard to mitigation efforts, for clean-up operations and policymakers alike. The European Space Agency (ESA) is currently investigating this research question, and first scientific studies on the subject have been published recently. These studies refer to the field of remote sensing, which is the only one regarded to have potential in monitoring the oceans in real time and to provide the relevant information.

One of the approaches in the field is considered in this paper. It focuses on the passive remote sensing method of imaging spectroscopy. An explorative approach is applied to investigate the conditions under which floating PET bottles can be detected in spectral imagery and, if at all possible, identified. The research questions asked relate to fundamental detectability limits such as the surface density of the floating plastic and the spatial and most importantly spectral resolution requirements for imaging sensors. However, no suitable data were available at the onset of the project, and in order to obtain meaningful imagery for the planned investigations, an experiment with 492 PET bottles was carried out on Swiss lakes during the 2018 flight mission period. Several image analysis and classification approaches were applied to the acquired data from both the APEX and AVIRIS-NG imaging spectroscopy sensors. The chosen methods essentially cover three selected elements of data comparison: spectral similarity (e.g., SAM), specific spectral absorption features of plastic materials (e.g., Indices, CR), and sub-pixel information extraction based on spectral mixture analysis for abundance estimation.

Our results, achieved for the first time for small surface fractions of floating plastic under real conditions, allow to significantly lower and narrow the detection limit range based on laboratory data and documented in the research literature: A surface fraction of less than 1% plastic can be distinguished from the surrounding water in imaging spectroscopy data. Furthermore, small plastic proportions (1%, 2.5%, and 5%) were classified, however not unambiguously. Significantly higher signal components of the sought plastic material seem to be necessary for precise material identification.

In conclusion, it must be noted that the evaluated data of the experimental test areas were primarily oriented towards technical feasibility rather than real ocean conditions. Insofar, the technical feasibility of identifying and monitoring floating plastic debris in the ocean is considered to be appropriate in principle, although it may only be applicable to extremely high waste concentrations and under optimal conditions.

ZUSAMMENFASSUNG

Ist es möglich, schwimmenden Plastikmüll auf den Weltmeeren aus dem Weltraum - oder von Daten, die durch Sensoren in Flugzeugen mehrere tausend Meter über der Wasseroberfläche erfasst werden - zu erkennen? Plastikmüll im Meer ist ein globales und exponentiell wachsendes Umweltproblem, doch der heutige Kenntnisstand über Menge und Verbreitung basiert grösstenteils auf Daten, die auf Hochrechnungen und ozeanographische Strömungsmodelle zurückzuführen sind.

Genau zu wissen, wo wieviel Plastikmüll im Meer treibt, wäre eine wichtige Information für die Öffentlichkeit und politische Entscheidungsträger gleichermaßen. Die Europäische Weltraumorganisation ESA geht aktuell dieser Forschungsfrage nach, und erste wissenschaftliche Studien sind in den letzten Jahren dazu publiziert worden. Diese beziehen sich auf den Fachbereich der Fernerkundung, welchem als einzigem das Potential zur Beantwortung dieser Frage zugeschrieben wird.

In dieser Arbeit wird auf eine dieser Fernerkundungsmethoden fokussiert: auf die passive Methode der Bildspektroskopie. Es wird mit einem explorativen Ansatz untersucht, unter welchen Rahmenbedingungen auf Gewässer schwimmende PET-Flaschen in hyperspektralen Bilddaten detektiert und allenfalls identifiziert werden können. Die gestellten Forschungsfragen beziehen sich auf grundsätzliche Detektionsgrenzwerte wie die Oberflächendichte des schwimmenden Plastiks, sowie auf räumliche und vor allem spektrale Auflösungsanforderungen an Sensoren. Allerdings gab es für die geplanten Untersuchungen keinerlei geeignete Daten. Im Rahmen der jährlichen Flugkampagnen wurde deshalb im Sommer 2018 mehrmals ein aufwändiges Experiment auf Schweizer Gewässern mit 492 PET-Flaschen durchgeführt. Für die Auswertungen wurden mehrere Bildanalyse- und Klassifikationsansätze auf die erlangten Bilddaten der hyperspektralen Fernerkundungssensoren APEX und AVIRIS-NG angewendet. Die gewählten methodischen Ansätze konzentrieren sich hauptsächlich auf drei Datenmerkmale: Spektrale Ähnlichkeit (z.B. SAM), spezifische spektrale Absorptionsmerkmale von Plastikmaterialien (z.B. Indizes, CR) und Schätzung von unterschiedlich geringen Plastikanteilen im Subpixel-Bereich (basierend auf spektraler Mischungsanalyse).

Die erstmalig unter realen Bedingungen erzielten Resultate ermöglichen es, den einzigen bisher in der Forschungsliteratur dokumentierten (und auf Labordaten basierenden) minimalen Detektionsbereich deutlich nach unten zu reduzieren und einzuschränken: Ein Plastik-Oberflächenanteil von unter 1 % ist in hyperspektralen Signalen vom umgebenden Wasser unterscheidbar. Im Weiteren konnte zwischen Plastikanteilen von 1 %, 2.5 % und 5 % unterschieden werden, allerdings nicht eindeutig. Für eine präzise Materialidentifikation scheinen jedoch deutlich höhere Signalanteile des gesuchten Materials nötig zu sein.

Es muss abschliessend festgehalten werden, dass sich die ausgewerteten Daten der experimentellen Testflächen vorwiegend an der technischen Machbarkeit und weniger an realen Bedingungen auf dem Meer orientierten. Insofern werden Identifikation und Monitoring von schwimmendem Plastikmüll zwar grundsätzlich als machbar angesehen, allerdings ist dies in der Praxis möglicherweise nur für extrem dichte Müllkonzentrationen und unter optimalen Rahmenbedingungen umsetzbar.

TABLE OF CONTENT

ABSTRACT	3
ZUSAMMENFASSUNG	4
TABLE OF CONTENT	5
LIST OF FIGURES	7
LIST OF TABLES	8
LIST OF ABBREVIATIONS	9
1 INTRODUCTION	11
1.1 Scientific background	11
1.1.1 Ocean plastic pollution	11
1.1.2 Quantification and localisation of floating plastic waste	13
1.1.3 Remote sensing approaches	16
1.2 Research questions and working hypothesis	18
2 DATA	19
2.1 Experimental design and setup	19
2.1.1 Experimental design and preparations.....	20
2.1.2 Deployment of floating plastic reference fields.....	21
2.1.3 Locations	23
2.2 Data acquisition and baseline processing	23
2.2.1 APEX airborne data	23
2.2.2 AVIRIS-NG airborne data.....	24
2.2.3 Sentinel-2 satellite data	25
2.2.4 Auxiliary data.....	25
2.3 Resulting data pool	26
3 METHODS	28
3.1 Data preprocessing and quality assessment	28
3.1.1 Data preprocessing.....	28
3.1.2 Initial image quality assessment	30
3.1.3 Data transformation	30
3.2 Basic image evaluation	31
3.2.1 Spectral and spatial profiles.....	33
3.2.2 Image enhancement approaches.....	33
3.2.3 Outline	34
3.3 Discrimination approaches	34
3.3.1 Clustering	36
3.3.2 Band ratioing and indexing	37
3.3.3 Supervised Classification.....	39
3.3.4 Outline	41
3.4 Plastic identification	42
3.4.1 Spectral Angle Mapper	43
3.4.2 Continuum Removal	44
3.4.3 Spectral Mixture Analysis	46
3.4.4 Outline	47
3.5 Spectroscopic models	47
3.5.1 Spectral mixing model	47
3.5.2 Spatial scaling.....	48

4	RESULTS	49
4.1	Data preprocessing and quality assessment	49
4.1.1	Data preprocessing	49
4.1.2	Initial image quality assessment	49
4.1.3	Data transformation	50
4.2	Basic image evaluation	51
4.2.1	Spectral and spatial profiles	51
4.2.2	Image enhancement approaches	53
4.3	Discrimination approaches	54
4.3.1	Clustering	54
4.3.2	Band ratioing and indexing	57
4.3.3	Supervised Classification	58
4.4	Plastic identification	60
4.4.1	Spectral Angle Mapper	60
4.4.2	Continuum Removal	62
4.4.3	Spectral Mixture Analysis	62
4.5	Spectroscopic models	63
4.5.1	Spectral mixing model	63
4.5.2	Spatial scaling	64
5	DISCUSSION	66
5.1	Data preprocessing and quality assessment	66
5.2	Basic image evaluation	66
5.3	Discrimination approaches	67
5.3.1	Clustering	67
5.3.2	Band ratioing and indexing	68
5.3.3	Supervised Classification	69
5.4	Plastic identification	70
5.4.1	Spectral Angle Mapper	70
5.4.2	Continuum Removal	73
5.4.3	Spectral Mixture Analysis	75
5.5	Spectroscopic models	76
5.5.1	Spectral mixing model	76
5.5.2	Spatial scaling	76
5.6	Plastic target characteristics at sea	77
6	CONCLUSIONS	79
6.1	Summary of research work results	79
6.2	Answers to the research questions asked	80
6.3	Outlook on further research steps	81
	APPENDIX A: SCIENTIFIC LITERATURE	83
	APPENDIX B: DERIVATIVE SPECTROSCOPY	85
	ACKNOWLEDGMENTS	89
	DANKSAGUNG	90
	REFERENCES	91
	PERSONAL DECLARATION	97

LIST OF FIGURES

Figure 1-1: Distribution of floating plastics in counts and weight for different size classes	14
Figure 1-2: Impressions of ocean plastic debris	15
Figure 1-3: Solar radiation, atmospheric absorption bands (yellow) and known plastic absorption features.	18
Figure 2-1: Impressions from experimental setups and locations	22
Figure 3-1: Methods overview	28
Figure 3-2: RGB visualisations of the image subsets over Irchel Pond	32
Figure 3-3: RGB visualisations of the Greifensee location.	35
Figure 3-4: Index calculation theory.	38
Figure 3-5: RGB visualisations of the Hallwilersee location	43
Figure 4-1: Binary water masks for the Irchel location with superimposed position vectors of the test fields....	49
Figure 4-2: MNF bands of the masked APEX radiance subset	51
Figure 4-3: Reflectance signals of the APEX, AVIRIS-NG, and Sentinel-2 sensor	52
Figure 4-4: Spectral profiles of water and PET test area reflectances as well as radiances.....	52
Figure 4-5: Spatial profile of the APEX reflectance RGB bands.	53
Figure 4-6: Enhancement methods: Histogram stretching	54
Figure 4-7: K-means results of the APEX radiance subset data	56
Figure 4-8: Index results for APEX radiance data	57
Figure 4-9: Index results for AVIRIS-NG radiance data.	58
Figure 4-10: Results of supervised classification using only 2 reference classes.....	59
Figure 4-11: Results of supervised classification using 4 reference classes	60
Figure 4-12: SAM results for all locations and both AVIRIS-NG and APEX data.....	61
Figure 4-13: Continuum Removal results.....	62
Figure 4-14: Matched Filtering results (APEX, Greifensee).....	63
Figure 4-15: Spectral mixing model with APEX water (Greifensee) and ASD-PET spectra	63
Figure 4-16: Approximation of PET abundancies in the 3 test fields based on mixture analysis	64
Figure 4-17: K-means results of spatially upscaled APEX data.....	65
Figure 5-1: K-means results using the whole spatial subset area for evaluation	68
Figure 5-2: Threshold considerations for the SAM results (AVIRIS-NG, Hallwilersee).	71
Figure 5-3: Spatial subset extent considerations for the SAM results (APEX, Greifensee).	71
Figure 5-4: Spectral subset considerations for the SAM results (APEX, Greifensee).	72
Figure 5-5: Spectral curves at absorption feature positions.....	74
Figure 5-6: Pixel Purity Index for the APEX image at Greifensee location.....	75
Figure B-1: First impressions of the spectral characteristics	86
Figure B-2: First order to fifth order derivatives calculated for the mean PET reflectance spectrum.....	87
Figure B-3: Coloured spectral ranges where certain conditions for absorption features are met.	88

LIST OF TABLES

Table 1-1: Most common plastic types by composition.	13
Table 2-1: Remotely sensed data sets acquired over the PET test installations.....	27
Table 3-1: Selected bands for index calculations, including the ENVI Band Math formulas.	39
Table 3-2: Defined index value ranges for selected density slice ranges of the APEX result images	39
Table 3-3: Spectral subset definitions and ENVI Band Math formulas for CR calculations.	45
Table 3-4: Defined CR value ranges for selected density slice ranges of the APEX result images.....	46
Table 4-1: Image spectroscopy data product image band assessment.....	50
Table 5-1: PET abundancies in the experimental test fields.	76
Table 6-1: Scored summary of the applied methods and results.	79
Table A-1: Scientific papers addressing marine pollution detection and identification	83

LIST OF ABBREVIATIONS

ANG	Short form for AVIRIS-NG, used especially in datafile naming by NASA
APEX	Airborne Prism Experiment (airborne imaging spectroscopy sensor)
AUC	Area Under Curve
AVIRIS-NG	NASA's Next Generation Airborne Visible Infrared Imaging Spectrometer
BRDF	Bidirectional Reflectance Distribution Function
CR	Continuum Removal
ENVI	ENVI is an extensive software application used in GIS and remote sensing data analysis
ERDAS	Earth Resource Development Assessment System (software application for GIS and remote sensing data analysis)
ESA	European Space Agency
FOV	Field Of View
GIVOF	Ground Instantaneous Field of View
GPGP	Great Pacific Garbage Patch (a large convergence zone of ocean surface currents)
GRFS	Short form used for the Greifensee location
HAWS	Short form used for the Hallwilersee location
HI	Hydrocarbon Index
MATLAB	MATrix LABoratory (high-level language and interactive environment for numerical computation, visualization, and programming)
MF	Matched Filtering (partial unmixing approach)
MNF	Minimal Noise Fraction (data transformation approach)
MTMF	Mixture Tuned Matched Filtering (a partial unmixing approach using MNF bands)
NASA	National Aeronautics and Space Administration (United States)
NIR	Near infrared (wavelength range of the electromagnetic spectrum: 700 – 1000 nm)
NOAA	National Oceanic and Atmospheric Administration (United States)
PET	Polyethylene terephthalate (common plastic type, used for beverage bottles)
PPI	Pixel Purity Index
RGB	Red, green, and blue spectral bands of the visible light
ROI	Region of interest (pixel selection in a raster image)
RSL	Remote Sensing Laboratories, University of Zürich
S2	Sentinel-2 (ESA's multispectral satellite)
SAM	Spectral Angle Mapper (supervised classification algorithm)
SMA	Spectral Mixture Analysis
SNAP	SeNtinel's Application Platform (open source platform providing ESA toolboxes for the exploitation of ESA's sentinel satellite data)
SPECCHIO	Spectral database and information system
SVM	Support Vector Machine (classification method)

SWIR	Short wave infrared (middle infrared region, wavelength range of the electromagnetic spectrum: 1000 – 2500 nm)
TOA	Top Of Atmosphere
UAV	Unmanned Aerial Vehicle (often referred to a drone)
VIS	Visible light (wavelength range of the electromagnetic spectrum: 400 – 700 nm)
VNIR	VIS and NIR spectral ranges (400 – 1000 nm)

1 INTRODUCTION

It was during a coffee break with scientists of the RSL team when I asked my question for the first time. This was back in September 2016 and I had just started my master's studies in Remote Sensing, wondering what chances and challenges this chosen field would yield for the semesters to come. On the eve I had read, quite by chance, a momentous article in the latest print issue of a scientific journal about the alarming plastic pollution in the world's oceans (Cressey, 2016). Therefore, my concerned question was: "Is it actually possible to detect all that floating plastic in the oceans with remote sensing technology?" – "Not that I knew of, but that's a good one – just keep that question in mind", Andy replied.

And so I did. The thematic focus of this master's thesis research project lies on the aggravating environmental pollution problem of marine plastic debris. To date, it is known that the amount of plastic debris in the world's oceans is already enormous and exponentially increasing (Eriksen et al., 2014). Oceanographic models of current patterns and accumulation areas allow predictions of debris occurrence and density. But reliable measurements of true location and quantity are sparse, considering the sheer vastness of the oceans total surface area. It is believed that remote sensing is the only technology capable of providing observation coverage of such vast areas within a practicable period of time (Maximenko et al., 2016; Hafeez et al., 2019). However, research on this topic is still in its infancy (Goddijn-Murphy et al., 2018).

1.1 Scientific background

In the next subsections, this introductory part provides an overview of the framework topics related to the localisation problem of floating plastic debris. This includes a short overview on the dimensions, effects and environmental consequences of the pollution problem and on debris distribution processes in the oceans as well as on material composition and categories. Most importantly, the scientific framework that forms the background to the work at hand is presented: Which approaches and methods, which research projects and findings have been achieved to date in the field of remote sensing technologies for the optical detection of floating macro plastics?

1.1.1 Ocean plastic pollution

The uncontrolled release of plastic waste ending up in the oceans has become a global ecological problem of gigantic proportions in the recent decades. Plastic products offer short-term benefits, but their long-term impacts – due to ubiquitous distribution, inadequate waste disposal and extremely slow degradation rates – have largely been neglected for decades. Recently, this environmental issue attracts considerable media and public attention. While the emerging ocean plastic pollution problem has been known in scientific circles for half a century already (Andrady, 2011; Thompson et al., 2009a), its real dimensions and harmful environmental effects are still not fully understood (Jambeck et al., 2015; Teuten et al., 2009).

What actually makes this plastic waste such a big problem - perhaps apart from visual impairments and negative economic impacts on tourism destinations? I explored this question as a preparatory thematic basis for this thesis, and out of personal interest and concern. The summarized findings went into a literature-based semester study in the field of ecotoxicology, in the context of my minor subject and supervised by Prof. Dr. Karl Fent (Bertschi, 2018). Harmful impacts on the oceanic environment are caused by plastic waste as long as it floats in the water column – and on our coastal living environment when debris is washed up in large quantities..

Generally, plastic waste directly affects marine wildlife via two means: entanglement and ingestion. A recent study documented over 600 marine species affected by plastic waste in the oceans (Wilcox et al., 2015). In addition to these primarily physical effects, adverse long-term effects result from additives and toxic pollutants adsorbed to fragmented and degraded plastic debris and ingested by organisms of all trophic levels (Gregory, 2009). Since toxicity always depends on the concentration of a contaminant, the processes of biomagnification and trophic transfer from the smallest benthic organisms to fish and eventually to the human diet raise increasing concern (Worm et al., 2017). For the present work, however, these ecological facts are not further elaborated, as the focus lies on the poorly known distribution parameters of macro plastics in the oceans.

The amount of plastic waste that globally enters the sea each year is estimated to be approximately 10 million tonnes (Jambeck et al., 2015). A simple calculation allows a more concrete and better imaginable order of magnitude of this quantity: This represents a full truck load of plastic waste that enters our oceans – every single minute. And it is anticipated that this amount will increase exponentially in the future: “Reports have it that by the year 2050, there will be more microplastics in our oceans than fish” (Auta et al., 2017). But huge differences between estimates of plastic waste mass entering the oceans annually and of floating plastics are being reported – while the real quantity of plastic waste in the oceans is unknown (Jambeck et al., 2015).

What is the fate of plastic debris once thrown or washed into the sea? At first, there are physical processes involved in fragmentation and transportation of the waste items. It is believed that vertical transport processes in the ocean eventually lead to the sedimentation of the fragmented plastic waste when its specific weight is altered by biofouling (Auta et al., 2017; Koelmans et al., 2017; Maes et al., 2018). Furthermore, huge quantities of plastic waste with a lower specific weight are washed up on beaches all over the world (Lavers et al., 2016).

Plastics are a subgroup of the material class of polymers which are composed of large molecules consisting of organic compounds: hydrocarbons. Polymers are ubiquitous and can be of natural or synthetic origin (other subgroups are elastomers (rubbers), fibres and films). They are produced synthetically by polymerization of low-weight monomers which are organic materials generally derived from petroleum. They come in thousands of polymer combinations and with various chemical additives (Worm et al., 2017; Thompson et al., 2009b). Plastics are considered the most widely used polymers (Emadian et al., 2017) and even the most widely used man-made substances (Worm et al., 2017) because of their usefulness. They are incredibly versatile materials - cheap, lightweight, strong, and corrosion-resistant, with high thermal and electrical insulation and plasticity properties (Thompson et al., 2009b). Another advantage – its durability – however poses enormous environmental concerns, since the material accumulates and persists in the environment for centuries, even for up to thousands of years, as some estimates predict (Barnes et al., 2009; Li et al., 2016).

Which are the categories of marine plastic waste? Plastic debris can be classified by size category, type, composition, and with regard to their optical properties additionally by degradation and fragmentation state. **Size** category definitions are various and inconsistent, even for the most common distinction between microplastic and macroplastic. While common classifications often differ between macroplastics (> 2 cm), mesoplastics (5 mm – 2 cm), microplastics (1 µm – 5 mm), and nanoplastics (< 1 µm) (Eriksen et al., 2014; Worm et al., 2017), detection using optical sensors is only considered possible for macroplastics. Plastic **types** include – besides whole items such as drinking bottles – sheet fragments, pellets, cosmetic beads, fibres, lines, and foams. Regarding classes by **composition**, close to 5000 different types of plastic are known today. But only a few account for approximately 90 % of the total global production and are most abundantly used and thus found in ocean plastic waste (Li et al., 2016). These are listed in the table below.

Table 1-1: Most common plastic types by composition.

Plastic material type			Products and typical origin
Class		Specific gravity	Substantiation
PA	Polyamids (Nylons)	1.13 - 1.35	Fibers, nets, toothbrush bristles, fishing line
PC	Polycarbonate	1.20 - 1.22	Compact discs, security windows, lenses, construction materials
PE (HDPE)	Polyethylene, high-density	0.94	Juice jugs
PE (LDPE)	Polyethylene, low-density	0.91 - 0.93	Plastic bags, six-pack rings, bottles, netting, drinking straws
PES	Polyester	1.4	Fibers, textiles
PET	Polyethylene terephthalate	1.30 - 1.37	Plastic beverage bottles
PP	Polypropylene	0.85 - 0.83	Rope, bottle caps, netting
PS	Polystyrene	1.05	Plastic utensils, food containers (foam cups)
PU	Polyurethane	1.12 - 1.15	Plastic film, bottles, cups
PVC	Polyvinyl chloride	1.38	tarpaulings, shower curtains, sheets

1.1.2 Quantification and localisation of floating plastic waste

The **total amount** of plastic floating in the oceans today can only be estimated on the basis of projections. These are based on countless tow net samples collected over the years (Cozar et al., 2014; van Sebille et al., 2015), but only a very marginal proportion of the immense global water surface area¹ of 361'000'000 km² (Leser, 2001) has been systematically sampled to date. Such projections are the result of complex oceanographic surface current models (Potemra, 2012; Lebreton et al., 2012; van Sebille et al., 2015; Eriksen et al., 2014). Despite the large spatial uncertainties contained in such data, the magnitudes of the numbers are alarming. Eriksen et al. (2014) published one of the most comprehensive and often cited studies estimating the global amount of floating plastic debris at sea. Using an oceanographic model of floating debris dispersal, a large volume of data that had been collected from ships during 24 expeditions (2007 – 2013) was used to calibrate this model. Calculations estimated “a minimum of 5.25 trillion particles weighing 268'940 tons” floating in the world's oceans (Eriksen et al., 2014). And recent research has come to the conclusion that previous figures systematically underestimate the real quantity of ocean plastic (Koelmans et al., 2017). If one wants to get an idea of how much plastic waste per unit area is floating on the sea surface on the basis of such numbers, then the figures vary greatly. For example, mass concentrations of 0.01 – 100 kg/km² within the Great Pacific Garbage Patch (Lebreton et al., 2018) and an average of 0.579 kg/km² in the Mediterranean (Ruiz-Orejón et al., 2016) have recently been reported. Another study has reported comparable average quantities of 70 g/km² (Eriksen et al., 2013) for the accumulation zones in the South Pacific. With regard to the data evaluated for this thesis, a huge discrepancy must be noted: While the latest example data correspond to 0.00007 g/m², the evaluated reference areas contain 1 - 2 PET bottles/m². As for the number of debris items, an average particle concentration range of 100 – 1'000'000 items/km² and a maximum concentration of over a million items / km² were reported by these example research projects. This order of magnitude, on the other hand, corresponds exactly to the evaluated data.

The **spatial distribution** of plastic debris in the oceans is even more difficult to estimate than its total quantity. Ocean distribution models are subject to considerable variance “due to high uncertainty in underlying data and assumptions” (Liubartseva et al., 2018). Moreover, distribution pattern is subject to constant change. Large-scale oceanographic circulations greatly influence debris distribution and determine accumulation of floating marine debris in the convergence zones at subtropical altitudes of all major oceans (Brach et al., 2018).

¹ This area accounts for approximately 71 % of the Earth's surface.

In these anticyclonic eddies, debris material is collected due to Ekman transport processes, resulting in the often mentioned "garbage patches" of great expanse such as the GPGP. In overall terms, complex large-scale and meso-scale surface currents as well as climate oscillations (e.g., El Niño/La Niña) cause regional and temporal variability in debris concentrations, further accentuated by seasonal climate patterns with altering prevailing winds (e.g., monsoon cycles) and tides. With all this variability on multiple temporal and spatial scales, current and detailed distribution data are largely unknown.

What is undoubtedly known, however, is the fact that today plastic waste is found everywhere in the oceans, on the surface and throughout the water column down to benthic sediments (Law et al., 2014), washed ashore on beaches and even near polar regions (van Sebille et al., 2015). Still, at a global scale, distribution maps of ocean plastic waste are mainly based on oceanographic modelling, as is illustrated in the exemplary *Figure 1-1* below.

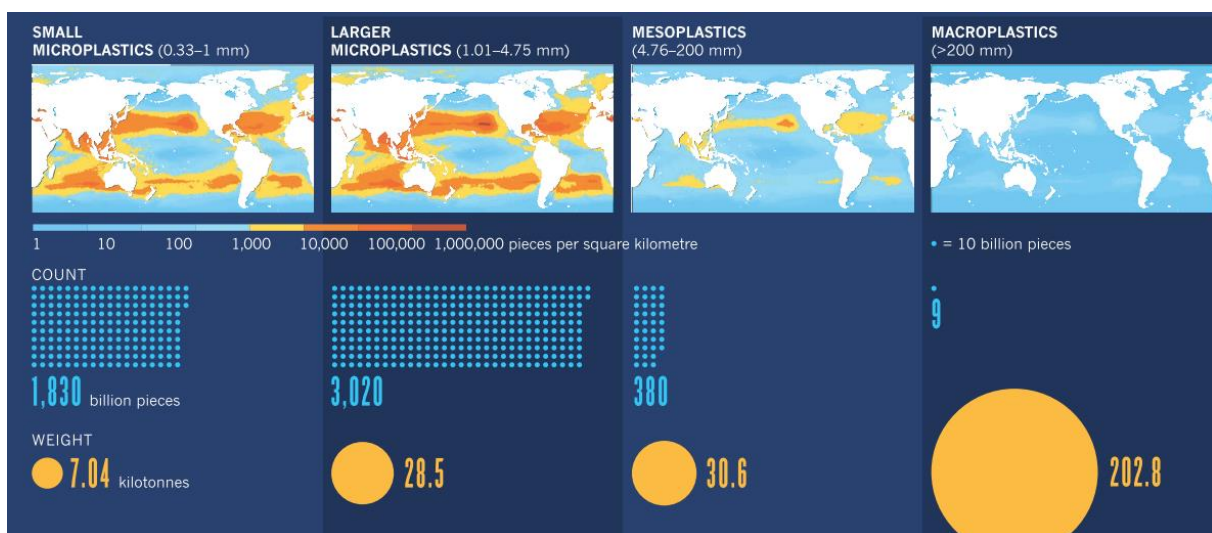


Figure 1-1: Distribution of floating plastics in counts and weight for different size classes (Cressey, 2016).

Simulations as in the above example are inadequate particularly for macroplastics distribution. But why would it be useful to know where all the plastic in the oceans is? While globally monitoring and knowing about the concentration and distribution of the debris is not a goal in itself, it is however a most relevant means to show and quantify the scale of the problem, to provide useful information to debris removal operations – and hopefully to increase the pressure on decision-makers in politics and economics. A global map showing litter concentrations that is based on actual measurements would also provide important insights to scientists regarding quantification and distribution patterns. Moreover, it would hold greater power in communicating the problem for the public as well as for policymakers (ESA, 2018).

In order to have an illustrative presentation of the topic, examples of ocean plastic debris as well as the tow net sampling method are compiled on the following page. The selection of examples was deliberately made in order to contrast those images of "garbage carpets" distorted by the media with the appearance of more realistic debris densities.



Figure 1-2: Impressions of ocean plastic debris. While (a) corresponds to a common conception of so-called "garbage carpets", this picture represents an extreme case of garbage washed in by a river after a tropical storm. (b) represents heavily polluted coastal waters, (d) shows derelict fishing gear, and (g) depicts barnacles on floating bottles. However, typical sights of floating plastics in the Aegean Sea and washed ashore are illustrated in (c, e, f, h, i). The common sampling method using neuston tow nets for floating microplastic particles is shown in (k).

1.1.3 Remote sensing approaches

Remote sensing is seen as the only technology that has the potential to solve the problem of the location of drifting plastic waste on the world's oceans through monitoring and spatial quantification. With regard to an automated localization of plastics on the oceans, only satellites could cover the enormous spatial dimensions within reasonable time intervals. In fact, the European Space Agency has recently started a program to investigate satellite detection requirements for marine plastic litter observation (ESA, 2018), and international scientific conferences² have been launched worldwide. However, research in the field of remote sensing is still in its infancy and only a handful of research projects have been published to date. No remotely sensed image analysis of small abundancies of floating plastic on natural waters seems to exist. In this sense, the present work constitutes a novelty.

What has been achieved in remote sensing of ocean plastic debris to date? A compilation of the research papers in this field is presented in a complete list in *Appendix A*. These, however, are mainly theoretical concepts regarding radiative transfer models, are based on laboratory measurements and modelling, or focus on very large (> 1m) floating items and beached waste. Garaba et al. (2018) presented the only research paper so far where spectral feature comparison for large floating debris was applied on remotely sensed imagery of ocean debris. This research comes closest to the present study in terms of its objective and methods of investigation. Approaches have also been made with satellite data (Acuña-Ruz et al., 2018; Aoyama, 2016; Biermann, 2019), although it is still not possible to identify ocean plastic with existing satellites. Thus the relevant statement in Wikipedia still applies³.

What remote sensing technologies, what sensors and sensing distances might represent a conceivable solution? In a ground-breaking international workshop in 2016 on remote sensing approaches for marine debris sensing, the general possibilities offered by the various remote sensing platforms were summarized as follows: "Traditional optical imagery can be used for the largest debris in selected cloud-free areas; synthetic aperture radar imagery and interferometry is suited for all-weather detections and drift measurements; imaging spectroscopy can detect low concentrations of subpixel-size plastic particles; and Raman spectroscopy, which penetrates below the surface, is useful for measuring debris sunk in shallow seas or suspended in the upper ocean" (Maximenko et al., 2016). Based on this summary it becomes obvious that, for the fundamental question of this work, imaging spectroscopy (also known as hyperspectral remote sensing) is considered the remote sensing technology of choice.

The underlying physics of image spectroscopy: The foundation of optical physics dates back to the 17th century and the pioneering work by Isaac Newton, but only in the 20th century, spectroscopic instruments were developed and in the 1950s and 1960s, the first remotely sensed spectral data were recorded (Mac Arthur and Robinson, 2015). The fundamental principles of optical physics form the physical basis of spectroscopy, stating that photon energy level and flux density change occurs when light interacts with a surface material and that, consequently, spectral measurements contain information on the light source (e.g., solar radiation intensity), the atmosphere (e.g., gas content resulting in light scattering and/or absorption), and the surface with which the light has interacted. In spectroscopy, the energy level is indicated by wavelength, and flux density is measured as radiant flux (Mac Arthur and Robinson, 2015).

² Under the lead of the National Oceanic and Atmospheric Administration (NOAA) and the UN Environment organization, the probably most comprehensive International Marine Debris Conference is held regularly: <http://internationalmarinedebrisconference.org/> (last accessed August 28, 2019)

³ https://en.wikipedia.org/wiki/Great_Pacific_garbage_patch (last accessed August 29, 2019)

Why is remote sensing regarded as the only technology with potential in ocean plastic detection? Basically, the key point lies in the immense surface of the oceans: Optical satellite monitoring is the only way to capture this surface in real time. An entire field of research, called “ocean remote sensing” already focuses on large-scale detection and monitoring of physical and biogeochemical oceanic factors such as water temperature and salinity, wind force and wave height, ice cover extent and drifting icebergs, and suspended organic matter concentration such as algae blooms (Martin, 2014; Frouin et al., 2016; Venkatesan et al., 2017). However, it is not (yet) about waste monitoring - this would be an obvious next scope of application.

The detection of plastic debris by highly specialized spectral sensors is considered due to the specific spectral properties of plastic materials. Material identification and automated sorting of plastic types based on spectroscopic technique is well established and successfully applied in waste separation plants (Vázquez-Guardado et al., 2015). The classification accuracy for these applications is remarkably close to 100% (Moroni et al., 2015). In this context, normalized reflectance spectra can be fully characterized and identified when considering the spectral NIR and MIR spectral ranges (0.3 – 12 μm).

In contrast to this spectral data acquisition under laboratory conditions, the spectral range of data acquired by remote sensing sensors is not sufficient for the detection of all commonly used plastics (Vázquez-Guardado et al., 2015). The reason for this lies in the light transmittance of the Earth's atmosphere. Some spectral regions cannot be used in remote sensing because atmospheric gases absorb essentially all the emitted solar radiation. A few gases among the approximately 30 atmospheric gases absorb solar radiation at specific wavelengths over the spectral range relevant in remote sensing (between 400 – 2500 nm). In particular, the molecules of water vapor (H_2O), carbon dioxide (CO_2), ozone (O_3), oxygen (O_2), carbon monoxide (CO), methane (CH_4), nitrous oxide (N_2O), and nitrogen dioxide (NO_2) absorb solar radiation, resulting in effective loss of energy to the atmosphere (Gao et al., 2009). The wavelength ranges in which the atmosphere is transparent for solar radiation – and thus usable for remote sensing – are mostly in the VIS and NIR regions of the electromagnetic spectrum. They are called atmospheric windows (Lillesand et al., 2008).

However, a trade-off is unavoidable: While plastic materials can be unambiguously and automatically identified using spectroscopy, this approach is impaired in the natural environment due to atmospheric properties and, as far as to our knowledge, has not yet been applied successfully under typical oceanic conditions. Only remote sensing technologies, on the other hand, allow global coverage of ocean surface within a useful time frame. This is exactly where this study comes in.

Behind the spectral signatures of the chemistry of hydrocarbons: The wavelength position of spectral features such as absorption peaks are strictly related to the chemical structure of the material and to the underlying quantum mechanical mechanisms of electronic and vibrational states (Manolakis et al., 2016). Thus, spectral absorption features are characteristic for certain materials. Absorption peak positions of plastics are strictly related to the chemical structure of polymers, as the spectral organic features common in polymers absorb light in the NIR region via the first overtones of the normal vibrational modes that involve stretching of the C-H and O-H bonds (Cloutis, 1989; Moroni et al., 2015). Thus, their spectra show a distinctive depression at these wavelength positions. For PET material samples, well noticeable absorption peaks were identified at 1130 nm, 1170 nm, 1420 nm, and 1660 nm (Moroni et al., 2015).

An overview on both the most important atmospheric windows (and accordingly the water vapor absorption regions) and the known plastic absorption feature wavelengths, *Figure 1-3* provides an overview which is based on (Gao et al., 2009; Jensen, 2016; Richter and Schläpfer, 2016; Vázquez-Guardado et al., 2015). Highlighted in blue are those known plastic absorption features that coincide with important atmospheric water vapor

absorption bands. And highlighted in green are those spectral regions of known absorption by plastic materials which will be systematically considered in the following analyses.

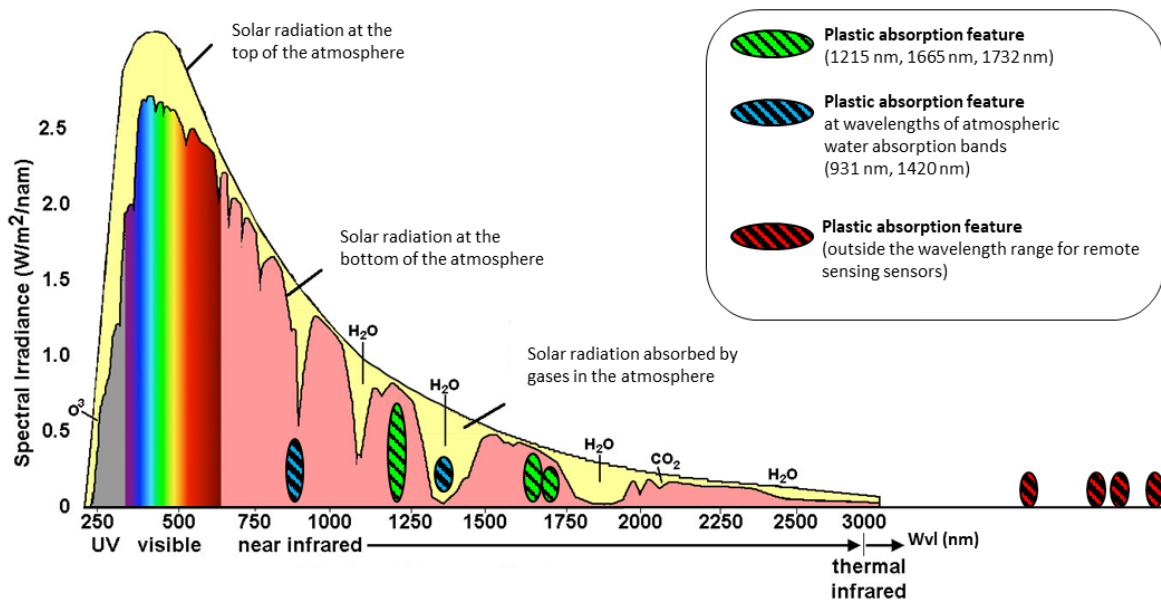


Figure 1-3: Solar radiation, atmospheric absorption bands (yellow) and known plastic absorption features.

Besides the detailed knowledge of material inherent properties, further optical properties such as size, presence and concentration of encrusting organisms (as shown in Figure 1-2 (g)), and factors like surface degradation and roughness are determinant for the spectral signal (McElwee et al., 2012). Furthermore, sea state and atmospheric conditions affect the optical signal. Here it becomes obvious how many factors are involved in the task at hand. In the discussion chapter (Section 5.6) those factors which directly influence debris detection using imaging spectroscopy are taken up again.

1.2 Research questions and working hypothesis

The main **research focus** is on the investigation of optical detection possibilities for floating plastic debris at the water's surface. Thus, the research questions are addressed in the form of a feasibility study, exploiting remotely sensed imagery of experimental installations of floating PET bottles.

Thus, the **main research questions** are:

- (1) What plastic surface densities on water bodies can be identified from spectral data?
- (2) What spatial resolution is needed for detection?
- (3) What spectral information (spectral range and resolution) is relevant to distinguish between water and plastic surfaces?
- (4) Which factors influence the detectability?

Based on preliminary literature research, these questions are addressed with the passive remote sensing technology of imaging spectroscopy. And consequently, the working hypothesis is:

"Image spectroscopy can be used to k f g p v k h { . " s w c p v k h { " c p f " o c r " h n q c v k p i "

2 DATA

This chapter contains a compilation and characterisation of the datasets used for the analysis in this study. The following subsections first provide an insight into the considerations, preparations, and practical implementation of the experimental setting for the purpose of controlled test data acquisition. Then, data acquisition parameters are described as well as the preprocessing steps, both radiometric and geometric, which are normally carried out by the data providers.

The most relevant datasets for this thesis consist of aerial image spectroscopy data, acquired with the AVIRIS-NG and APEX sensors during the RSL summer flight campaigns 2018 over temporary installations of floating plastics with varying predefined surface abundances. Spaceborne data were acquired twice by the Sentinel-2 multispectral ESA satellites when orbiting over the experimental setup locations. Additional field data were purposively acquired in order to obtain further typical plastic and water spectra as reference values. Together with other auxiliary data, the data pool used for this study comprises a solid diversity with varying spatial and spectral resolution. *Table 2-1* at the end of this chapter gives an overview of the remotely sensed imagery.

2.1 Experimental design and setup

At the onset of the work no data set was available and therefore an experimental design to acquire data was required. How could the questions about technical feasibility of plastic detection on water surfaces be tackled? What remotely sensed data would be helpful? What kind of experimental setups would be necessary?

Since no remotely sensed imaging spectroscopy data of ground-referenced floating plastic items was neither known nor available, the main research questions of this thesis required quite some creative ideas and considerable efforts in order to acquire a meaningful data pool. Remotely sensed imagery of such "plastic targets" with precisely documented local position and surface density would represent the indispensable database for explorative analyses.

It was, however, a unique opportunity that emerged at the beginning of summer 2018. In the context of the annual research flight operations with the European Airborne Prism Experiment (APEX), organized by the RSL department at UZH, some of the flight strips for data acquisition were planned across nearby Swiss lakes. Furthermore, there was the prospect that NASA's Next Generation Airborne Visible Infrared Imaging Spectrometer (AVIRIS-NG) would be operated in selected research areas over Switzerland (and other European countries) as part of an international research collaboration⁴. These flights were also coordinated at RSL, which is why both the planning data of these flights were known and the collected data would be available for research. The fact that this NASA sensor, considered to be the most outstanding of its kind and unprecedented in radiometric accuracy and spectral uniformity, would be flown over Switzerland for the first time since 1991 (AVIRIS-classic) was an extremely promising prospect!

Together with the fact that I am a passionate sea kayaker owning a great little folding kayak⁵, these flight operation plans were the starting point for the idea of an experimental setup of plastics prior to these data acquisitions. But the framework conditions were a challenge, and the success of this idea was very uncertain.

⁴ Information by Andy Hueni who is responsible at RSL for research flight planning

⁵ A seaworthy and agile "K-light" model, built in Vancouver, Canada, 20 years ago by Feathercraft

2.1.1 Experimental design and preparations

Nevertheless, as soon as the possibility of targeted data collection on water surfaces became concrete, the conceptual and practical preparations for the field experiments began. Generally, for optical detection of ocean plastic waste, the relevant factors are object size, material composition, surface consistency, and its spatial distribution both horizontally and vertically.

A fundamental question was: how large should a meaningful test area be at least? Its **surface area** should allow unambiguous identification of plastic containing pixels in the resulting image, considering pixel size and expected geometric accuracy of the imagery. The planned flight levels would result in data with a spatial resolution of 6.3 cm (HyperSpec) and between 2.5 – 4.1 m for the APEX and AVIRIS-NG airborne sensors.

The detection limit for **plastic abundance** on the water surface is expected to be below 5% surface abundance (Bochow, 2013; Maximenko et al., 2016). These expectations represent the only relevant clue in the scientific literature. However, they are based on laboratory measurements. Whether this estimation also applies under realistic conditions was unknown at the time the experiments were planned and carried out. The latest research project on this topic was published only afterwards and makes the assumption that a 5% plastic abundance "might not be appropriate for detecting ocean plastics" (Garaba and Dierssen, 2018)

The aim was to prepare a test field above this limit and (at least) one test field below this limit in order to approximate the actual detection limit based on this gradation. However, this plastic abundance could only be roughly estimated during preparation. For this purpose, the outlines from 5 of each of the selected PET bottles of both sizes (irregularly flattened) were drawn on 5mm paper. Based on their averaged outline, an area of 130 cm² was estimated for the smaller bottles and 300 cm² for the larger ones. Supplementary observations of the buoyancy behaviour of the bottles on the water revealed that an estimated 20 - 33% of their surface remains submerged. Accordingly, estimations of resulting plastic areas at the water surface per PET bottle were reduced to roughly 100 cm² and 250 cm², respectively. Therefore 1 - 2 bottles per m² test area would be required.

High-resolution RGB drone data and in particular the high-resolution HyperSpec data were intended for the subsequent exact determination of the abundance, ideally supplemented by mixture model analysis. It must be emphasised that the planned abundance of the test areas is targeted at the expected technical possibilities. Realistic abundance in ocean gyres, on the other hand, is reported to be more than 1 piece per m² – with an average size of plastic debris objects which make up only an extremely tiny fraction of a PET bottle. Newest results of average plastic mass concentrations estimate 1 g per m² (!) in the GPGP (Lebreton et al., 2018). Against this background, it is therefore of great importance to interpret the following methodical data evaluations and results with regard to technical feasibility.

The **practical framework conditions** were:

- ◁ Due to weather conditions, the day of the flights are known only at very short notice and installation of the test areas must be set up and removed on the same day.
- ◁ The lakeshore near the intended test positions must be accessible for material transport, and all necessary permits must be obtained in time.
- ◁ All material must be manageable by one person alone and from a kayak, i.e. transport from the lakeshore to the selected position on the lake, deployment, and temporary anchoring.
- ◁ Since the exact overflight time depends on actual air traffic and Skyguide's permission, the material should be installed as early as 10 o'clock in the morning.

In spite of concerns about practical feasibility – especially due to time limitations during the very days of the research flights – surface net constructions with PET bottles were prepared. The aim was to have different controlled abundances of plastic for spatially defined test areas on a natural body of water for data acquisition in a realistic setting. These plastic net constructions however had to be within the scope of my possibilities, lightweight and controllable for one person alone, since the plan was to deploy and anchor them only with the aid of my great little folding kayak.

Plastic test area construction: How do you create a total of 300 m² of plastic pollution on a lake, which afterwards has to be completely removed? Since PET bottles were readily available and also represent one of the most common types of marine plastic waste, this material was chosen. No special attention was paid to the colours of the selected bottles, since colour does not show significant influence in the spectral signal (Vázquez-Guardado et al., 2015). They correspond largely to the average mixing ratio of recycled PET in central Switzerland where at least 50% is transparent, about 20% is green, about 10% each are brown and yellow, and only a few are light blue or completely dark. These empty bottles were flattened to some extent, closed, and attached to their bottle necks with parcel cords. First attempts with a painstakingly measured and prepared cord net of regularly interwoven small PET bottles on the lakeshore resulted in an inextricable, frustrating, wet disaster once in the water. It turned out that the chosen parcel cords - when wet - got entangled incredibly quickly. It became obvious that the plastic fields could only be tied together on the water.

The solution found was to knot 20 - 30 PET bottles at regular intervals into individual, 10 m long cords and then hang them separately into a previously anchored "frame" using small material carabiners. This frame also consisted of parcel cords, with prepared loops at regular intervals also for marking. The individual test areas contain 240 * 1.5 l bottles (8 lines of 30 bottles each), 120 * 1.5 l bottles (6 lines of 20 bottles each), and 120 * 0.5 l bottles (6 lines of 20 bottles each), all temporarily anchored to the bottom of the lake and with **resulting plastic surface abundances of approximately 5%, 2.5%, and 1%**. Additional bottles were used in all test area corners for anchor positions and were partly submerged because of the tension on the anchoring cords. In total, the test installation consisted of 492 PET bottles. Comparable test data never seem to have been generated in a natural body of water. Few research projects in our field have mapped artificial floating plastic surfaces near the beach (Topouzelis et al., 2019) or acquired their reflectance spectra with a field spectrometer (Goddijn-Murphy and Dufaur, 2018).

Another challenge was the selection of **suitable locations**, for which the lakeshore areas were explored and identified on preceding kayak excursions. Particular attention was paid to the vegetation and topography at the lake shore for considerations of light incidence and shadow effects, whereas the accessibility and depth of the water played a more practical role. In addition, there was the consideration of the shipping routes, nature conservation zones, and popular bathing areas, which had to be avoided wherever possible. Once the most suitable locations had been determined, all the authorities involved had to be informed and the necessary permits obtained.

2.1.2 Deployment of floating plastic reference fields

The chosen experimental setup solution finally covered three plastic test fields of 10m x 10m each with a distance of 20 m in between, resulting in a total test area of 700 m². The distance between these test surfaces should ensure that no different surface abundance occurs in the same pixel, with respect to satellite data resolution.

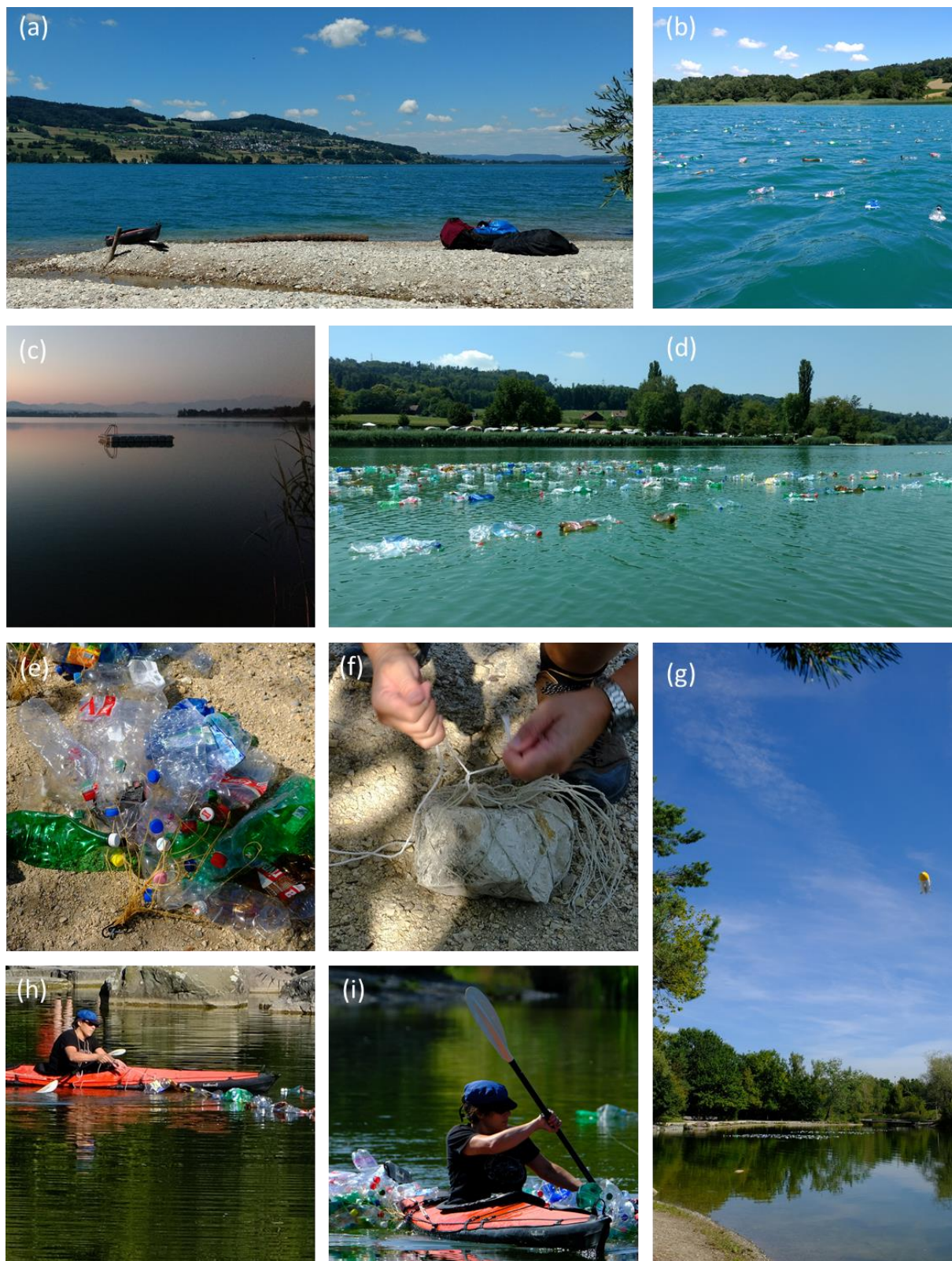


Figure 2-1: Impressions from experimental setups and locations. (a) and (b) show the Hallwilersee location after data acquisition when the wind had nearly calmed down, with (b) giving an impression of the 1% PET test field. The Greifensee location is shown in (c) at the moment when setup started at 5.20 am before sunrise and in (d) with the 5% PET abundance (foreground) and 2.5% (barely visible) test fields. Irchel location: (e) one of the carefully coiled bottle lines; (f) illustrates one of the 14 handmade, cheap and reusable anchor nets temporarily filled with local stone. Refined deployment (h) and deinstallation (i) technique with gained practice and (g) unique occasion of a zeppelin overflying the Irchel Pond – and the deployed test areas - at an altitude of only 150 m AGL. ((a) – (h) courtesy Daniel Furrer).

2.1.3 Locations

The closer spatial environment of these three test locations can be characterized as follows:

The **Irchel Pond** is located in the middle of the park of the same name, which is directly adjacent to the university campus Irchel 3 km north of Zürich's city centre on the western slope of the Zürichberg hill⁶. It is an artificially created pond with only a negligible inflow, a shallow maximum water depth of only about 6 m with a total water area of only 6'800 m². Of course, the environmental factors of the park are far from comparable to an open ocean setting. The main reasons for conducting the experiment at this location however were for practicability and flight plan restrictions. However, the unique chance to acquire – in a very first attempt – spectral data of specifically designed and controlled floating plastic targets topped the disadvantage of the small water body and resulting adjacency effects. The pond is surrounded by playgrounds and some higher trees, which nevertheless do not directly obstruct the direct solar radiation in the area of the test areas. However, adjacency effects of these trees on the measured data cannot be ruled out. While interfering adjacency effects both from land and atmosphere generally increase towards the shore, they “remain significant to as far as 20 km off shore” (Odermatt, 2011). Therefore, adjacency effects can generally not be ruled out. At this location, a small adjustment had to be made to the deployment design: because of the small water area, the distance between the individual test areas had to be shortened from 20 m to 10 m.

The plastic test areas on Lake **Greifensee**, 10 km east of Zürich, are located in the western part of the lake, in a distance of 97 – 120 m from the slightly sloping reed-covered lake shore, at a water depth of about 20 m. This lake is comparatively high in nutrients.

For the choice of the test area on Lake **Hallwilersee** a compromise had to be chosen between the position of the flight strips, course ship lanes, closed protection zones, and shadows cast by tall shore vegetation. The chosen location is near a gravel delta (the gravels served as a makeshift anchor weight), in a distance of 30 - 50 m to the close-by nature reservation zone and 70 – 90 m to the eastern lake shore, at a water depth of 14 – 16 m.

2.2 Data acquisition and baseline processing

The airborne data acquisition took place within the scope of the annual flight missions at RSL, whereby the spectral data of the relevant test areas were made available in the desired product levels. ESA's satellite data are available online via the precisely researched product specifications, spatial parameters, and acquisition dates. ASD field data, GPS location coordinates, and image acquisition with drones were collected especially for this research project in 2018.

2.2.1 APEX airborne data

APEX, the Airborne Prism Experiment, is a dispersive pushbroom imaging spectrometer based on prisms, covering the spectral range between 372 and 2540 nm with a spectral sampling interval of 0.45–7.5 nm in the VNIR (400 – 1050 nm) and 5 – 10 nm in the SWIR (1050 – 2500 nm), respectively. It is a Swiss-Belgian development on behalf of ESA and has been introduced in 2009. It is operated by VITO and the RSL at the University of Zurich (Schaeppman et al., 2015).

⁶ Distance information on this page is based on the swisstopo online map (map.geo.admin.ch) or derived from the imaging spectroscopy data directly (pixel count based calculation of the Irchel pond surface area using the defined binary mask) .

The APEX imaging spectrometer was flown with a Cessna at an altitude of 6.5 km with heading 062° for the first flight strip and providing data with 2.6 m across-track GIFOV for the Irchel location. Over the Greifensee location, the flight level was at 5 km with heading 324°, resulting in the highest spatial resolution with 2.1 m GIFOV that could be acquired of the plastic test areas. Since pixel sizes in across-track direction are given by the above-ground altitude and in along-track direction by the flight speed over ground (and sensor technology), the resulting pixels are rarely square (Hueni et al., 2017). They were georectified and spatially resampled, resulting in pixel sizes for both locations of 2.0 m with an assumed geolocation accuracy of +/- 1 pixel. Radiometric calibration of the raw data to radiances generated level-1 data, which were exclusively geocoded on request. The reason for this was its intended use because atmospheric correction models often employ a "dark pixel approach" for water surfaces which might eliminate meaningful spectral details (Goddijn-Murphy et al., 2018; Emberton et al., 2016). The underlying assumption of this **black pixel approach**, initially made for clear ocean waters and ocean colour satellite applications, is that the ocean is optically black in the NIR where values of water leaving radiance only contain atmospheric aerosol and ocean surface effects (Emberton et al., 2016; Siegel et al., 2000). While this approach, "thought to be accurate to within ~5%" (Siegel et al., 2000) may be valid for certain applications, it is "rarely valid for waters with significant particulate" (Bailey et al., 2010) and would very likely hide the signal from floating plastic. Therefore, atmospherically uncorrected data would be needed (Goddijn-Murphy et al., 2018).

By default, the radiance data were converted to bottom-of-atmosphere reflectance level-2 data (more precisely: to HCRF) using the ATCOR4 atmospheric correction software (Hueni et al., 2017). This algorithm applies interpolations to bands of the atmospheric water vapor absorption regions around 940, 1130, 1400 and 1900 nm and generally to bands with low signals (Richter and Schlöpfer, 2016). For both the georectification and atmospheric correction steps, the digital elevation model "swissALTI3D" with a 2 m grid cell size was used (Hueni et al., 2017).

2.2.2 AVIRIS-NG airborne data

NASA's Next Generation Airborne Visible Infrared Imaging Spectrometer (AVIRIS-NG) was developed by JPL at the California Institute of Technology as a successor of the AVIRIS spectrometer. Weighing 465kg⁷, this pushbroom mapping instrument is based on an Offner spectrometer design and measures reflected light in the spectral range from 380 - 2510 nm with 480 continuous bands at a spectral resolution of 5 nm ± 0.5 nm (Thompson et al., 2018a).

The AVIRIS-NG sensor was flown on the Beech B200C Super King Air aircraft at a speed of 315 km/h over the Irchel location the same day and also during the same midday hours as APEX, but at a lower flight level. This sensor also acquired the data over the Hallwilersee location on a windy day when occasional clouds blocked the view down to the targeted surface area. One advantage of this carefully selected location was that it was to be captured by two overlapping flight strips. And because of such clouds, the planned flight strips had to be covered twice, which finally resulted in a total of 4 images of the target location. Due to the sensor's different IFOV (compared to APEX), the GIFOV and thus the spatial resolution resulted in a image pixel size of 4.1 m for the Irchel location and slightly higher with 4.0 m for the Hallwilersee location. All these flights were made in an east-west direction.

⁷ <https://avirisng.jpl.nasa.gov/specifications.html>

An alternative to conventional atmospheric correction is applied for the AVIRIS reflectance data product. The method is based on the ATmospheric REMoval (ATREM) algorithm (Thompson et al., 2015), a combined model of atmospheric scattering, absorption, and surface reflectance based on probabilistic model inversion theory. It achieves overall reflectance errors of 1.0% (Thompson et al., 2018b).

2.2.3 Sentinel-2 satellite data

ESA's Sentinel-2 is a wide-swath, high-resolution, multi-spectral satellite mission which involves a constellation of two polar orbiting satellites (Sentinel-2A and Sentinel-2B) in the same sun-synchronous orbit, offset by 180°. With a wide swath width of 290 km, this constellation results in revisit times of 2 – 3 days at mid-latitudes. Its optical instruments sample in 13 spectral bands with spatial resolutions of 10 m, 20 m, and 60 m for selected bands⁸.

While the spectral band configuration is designed for land applications, its overall spectral and spatial resolution characteristics make it one of the most promising – however not ideal – operational satellite for the detection of floating plastics. Data acquisition over the oceans, however, is only provided for coastal waters, enclosed seas (such as the Mediterranean) and other specified regions (European Space Agency, 2015). Despite the fact that there is little prospect of a successful plastic detection due to the spatial and especially the spectral resolution of these satellite data, Sentinel-2 data is considered here as well. This is due particularly to the lucky fact that on two of the experimental days, these satellites flew over Switzerland in their orbit at noon.

Level-1C imagery was downloaded for analysis from the ESA's Copernicus open access hub (scihub.copernicus.eu). This data contains top-of-atmosphere (TOA) reflectances in cartographic geometry and is provided in tiles of 100 km *100 km spatial extent. For the area of central Switzerland, covering the deployed plastic test areas at the Irchel and Greifensee locations, the relevant tiles are 32TMT. Standardized radiometric and geometric preprocessing steps are applied on Level-1C products. Radiometric processing includes radiometric correction and a dark signal correction. Geometric processing includes ortho-rectification based on a digital elevation model, and spatial registration on a global reference system (in UTM/WGS-84 projection) with sub-pixel accuracy (European Space Agency, 2015).

2.2.4 Auxiliary data

Furthermore, on all experiment days in the Irchel park, **RGB pictures were taken with drones** from low altitude (approx. 100 m). These images of the setting, taken from a bird's eye view in high spatial resolution, were mainly used to ascertain the exact geolocations of the test field corner points (*Section 3.1.1*) and to determine PET area fractions of the test areas on the water (*Section 3.5.1*).

For the test area corner positions on the lakes, **GPS data** were acquired directly in the field using a handheld GPS (Trimble GeoXT on Hallwilersee and Garmin Oregon 600t on Greifensee) from the kayak. These positions, acquired in the standard map projection WGS-84, were later converted to a vector file and used as geometric overlay information in various methods applications. The vector file was generated using the Point Collection tool and importing point data from the GPS' ASCII-file in ENVI.

Standardized **field reference measurements** with the ASD-3 fieldspectrometer were routinely carried out on selected surface types during the overflights for cross validation. In addition, field measurements were acquired

⁸ ESA's Sentinel mission online portal: <https://sentinel.esa.int/web/sentinel/missions/sentinel-2> (last accessed 25.08.2019)

in the Irchel park in order to obtain some reference spectra which could be useful in the context of the present work.

The targets selected were a minimally reflective black plane, 90 of the PET bottles used during the experimental setups, and the water body of the Irchel pond. All bottles were arranged to create 100% surface coverage. The black plane was used as a base to prevent reflective fractions of the lawn. Reflectance of this plastic target was then measured both on land and floating with both dry and wet surfaces on the water. The surface roughness of the water was also of interest. The smooth surface of the water was measured as well as small waves caused by water treading, which led to changes in the surface geometry.

Since field spectroscopy is based on relative measurements of target and reference panel radiance, a tripod with bubble level was used to horizontally adjust the white Spectralon reference panel, and reference measurements were taken systematically before and after target measurements, ensuring that the reflectance panel completely fills the FOV of the spectrometer (Milton et al., 2009; Milton, 1987). For each target, a series of 30 measurements in vertical direction were taken applying the sweep sampling scheme while keeping a distance of 1 m between sensor and target. Ideally, the operator should wear cotton clothing, take a position perpendicular to the solar principle plane and keep at least one arm's length away from the target object (Hueni et al., 2017). For the measurements on land these specifications could be easily met, but for the measurements of dry and wet floating PET bottles as well as the smooth and agitated water surface, these specifications - standing in cold water on uneven ground and loaded with the ASD spectrometer - were only partially feasible.

The ASD binary files were then imported into the SPECCHIO⁹ spectral database at RSL and automatically calibrated from DN to radiance (Hueni et al., 2009). Relevant metadata such as location and target descriptions, sensor and sun geometries, and atmospheric conditions were added. Interchannel radiometric steps between the ASD spectroradiometer's spectral detectors due to temperature result in radiometric miscalibration (Hueni and Bialek, 2017). To compensate for these radiometric steps in the wavelength regions of 1000 and 1800 nm, a correction model was developed and provided as a MATLAB tool by Hueni and Bialek (2017). This function is also integrated in SPECCHIO's reflectance calculation tool and was applied prior to reflectance calculation.

In the context of the LSMD Demo Day 2018, data acquisition over the test setting at the Irchel location was planned as "Ocean Plastic Experiment". Using the **Zeppelin NT** as research platform, the plastic targets were imaged by a NanoHyperspec camera from two flight levels at 150 m and 300 m AGL, resulting in pixel sizes of 6.3 and 12.6 cm, respectively. This hyperspectral camera was mounted on a gimbal system which was installed on the outside of the passenger cabin before the flight.

2.3 Resulting data pool

The most relevant datasets for this thesis consist of aerial imaging spectroscopy data (AVIRIS-NG and APEX), acquired during the RSL summer flight campaigns 2018 over temporary installations of floating plastics with varying predefined surface densities. In addition, spaceborne data were acquired from the Sentinel-2 multispectral ESA satellites when orbiting at the same date over the experimental test areas.

Data products that were used for data analysis in this work comprise both Level-2 reflectance and Level-1 radiance images from both image spectroscopy sensors, and Top-of-Atmosphere reflectance (Level-1C) products of the Sentinel-2 satellites. Spectral reference measurements from the laboratory and the field were added supplementing.

⁹ SPECCHIO Spectral Information System: www.specchio.ch (last accessed 20.09.2019)

Unfortunately, it was only at a late stage when our suspicion was confirmed that the high-resolution data collected during the unique experimental zeppelin flight were faulty due to a malfunction of the gimbal system. This mechanical system should have continuously orientated the attached NanoHyperspec sensor precisely downwards during the irregular three-dimensional airborne platform motions (rolling, pitching and yawing) in order to ensure constant acquisition geometry during the flight. Therefore, the promising hyperspectral dataset with extremely high spatial resolution was of no practical use for evaluation.

Together with the collected field data both during the flight missions and separately – to obtain further typical plastic and water spectra as reference values – the data pool used for this study comprises a solid diversity with different spatial and spectral resolution. The table below gives an overview of all remotely sensed data of the PET test installations. Those entries which are highlighted in bold have been used for the following analysis.

Table 2-1: Remotely sensed data sets acquired over the PET test installations. Flight and sensor parameters were taken from the corresponding data header files, from in house mission documents, or were computed¹⁰.

Acquisition date			Illumination		Flight parameters				Sensor characteristics		
date	time (local)	location	solar zenith [°]	solar azimuth [°]	platform	speed [km/h]	altitude AGL	pixel size [m]	sensor	spectral range	spectral bands
11.06.2018	11:00	Irchel	52	117	UAV	~ 30	~ 100 m	(cm)	RGB camera	380 - 2510 nm	RGB
27.06.2018	12:07	Hallwilersee	61	139	airplane	315	4.5 km	4	AVIRIS-NG	380 - 2510 nm	425
	12:16		62	142							
	12:55		65	161							
	13:04		65	166							
01.07.2018	12:10	Irchel	61	140	airplane	260	6.5 km	2	APEX	372 - 2540 nm	334
01.07.2018	12:50	Irchel	64	158	airplane	315	4.5 km	4.1	AVIRIS-NG	380 - 2510 nm	425
01.07.2018	12:20	Irchel	62	144	satellite	27'000	786 km	10 - 60	Sentinel-2A	VIS - SWIR	13
01.07.2018	11:45	Irchel	58	130	UAV	~ 30	~ 100 m	(cm)	RGB camera	VIS	RGB
24.07.2018	12:35	Greifensee	60	152	satellite	27'000	786 km	10 - 60	Sentinel-2B	VIS - SWIR	13
24.07.2018	14:05	Greifensee	62	196	airplane	260	5 km	2	APEX	372 - 2540 nm	334
11.09.2018	11:20 - 11:50	Irchel	41	142	zeppelin	18	150 m 300 m	6.3 cm 12.29 cm	Nano-Hyperspec	400 - 1000 nm	270
11.09.2018	11:15	Irchel	39	137	UAV	~ 30	~ 100 m	(cm)	RGB camera	VIS	RGB

¹⁰ Illumination parameters were calculated using the online tool by NOAA and compared with the image product metadata where provided. (<https://www.esrl.noaa.gov/gmd/grad/solcalc/azel.html>). The satellite speed was calculated with the orbit time of 100 minutes, then rounded for easy comparison. .

3 METHODS

According to the explorative character of this study, this methods chapter contains successive analytical parts, starting with basic data analysis steps and progressively aiming at more specialized information extraction methods designed for imaging spectrometer data analysis. In the last subsection, differences between the evaluated test settings compared to the optical conditions, which are to be expected in more realistic situations at sea, will also be addressed.

During this explorative process, some of the most often used analytical methods in remote sensing are discussed and applied on varying imagery, while the focus always remains on the previously stated research questions. The chosen methods essentially cover three selected elements of data comparison: spectral similarity, material-specific absorption features, and subpixel fraction evaluation based on spectral mixture analysis. However - and this design might differ slightly from comparable reports - an additional objective of this thesis is to provide an insight into the nature of remotely sensed imagery to the reader with little previous expertise in the field. This is in particular the reason for the true colour visualisations of the data subsets in this chapter.

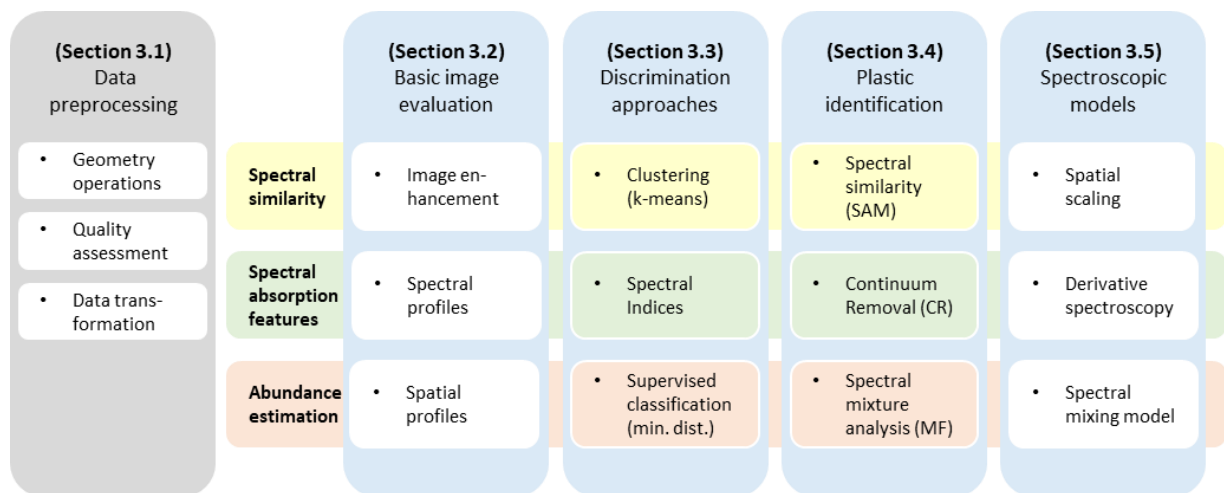


Figure 3-1: Methods overview: The three selected elements of data comparison are emphasized in yellow, green, and orange, while the chapters structure follows the working process with increasing specialization in the applied methods.

3.1 Data preprocessing and quality assessment

Prior to image evaluation, some basic preprocessing steps were applied. These include in particular the definition of spatial subsets for the test areas contained in the high volume imagery. Subsequently a basic image quality assessment was performed on all image subsets, mainly to ensure that the data would not contain any technical issues. Furthermore, another preparatory step included MNF data transformation, since some algorithm use noise-reduced MNF data as input.

3.1.1 Data preprocessing

First, image geometry operations were applied to the selected data products. For the **Irchel location**, spatial subsets, containing all available spectral bands, were defined with equal side lengths of 200 m (205 m for the

AVIRIS-NG data) for each of the provided imagery. Due to different pixel sizes, the resulting subsets contain 400 pixels (S2, 10 m pixel size), 2'500 pixels (AVIRIS-NG, 4.1 m pixel size), and 10'000 pixels (APEX, 2 m pixel size), respectively. During baseline preprocessing, AVIRIS-NG products remain orientated in their flight line direction. Thus, they generally are not north-oriented but come with a defined rotation angle. **Image rotation** (70.0 ° clockwise, according to the rotation angle of -70.0 °) was applied to this data in order to have all images (and pixels) in the same orientation for easier comparison.

For the **satellite data**, a resampling to 10 m spatial resolution was necessary for all bands except for bands 2, 3, 4, and 8 of the downloaded data tiles prior to layer-stacking and spatial subsetting. The bicubic upsampling method was chosen, and these steps were all performed using ESA's SNAP software tools.

Masking: The focus in data processing here is on the water surfaces. In order to exclude all land areas from further analysis, binary water masks were created for each of the image subsets, using the ENVI Build Mask tool (*Figure 4-1*). These masks were defined based on the pixel values from one single image band. For the APEX reflectance data, band 71 (with 744 nm central wavelength in the NIR range) was chosen to separate land from water pixels. The data value range for water pixels was defined from 0 to 1000 after investigation of the pixel values on the edges of the water body. This threshold implies that water reflects only up to 10% of the irradiance at this wavelength (percentage values result from rescaling the reflectance values with the scale factor inherent in the data product). For the AVIRIS-NG data, band 75 (747 nm) was chosen to define reflectance values from 0 to 0.085 as water pixels. For the Sentinel-2 satellite image, only four of the 13 bands have an original pixel size of 10 m, with band 8 being the suitable band in the NIR, allowing for easy separation of land and water surface pixels. The reflectance value range from 0 to 1100 was defined as water pixels.

Irchel test field corner position determination was done based on a drone image (*Figure 3-2 (a)*) through application of an image geocoding approach using a geometric (polynomial) approximation model¹¹. Ten control points were defined at well identifiable positions (e.g., crossroads, bridge centre point) in the image, and reference point coordinates were determined manually on the basis of the detailed Swiss Map (map.geo.admin.ch). The geometric model was then solved with the defined control points using the nearest-neighbour resampling method. Based on the resulting geocoded image, the test field corner positions were then determined and stored as vector point data. All these steps were applied using the ERDAS Imagine 2014 software.

The available imagery from the **Greifensee test site** was preprocessed accordingly. From the APEX radiance data, two square subsets were defined with side lengths of 100 m (50 pixels) and 800 m (400 pixels), respectively. The smaller subset covers only water surface containing the three PET test areas. The larger subset also covers the lake shore and nearby land areas. A binary water mask was created for the latter one, based on band 100 (983 nm) where values < 10 were used to select the water area. In this case, the shore zone was also masked, and smoothing was necessary, using convolution (median filter with a 5x5 window size) and morphology filtering (dilate option) as additional steps. Here, the satellite reflectance data were subset to the same areal extents as the APEX data, resulting in images of 10x10 and 80x80 pixels, respectively. For mask definition, values < 1000 from the satellite's band 8 were selected. Accuracy for both masks was verified using ENVI's Window Overlay function with 50% transparency. GPS positions of the test area corners were measured and converted into a vector layer, as described in Section 2.2.4.

¹¹ This approach is based on exercise 6 within the framework of the lecture «Geo233 - Übungen zu Grundlagen Fernerkundung» at RSL / UZH, 2014.

The available imagery from the **Hallwilersee test site** was preprocessed similarly. A larger square spatial subset with 100 pixels on each axis was considered ideal, resulting in 10'000 pixels. This subset covers an area of 400 m x 400 m due to a slightly lower flight level (compared to the Irchel location) and resulting AVIRIS-NG pixel size of 4.0 m. Image rotation was applied again, but the vegetated shore zone was not masked, as all intended algorithms are expected to deal with such land areas as well. Again, the acquired GPS positions of the test area corners were converted into a vector layer.

3.1.2 Initial image quality assessment

A basic image quality assessment was performed on all image subsets. Visual comparison of these PET test area positions with the derived corner positions of each test field was done for all georeferenced images (the AVIRIS-NG radiance image of the Irchel location is the only one not georeferenced). **Geometry accuracy** is regarded an issue only for the satellite data, since the brighter patches of the PET test areas were identifiable in the high resolution data visualizations.

Regarding **radiometric accuracy**, qualitative band examination was done, using the animation function provided in ENVI for the imaging spectroscopy data. The focus here was to find whether serious artefacts or faulty spectral bands are present in the data. In addition, visual examination of the water areas, using colour composite image subsets, was done to verify that no cloud or sun glint artefact is obstructing the locations of interest. While geometric and radiometric quality can be easily estimated from in the high resolution images, quality assessment for the satellite data was rather limited to statistical band information. At this point, no further statistical band examination was done, since the main focus of this qualitative assessment was in obtaining a first general usability estimate of the imagery at hand.

As it turned out, the APEX reflectance data of the Greifensee location contains further artefacts along image lines within the subsets. For this added reason, the APEX radiance data were used for subsequent analysis steps only. A radiometric comparison of the image values with field measurements would have been a further, sensible step to evaluating the image quality. Unfortunately, no field reference values of the water surface were acquired accordingly, which would have allowed the most relevant comparison for the data subset of the test areas.

For the Hallwilersee location, 4 datasets were acquired in total. Thus, a first quality assessment step consisted of selecting the most suitable image for the subsequent evaluations. While two of the pictures were affected by clouds and shadows, the other two seemed suitable without unwanted artefacts in the area of interest. Finally, the dataset was selected where the pixels of the test areas were slightly better identifiable using histogram stretching as shown in *Figure 3-5 (b)*. Thus, the geometry accuracy of the GPS points could be checked visually for this location as well.

3.1.3 Data transformation

Data transformations aim at reducing redundancy in multispectral image data by compressing the information content into fewer bands (Lillesand et al., 2008). In addition to reducing computational effort, the main advantage lies in the noise suppression which is achieved by decorrelating noise and image content and omitting resulting noise bands in subsequent analyses (Kneubühler et al., 2007). Principal Component Analysis (PCA) is one of the most widely applied statistical methods for dimensionality reduction. While there exist various versions of this powerful statistical tool, the standard PCA is a non-spatial approach that is applied to raster data and on the attribute space only (Demšar et al., 2013). The resulting **Minimal Noise Fraction (MNF)** bands

contain decreasing variance, hence the highest image variance is contained in the first bands. Therefore, only those MNF bands containing image information can be used with increased computational efficiency in subsequent analysis.

Although this technique primarily distinguishes the most basic image categories and therefore does not seem to be suitable for the detection of small amounts of plastic components in mixed pixels, in the framework of the chosen explorative approach, the method was applied anyway. The reason is that possible findings could be useful with regard to very large scale data products where efficient analytical methods are crucial. MNF forward transformation was applied on the masked APEX radiance subset image, using the corresponding ENVI software function. The smaller subset could not be used as its number of pixels is too small for statistical calculations.

3.2 Basic image evaluation

The main goal of this subsection is to assess whether the acquired data products can be expected to form a useful quality data basis for this research. The focus of this subsection lies on the following points:

- ◁ **Location:** Data from the Irchel location are used for basic visualisation and comparison, since this is the only location where data of the same floating plastic installation could be obtained by all three sensor types (satellite and airborne) at the same day during midday.
- ◁ **Sensors and data products:** Reflectance products are in focus here, since they represent the common data product type used for spectral image analysis. They are available for all three sensors in differing spectral and spatial resolution. In addition, imaging spectroscopy radiance data is consulted for basic product level comparison.
- ◁ **Methods:** The applied methods include visualisation and visual enhancement approaches.

Common basic image analysis methods can be grouped based on the dimensionality of the spectral data involved: An image dataset can basically be analysed (i) using only one spectral band (e.g., binary mask definition, density slicing), (ii) using two or three spectral bands (e.g., indexing, colour visualisation), (iii) using all available spectral bands, (iv) or by taking the spectral curve characteristics into account. In this first methods subsection, (i) is applied for binary mask definition of the water surface area within the spatial data subset images, (ii) is applied for true colour and false colour image representations, and all spectral bands (iii) are relevant for spectral profile visualisations. (iv) is addressed by more specialized methods and will be considered in later sections.

Figure 3-2 below contains RGB representations of the drone photo, the satellite image, and both airborne images of the APEX and the AVIRIS-NG sensors. While the drone image does not cover the full spatial extent of the subset images, its very high spatial resolution gives an impression both of the floating PET nets - which are of primary interest here - and of the greenish water colour as it appeared to the human eye on that hot summer day of data acquisition. The unequal spatial resolution of the images make the most obvious difference. Different brightness levels, on the other hand, are merely a display effect, resulting from the average brightness values of the original large datasets.

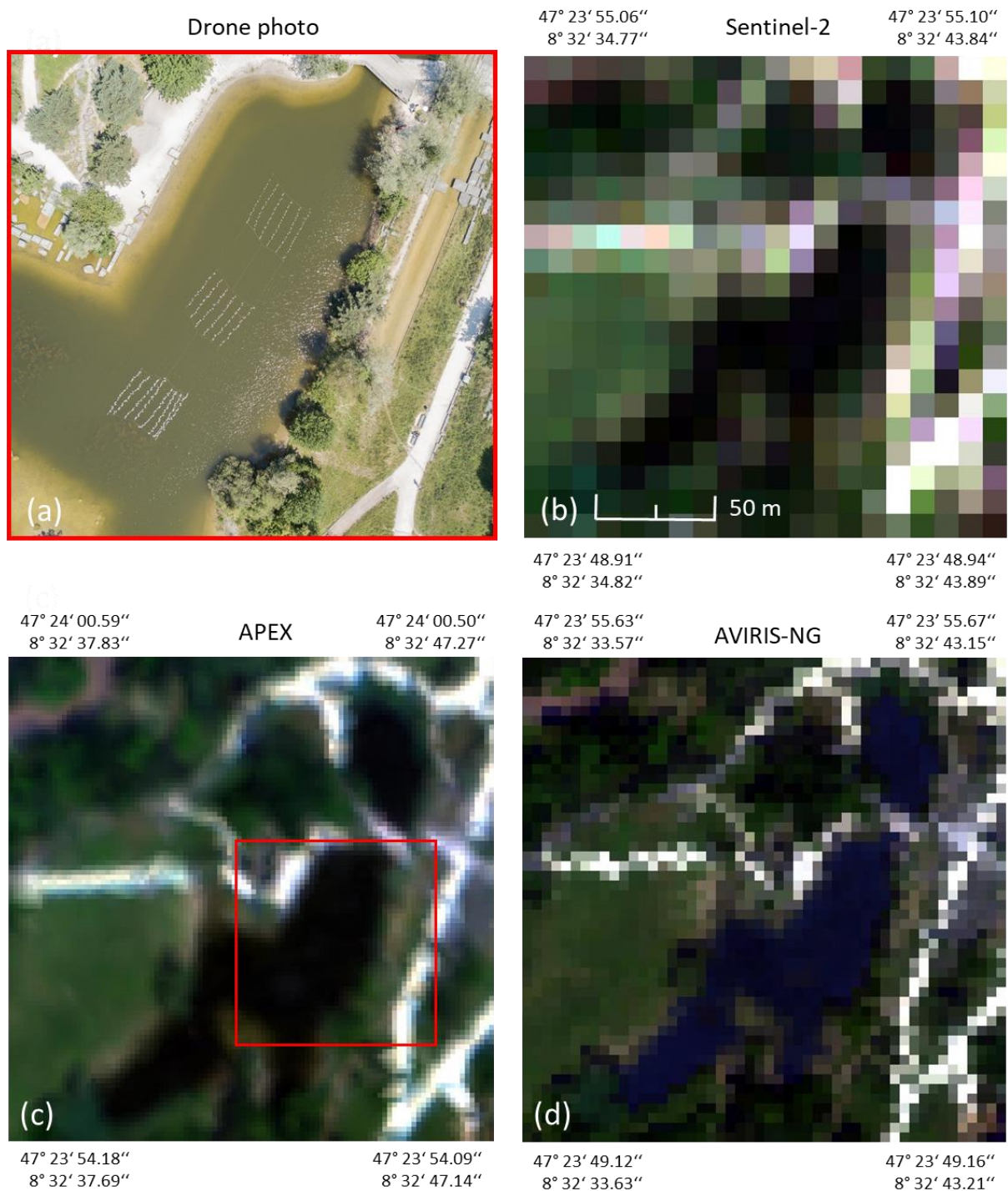


Figure 3-2: RGB visualisations of the image subsets over Irchel Pond. (a) shows the drone image taken over the relevant part of the pond shortly before airborne image acquisition (courtesy Dr Hans-Christian Koch). (b) contains Sentinel-2 data (R: band 4, G: band 3, B: band 2), (c) the APEX reflectance data (R: band 40, G: band 17, B: band 6) and (d) the AVIRIS-NG reflectance data (R: band 54, G: band 36, B: band 18). Map coordinates (WGS-84) are indicated for all subset corner positions, based on the relevant image header information.

3.2.1 Spectral and spatial profiles

Spectral profiles contain the image values of all spectral bands for one single pixel. In order to provide an overview on the available data, reflectance and radiance spectra from all image subsets were collected in groups (according to the manually defined regions of interest (ROI's) in ENVI) and exported from the imagery as ASCII files for further evaluation in MATLAB. Spectra were selected from the three PET test areas as well as from the surrounding pond water surface while avoiding the very shallow shore zones.

Regarding the satellite data, unfortunately it was not possible to specifically select the single image pixels covering one of the test fields each, as the pixel boundaries meet in the middle of the PET test fields with the result that many of the water pixels contain a fraction of the plastic signals. Still, with a simple approach in an attempt to find those pixel values that are most likely covering floating plastic areas, the satellite image subset was rescaled to a pixel size of 5m. Thus, 3 - 5 small pixels could be selected per test field, from which the mean vector was calculated. For the APEX data, over 20 pixels were selected per field, while there were only 4 – 6 pixels per field for the AVIRIS-NG data, due to different pixel sizes. Selection in all cases was based on the central location within the pond as well as on the brightness differences visible in the imaging spectroscopy image displays, rather than on the vector corner point coordinates.

Therefore, in order to focus on the "typical" spectra, only the calculated mean values per group are displayed in the spectral profile visualizations (*Figure 4-3 and Figure 4-4*). Reflectance values were all rescaled to the range of 0 – 100%. For reasons of completeness, radiance spectra were also considered.

Spatial profiles can be defined along a user-specified line in a single-band or 3-band composite image in order to extract brightness values of the pixels along this line (Jensen, 2016). This was done for the APEX reflectance image because of its smallest pixel size where the defined line across all three PET test areas touches the largest number of pixels. This was done using ENVI's Arbitrary Profiles Tool (*Figure 4-5*). The most important purpose of this visualization is to make a gradient (better) visible across the different PET abundances, while the consideration of accurate distance calculation is less important in this case. A distance calculation based on pixel counts would be distorted due to the stepped nature of the defined transect with an inclined angle to the image geometry.

3.2.2 Image enhancement approaches

Many methods exist to visualize pixel information contained in a multilevel image dataset. During a first investigative data assessment, many of them (histogram stretching and density slicing; grey colour, true colour and false colour displays) were applied. In *Figure 4-6* a selection of these visualisations is presented to illustrate a few commonly used methods and to highlight some obvious image features. For most of these steps, the masked subsets were evaluated. The APEX band for the grey colour display was not chosen randomly but calculated using ENVI's Spectral Math Tool: Two image pixels were selected, representing (brownish-green) water and the mixed signal of the PET test field with the highest plastic abundance. The calculated difference of these two spectra was then analysed to find the wavelength position where the two spectra show the largest difference over the whole spectrum. The spectral band representing this wavelength position was then histogram stretched to enhance its variability for the water surface.

3.2.3 Outline

This first part is not aimed at answering any of the research questions yet. But it provided some first image characteristics that are promising for further analysis steps of the APEX and AVIRIS-NG imagery. These include the visible brightness differences and even some scaling effect in the RGB visualisations where the PET bottles are afloat.

However, the limitations of a multispectral satellite band configuration for our target of interest is obvious. This is a first indication towards answering research question (3) about spectral sensor resolution requirements. Also, unwanted effects (missing band information or band interpolation in atmospheric absorption regions as well as water leaving radiance approximations) due to atmospheric correction algorithms might advocate the analysis of radiance images rather than the usual reflectance images. This evaluation corresponds to the latest research literature on this question (Garaba and Dierssen, 2018; Goddijn-Murphy et al., 2018). The small pond area is also seen as no ideal location due to adjacency effects and very shallow depth, resulting in most inhomogeneous water pixels in all images.

3.3 Discrimination approaches

The reasons for this subsection – prior to the imaging spectroscopy data analysis approaches in focus – are twofold: First, in the framework of this explorative study, it was considered important to evaluate the level of detail inherent in the acquired data, as well as finding what clusters are most obvious from a mathematical/statistical point of view. This seemed all the more appropriate in view of the fact that the evaluation of water surfaces and at the same time of small hyperspectral signal differences is a type of data investigation in which no previous practical experience had been gained. And second, only for imagery (sensor, processing level) where these methods reveal significant differences in the relevant water pixels, further analysis steps will be advisable.

Thus, the guiding question in this method subsection is about finding differences in airborne (or even satellite) imagery between water areas with small abundancies of floating plastic and surrounding water surfaces. In this methodical subsection, the focus lies on the following points:

- ◁ **Location:** Data from the Greifensee location are of priority in this subsection, because the two available datasets acquired over the floating plastic installation here contain highest variability in both spectral and spatial resolution parameters. In addition, good visibility and very little wind at time of data acquisition were the favourable environmental parameters for a best possible starting position.
- ◁ **Sensors and data products:** The APEX radiance data, geocoded and resampled to a 2 m pixel size, is analysed and compared to the multispectral Sentinel-2 satellite Level-1C reflectance product with a resampled pixel size of 10 m for all bands.
- ◁ **Methods:** Common image analysis and classification techniques are applied here, subsequent to the basic visual methods. These techniques are for automated information extraction from remote sensing data and were designed originally for multispectral imagery, thus they are not particularly designed to extract subtle features in continuous spectral signatures. These methods primarily aim at finding statistical differences and clusters in the data, and for unsupervised algorithms, the expected results generally cannot yield information on specific (plastic) surface materials. For supervised approaches, ground reference information about the precise location of the PET test areas is used for reference pixel

specification. In addition, theoretical findings from scientific literature are included. This applies in particular to specific absorption features in the spectrum of plastic materials, which form the basis for the **Hydrocarbon Indices**.

- ◀ **Research focus:** Discrimination analysis can only be an intermediate step towards more specific answers about the detectability and identification of floating plastics. It is likely, however, that this step already means end of the line with regard to satellite data, which is why initial results about spectral as well as spatial sensor resolution requirements can be expected here. In addition, the application of the Hydrocarbon Indices will show whether this approach can be applied at all to very small signal fractions, since no such information was found in the literature.

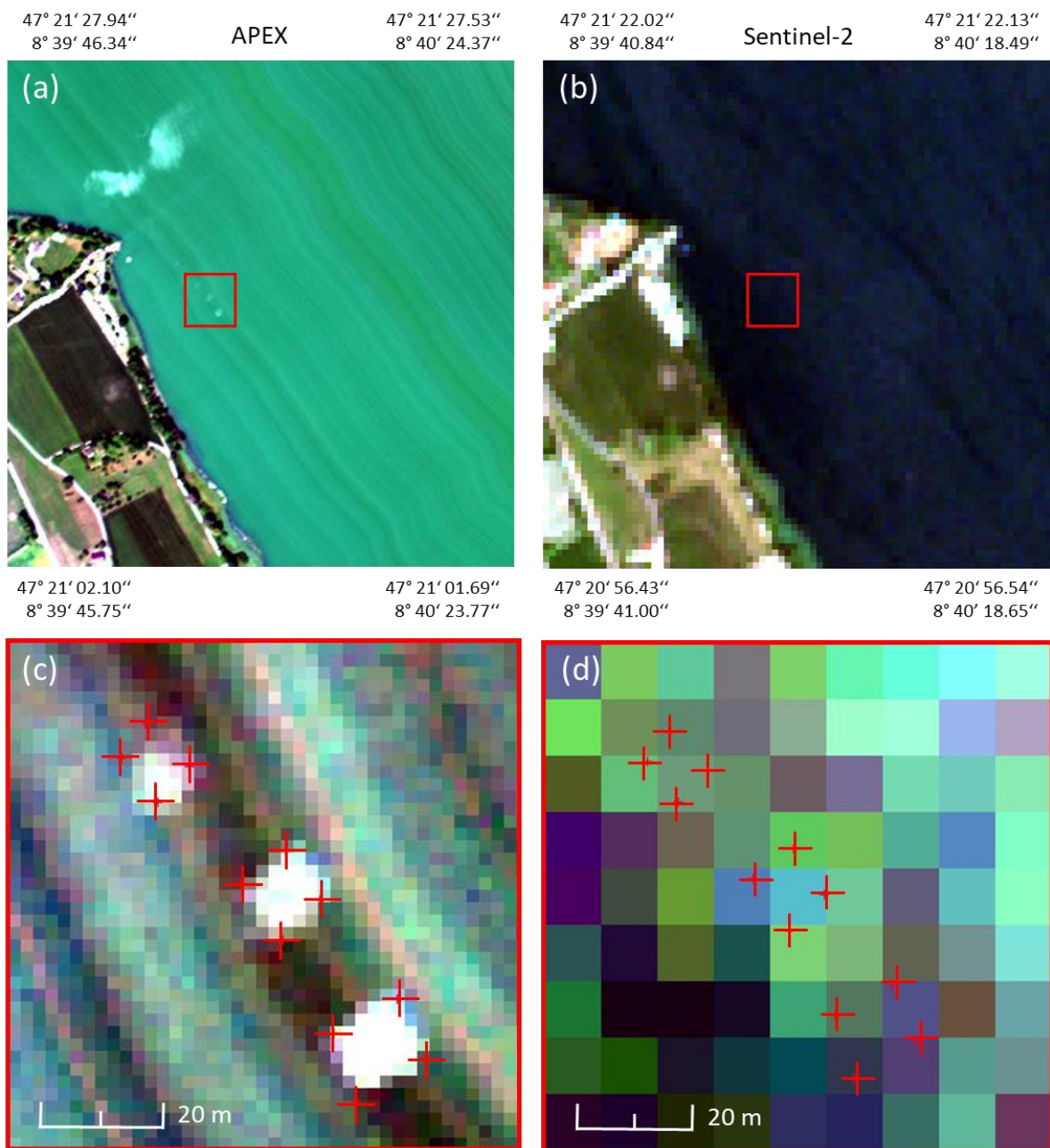


Figure 3-3: RGB visualisations of the Greifensee location. (a) shows the APEX radiance values of the spectral bands 8 (blue), 18 (green) and 43 (red). The Sentinel-2 true colour reflectance satellite image shows bands 2 (blue), 3 (green) and 4 (red). The zoomed details of the APEX (c) and Sentinel-2 (d) subsets are overlaid with the corner positions of the PET test fields.

The spatial subsets of the data from both the APEX hyperspectral and the Sentinel-2 multispectral satellite sensor, both acquired within less than 2 hours over the same plastic test fields at the Greifensee location are presented in *Figure 3-3*. These true colour representations provide a first impression especially of the spatial resolution inherent in such imagery. The "true" colour of the lake however was a greenish-blue to the human eye, thus a colour just between the two appearances in these images. Quite astonishingly, the PET test areas are distinguishable even in the unmodified APEX RGB image. Close to the tiny delta (bright due to a bright gravel surface), a floating raft of plastic material is also distinguishable in the APEX image. The two "cloudy" patches further north over the water originate from a campfire. These smoke clouds were not noticed at the time of the satellite overpass. The striped pattern in the APEX data are precisely coherent with the flight path (southeast to northwest). They represent an unwanted but well-known sensor artefact that cannot be completely eliminated during processing (Rogass et al., 2012). The enlarged sections show the water area where the three PET test fields were deployed (location highlighted by red rectangles in the subset images). For *Figure 3-3* (c) and (d), linear histogram stretching was applied on each spectral band for contrast enhancement.

3.3.1 Clustering

When choosing a classification method, essential considerations always play a decisive role, such as: What is the nature of the problem? What are the characteristics of the study area? What is known about the class(es) to be identified, including their distribution in the image (Jensen, 2016)? In the present case, the aim is to apply a simple unsupervised algorithm for target discrimination based on data statistics only, with the main objective to establish whether there is a statistical pattern inherent in the imaging spectroscopy data that would allow to find specific similarities in those pixels where the PET bottles contribute a small fraction to the spectral signal – in contrast to the surrounding smooth water surface where no other object was afloat at time of data acquisition. Furthermore: Is it possible to identify a scaling effect of the varying PET surface abundances?

K-means is one of the most common clustering methods in remote sensing and a common approach used in image analysis (Richards, 2013). It is an iterative optimisation algorithm, based only on data statistics aiming at identifying pixels in an image that are spectrally similar. The only parameter the analyst needs to provide consists of the number of clusters to which the image pixel vectors are to be assigned. In a "typical" classification task, this information may be gained from visual image interpretation, ideally combined with prior knowledge on the typical land surface categories present at the image location. For our location with the small floating PET bottles setup, however, the image features of interest are restricted to these differently small surface fractions of plastic.

The data were clustered using the k-means functionality in ENVI. Regarding the ideal number of clusters for a best possible result, the k-means algorithm was run several times for varying number of clusters. Furthermore, the algorithm was run in a first evaluation series using all spectral bands. In a second evaluation series, only 3 image bands were selected based on previous knowledge about specific wavelength positions around a known absorption feature of plastic materials. The APEX bands 183 (1667 nm), 190 (1728 nm), and 197 (1788 nm) were closest to the selected bands indicated in a successful mapping approach (Hörig et al., 2001). All results were generated after 3 iterations. The colours for visualisation were assigned randomly by the software.

The classified images were then assessed, based on a manually defined "ground reference" file for which the GPS location information and visible brightness differences in the image were used. For this purpose, all resulting images of each evaluation series were stacked together with the reference file, exported into MATLAB and evaluated by an algorithm specially developed. The evaluation logic was intentionally adapted to the

peculiarities of this classification, as the focus was placed solely on the three test areas. Defining the three different PET abundancies of mixed pixels as separate classes contradicts the basic logic of such classification, and thus a standard quality assessment. Nevertheless, this approach was intentionally chosen here, as the advantages of the first insights seemed to outweigh the disadvantages. When interpreting the unusual accuracy assessments, however, it must be noted that the user accuracy was summarized in one class, because an error within different plastic abundancies should not be treated misclassified here. A selection of the k-means results together with the accuracy metrics is shown in *Figure 4-7*.

3.3.2 Band ratioing and indexing

Band ratios and indices allow to combine spectral information from two or more bands, using a mathematical expression which will be applied on every image pixel, known as ratioing (Prost, 2014). The resulting image contains the calculated values in one single band. The main advantage of band ratios is that brightness differences due to terrain or shadow effects within an image are ratioed away while the spectral information remains. This can be useful for discriminating subtle variations in the spectral properties of materials that are obscured by brightness variations (Lillesand et al., 2008). As an added benefit, ratios provide normalized values that enable comparisons between different image data.

Indices are most useful when it comes to separating image features with well distinguishable spectral values in the selected bands. Many indices have been developed, most abundantly for vegetation analysis, and many are normalized indices based on ratios. Since plastic materials show specific absorption features with absorption maxima around 931, 1200, 1420, 1730 and 2310 nm (Cloutis, 1989; Hörig et al., 2001; Garaba and Dierssen, 2018), indices have also been developed for identifying these materials.

Although the 1730 nm feature is very close to a major atmospheric water absorption maximum, and radiance values are extremely low at this spectral range, the **Hydrocarbon Index (HI₁₇₃₂)** has been developed to be used for hydrocarbon material detection, similarly to the Normalized Difference Vegetation Index (NDVI) for vegetation identification and characteristics (Kühn et al., 2004). This first hydrocarbon index has been developed for HyMap bands at wavelengths 1705 nm, 1729 nm, and 1741 nm, usable with both reflectance and radiance data, and is claimed able to detect any hydrocarbon-bearing materials where HI values are > 0 (Kühn et al., 2004). This includes most plastics. Plastic sheets, oil contaminated sand, and artificial grass could successfully be identified as hydrocarbons, but the index did not work for plastic roofs (Kühn et al., 2004). However, no specified lower limit of surface abundance was reported, nor was the index applied on water surfaces. The Hydrocarbon Index is, to our best knowledge, the only approach in remote sensing for plastic detection, documented in the scientific literature.

(1)

Applying a very similar index formula, another **Hydrocarbon Index (HI₁₂₁₅)** has been developed, using the absorption feature around 1215 nm with the AVIRIS radiance bands at 1197, 1215 and 1235 nm (Garaba and Dierssen, 2018). In this recent study, both Hydrocarbon Indexes were applied and showed “several man-made targets with moderate to strong concentrations of hydrocarbons or plastics” (Garaba and Dierssen, 2018).

(2)

Based on these two hydrocarbon indices documented in the scientific literature, a specific "PET Index" was newly developed for the present analysis. It takes into account the shifted material-specific wavelength position for PET. Although this new index is based on the aforementioned formulas, it was defined empirically on the basis of the AVIRIS-NG image radiance spectra (because of this sensor's highest spectral resolution). Attempts to normalise this newly developed index have been made, but they have failed.

(3)

The theory behind these indices – and the explanation why no normalization could be achieved – is sketched in *Figure 3-4*. The indices combine the values from three spectral bands, which would typically contain the values of the two absorption shoulders (local radiance maxima) as well as the absorption maximum of an absorption feature, as illustrated in (a). Considering the relative value differences (or ratios) between shoulders and absorption maxima allows for normalized index values where brightness differences are eliminated. However, the specific spectral curve properties of plastic and water which form the basis of the index calculation in this case show a different picture. The sketch (b) is based on the spectra presented in *Figure 5-5* and the bands used for the Pet Index definition. It depicts the very small relative value difference between absorption maximum and shoulder. The more obvious difference in the two spectral curves is indicated as absolute value difference, because the effective radiance values of these bands are added to the Pet Index so that these absolute value differences highly add to the resulting index value. Finally, the theoretical justification of the initial Hydrocarbon Index is supplemented in (c).

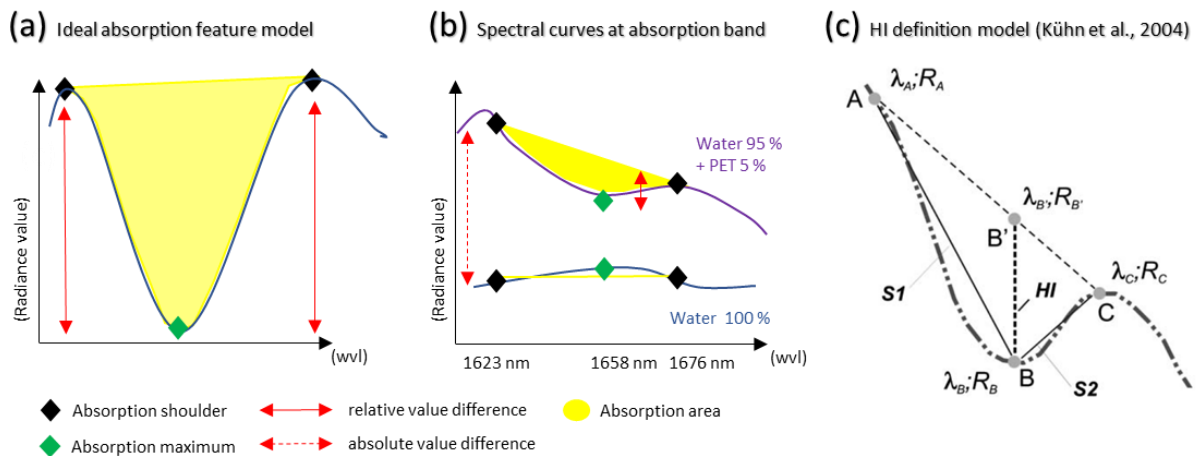


Figure 3-4: Index calculation theory: Absorption feature model vs. spectral curves of mixed plastic-water and water spectra.

Equations (1) to (3) were calculated for radiance data using the ENVI Band Math Tool. APEX radiance bands with the nearest central wavelength to the suggested index bands were selected, as summarized below. In addition, for sensor comparison reasons and because of some promising first results, the same equations were also calculated for the AVIRIS-NG radiance Hallwilersee subset image (presented in the following Section 3.4) where slightly different wavelengths were selected.

Table 3-1: Selected bands for index calculations, including the ENVI Band Math formulas. For brevity, the band wavelength is noted without digits.

Index	spectral range	APEX bands	AVIRIS-NG bands	ENVI Band Math formula
HI ₁₂₁₅	1193 - 1235 nm	b1 = 133 (1194 nm) b2 = 135 (1213 nm) b3 = 137 (1233 nm)	b1 = 164 (1193 nm) b2 = 168 (1216 nm) b3 = 172 (1235 nm)	$I = (\text{float}(b3 - b1)) * 0.5 + b1 - b2$
PET-I ₁₆₆₅	1623 - 1676 nm	b1 = 178 (1623 nm) b2 = 182 (1658 nm) b3 = 184 (1676 nm)	b1 = 250 (1624 nm) b2 = 258 (1665 nm) b3 = 260 (1674 nm)	$I = b1 + b2 + (\text{float}(b3 - b2))$
HI ₁₇₃₂	1702 - 1737 nm	b1 = 187 (1702 nm) b2 = 190 (1728 nm) b3 = 191 (1737 nm)		$I = 2 * (\text{float}(b3 - b1)) / 3 + b1 - b2$

No quantitative **result evaluation** was performed for these index results, as no obvious index value ranges were able to clearly separate the pixels containing plastic. It turned out that a possible classification based on index values (by means of density slicing) is highly dependent on the definition of the class boundaries, which will differ from image to image, especially when radiance data is evaluated as these indices are not normalized indices. For result comparison, however, density slicing was applied as defined in the table below. Colour density slicing is a method to map a range of brightness values to a single display value, thus to segment a scalar image into distinct classes, in order to highlight fine differences or make details apparent (Richards, 2013).

Table 3-2: Defined index value ranges for selected density slice ranges of the APEX result images (shown in Figure 4-8).

Index	image	Index result range	Defined density slice ranges			Assigned colours		
HI ₁₂₁₅	(b)	-0.147149 - 4.671032	-0.20 - 0.04	0.10 - 0.12	2.30 - 3.80	cyan	yellow	red
HI ₁₇₃₂	(e)	-0.108471 - 1.701036	-0.20 - 0.02	0.36 - 0.50		cyan	red	
PET-I ₁₆₆₅	(h)	0.469396 - 2.659658	0.00 - 1.53	1.53 - 1.60	2.20 - 2.70	cyan	yellow	red
PET-I ₁₆₆₅	(i)	0.700347 - 2.656569	1.25 - 1.50	1.50 - 2.70	1.53 - 1.80	yellow	red	orange

3.3.3 Supervised Classification

Classification algorithms are often distinguished by the level of information provided by the analyst. While unsupervised classification (e.g., k-means clustering) is based entirely on statistical properties of the data, supervised classification requires training classes defined by the analyst or selected from ground reference areas with known surface material (Prost, 2014). Training classes are sets of pixel data vectors that are typical for the classes to be classified. Unclassified pixels are being compared to the training classes, and, depending on the algorithm applied, will be assigned to the spectrally most similar class. Supervised classification results therefore depend primarily on the definition and fitness of the training classes employed.

Many **different algorithms** exist. **Commonly applied algorithms** are: Maximum Likelihood, Minimum Distance, Parallel-piped, and Spectral Angle Mapper (ENVI, 2002). The widely used Maximum Likelihood algorithm requires a minimum number of reference pixels per training class because it uses covariance information (Richards, 2013). This requirement is not met by all the small PET test

areas. In the case of insufficient training class samples, the **Minimum Distance algorithm** can be applied since it does not need the covariance information. It calculates the minimum Euclidean distance from each pixel to the mean vector for each training class (ENVI, 2002).

Minimum Distance Classification: Here we try to find the mixed-pixel areas solely on the basis of spectral similarities between mean reference spectra, selected from the image itself, and the image pixel spectra. Since the unsupervised k-means algorithm was able to discriminate between the test areas and the surrounding water, it can be expected that a supervised classification algorithm finds this distinction in the same data as well. Therefore, the main objective of this step is to find out whether different PET abundances can also be distinguished, even if no method specialising in mixed-pixel analysis is being applied. Here, too, the chosen method does not correspond ideally to the task at hand, because in principle, the reference classes should not spectrally overlap for this method (Richards, 2013). The three training classes of varying plastic abundance certainly overlap spectrally. In this explorative approach the algorithm has nevertheless been used, and certain knowledge of the material sought was taken into account additionally through the selection of input bands.

Training classes: For the APEX radiance subset image, the location of the floating plastic is precisely known. Thus, training classes were defined from the three different target surface areas and from the surrounding water surface without plastic. Two sets of ground cover type classes were defined, manually applying a stratified random sampling scheme¹²:

- ◁ The first set contains two classes, aiming at the only distinction between water and PET test areas. From all three test areas, the central pixels were selected to form one training class (30 pixels), while the water training class (30 pixels) contains pixels around the test areas at assumingly comparable mean water depths.
- ◁ The second set contains four classes, where 12 pixels each were selected from the test areas to define (sub-) training classes with varying plastic abundance. The fourth class again contains surrounding water pixels.

In theory, many considerations refer to the optimal size of training classes for algorithms without specific training class requirements. In the present case, however, there is little room for manoeuvre, since this is not a typical supervised classification task either, but rather an experimental application of a method that is not specifically tailored to low target abundances or even subpixel scaling issues.

Input bands: For both training sets, the algorithm was run with varying input band combinations, using the ENVI functionality with standard settings to classify all image pixels (no standard deviation nor distance threshold was defined). For comparison reasons, the three single bands used in the k-means clustering (*Section 3.3.1*) were selected for run 2. In this method, the Minimal Noise Fraction (MNF) bands were also used as input variants. However, this is the only (exemplary) evaluation based on this transformed image data because the results were below expectations. While the aim in the first runs is rather explorative, special interest lies in the four spectral regions of the known plastic absorption features. The spectral absorption feature ranges as defined in (Garaba and Dierssen, 2018) were used to define the band selections for run 5 – 8.

¹² Stratified random sampling involves two steps: First, the image subset is divided into the surface classes of interest. Then, a minimum number of samples per surface class is selected randomly (Jensen (2016)).

Overview of the input band selections for both training class sets:

1. All spectral bands (299 bands)
2. Selected spectral bands as in the k-means classification: band 183 (1667 nm), band 190 (1728 nm) and band 197 (1788 nm)
3. All MNF bands (299 bands). While input band reduction would be the goal using MNF bands, this run using no reduced data volume was intended for comparison with run 1 only.
4. Selected MNF bands, containing the most image information but omitting those bands containing mostly sensor artefact patterns (bands 6, 7, 8) and noise: MNF bands 1 – 50, except bands 6 – 8.
5. Absorption feature at 931 nm: bands 95 – 110 (880 – 980 nm range)
6. Absorption feature at 1215 nm: bands 125 – 144 (1100 - 1300 nm range)
7. Absorption feature at 1417 nm: bands 150 – 165 (1400 – 1500 nm range)
8. Absorption feature at 1732 nm: bands 181 – 200 (1650 - 1800 nm range)

For **assessing the accuracy** of the algorithm results from both training sets, another MATLAB script was developed to analyse all runs together with the labelled test data sets and training classes, and to create the accuracy metrics visualisations. The evaluation logic was – as described in the k-means example (*Section 0*) – again adapted to the peculiarities of this unusual classification problem. The assessment results are presented together with the classification results in *Figure 4-10 and Figure 4-11*.

3.3.4 Outline

Both the unsupervised k-means and the supervised Minimum Distance classifications applied to airborne data in this subsection clearly demonstrated that a distinction between the plastic test surfaces and the surrounding water surface is indeed achievable even for the smallest PET abundance of approximately 1%. This is an answer to the research question (1) regarding the detection limit. However, the results are ambiguous, which can be explained in part by the inhomogeneity of the water surface along the shore, by lake depth variations, and by the observed sensor artefacts. Furthermore, it must be assumed that the differences found are predominantly based on differences in brightness and do not allow unambiguous indication of specific plastic components.

As for the satellite data, indications towards answering research questions (2) and (3) regarding spatial and spectral sensor resolution requirements were found, however indirectly. But since the available test imagery does not cover larger spatial areas, and geometric accuracy did not allow any certain selection of the pixels containing the PET signals, no further evaluations of the Sentinel-2 imagery were carried out after a few pointless clustering attempts (not documented here in detail). At all, due to the limited spectral resolution (as visualized in *Figure 4-3*), it was also not expected that the satellite data would provide any major surprises.

The use of the established Hydrocarbon Indices showed disappointing results, whereby the assumption here is that the plastic abundance in the test data is insufficient for successful application. While this indication also points towards answering research question (1), a more elaborate evaluation method will be applied to the same plastic absorption features in the following subchapter, making use not only of single band values but also of the spectral curve characteristics.

3.4 Plastic identification

In this method subsection the focus is now on plastic detection approaches, where methods of imaging spectroscopy are applied. These are analysis methods for high spectral resolution data containing continuous bands over the VIS, NIR and SWIR spectral ranges. In particular, these methods are specialized to enable information extraction in the sub-pixel range. Here, the focus lies on the following points:

- ◁ **Location:** Data from both the previously presented locations are considered again. In addition, data from the Hallwilersee site are taken into account. They differ above all with regard to the weather situation: The test areas were exposed to wind (Beaufort 2 – 3) and waves, which is why the PET targets were wet or even partially submerged. Also, the water surface was agitated, resulting in small-scale geometry variations of the air-water interface, making this test setup probably the most realistic.
- ◁ **Sensors and data products:** Mainly L1 radiance data are analysed. These comprise two APEX image subsets (Irchel and Greifensee locations) with the highest spatial resolution, and two AVIRIS-NG image subsets (Irchel and Hallwilersee locations) containing the highest spectral resolution of the available imagery.
- ◁ **Methods:** The chosen approaches in this subsection basically ground on two underlying ideas: First, two methods which take the most promising approaches from the previous subsection one step further are applied: The Spectral Angle Mapper (SAM) method focuses on spectral similarity, while the Continuum Removal (CR) algorithm focuses on specific absorption features. Second, the fact that the floating plastic targets make up only a tiny part of the corresponding pixel spectrum, mixed pixel considerations (e.g., SMA) must be a fundamental part of every more sophisticated approach.
- ◁ **Research focus:** Now it's about the detectability (and possibly mapping) of specific plastic materials, while abundance estimations and more realistic settings - wet targets and agitated water surface - are also evaluated. First indications towards answering research question (4) on environmental influences are expected here, while more specific results are expected with regard to the other research questions.

The Hallwilersee test location differs from the other two in several points. The flight strips over the test area of this lake were overflown twice with the AVIRIS-NG sensor, and with two of the planned flight strips overlapping at the selected test site, this resulted in 4 imaging spectrometer images. The flight strip was flown twice because of cumulus clouds which blocked the view downwards on this rather windy day. This wind also made it difficult and very time-consuming to deploy the test areas on a lake at wind force 2 without prior practical experience. This is why only two of the three test fields could be installed during the morning prior to data acquisition. However, this test installation probably comes closest to reality at sea, because most of the bottles were constantly washed over by waves and were mostly wet - if not submerged - at the time of data acquisition.

Important observations to this image subset below are: The test area is right at the outer edge of the image strips, which can be recognized from the (irregular) northern image margin containing zero values (black pixels). Furthermore, the bright shore areas can in principle be attributed to two causes: It is possible that a small cloud has covered this image area, or this is a sun glint effect. **Sun glint** effects are caused by direct specular reflection of sunlight off the water surface into the FOV of the sensor, resulting in an oversaturation of the pixel values that are manifested as extremely bright image areas. The factors affecting sun glint are acquisition geometry related, that is, the relative position of the Sun, the viewing angle of the sensor, and water surface geometry, since rougher water surfaces create more angles for the light to reflect off (Emberton et al., 2016). Avoiding sun glint

is regarded as a most important factor in optical remote sensing of water surfaces and can be avoided best by flying within 10° of the solar azimuth during data collection and by acquiring data only in a specific range of solar elevation between 30° and 50° (Miller, 2005). A sun glint effect is possible here since the ideal illumination geometry was narrowly missed. What the bright effect really is could be clarified or at least narrowed down by analysing the spectrum. However, this was not done because it is of no further relevance here.

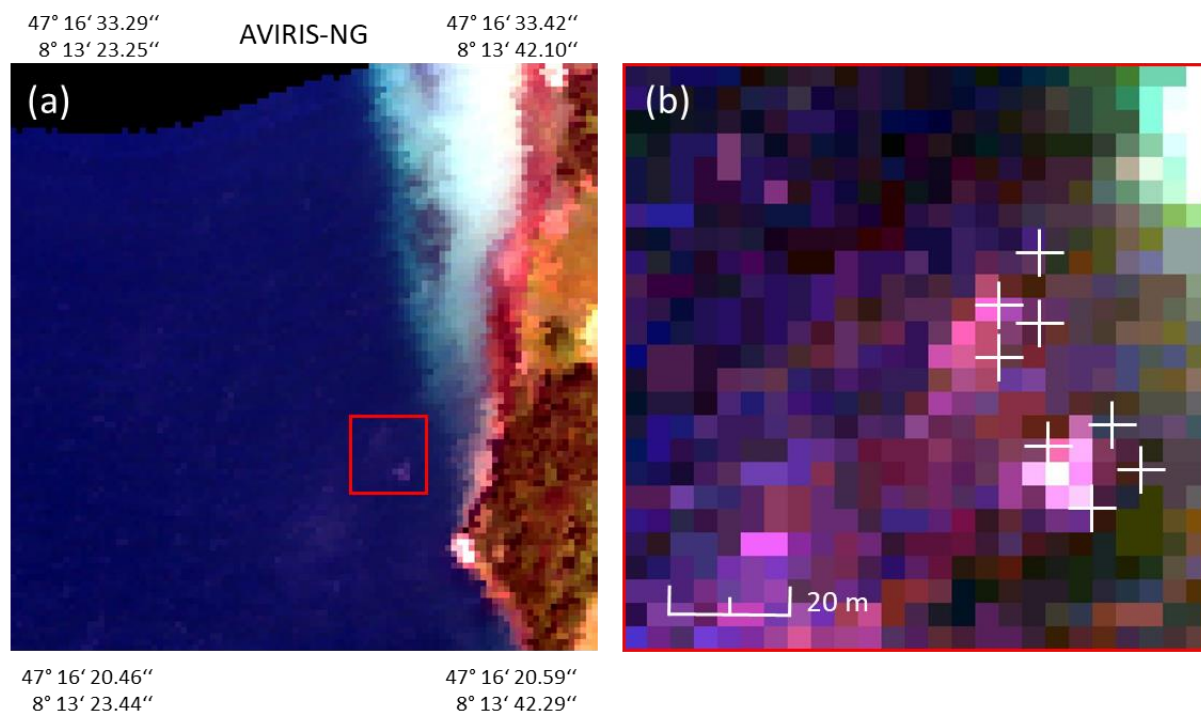


Figure 3-5: RGB visualisations of the AVIRIS-NG geo-rectified radiance image containing the Hallwilersee location. The subset is rotated, showing the image strip edge north of the experiment location (a) and the slightly shifted brighter PET test areas as compared to their measured GPS corner positions indicated by white cross symbols in the enlarged detail (b). Both visualisations are RGB true colour representations (R: band 54, G: band 36, B: band 18).

3.4.1 Spectral Angle Mapper

The Spectral Angle Mapper is a physically based algorithm, using an n-dimensional angle to match n-dimensional image pixels to a reference spectrum in the same n-dimensions. It is therefore a comparable algorithm to the Minimum Distance classifier, however designed for imaging spectroscopy data. And while a pixel value contains both a magnitude and angular direction, here, only its angular direction is analysed (Richards, 2013). This can be regarded as an advantage over the Minimum Distance classification, since brightness differences should not impact its accuracy. The spectral similarity is determined by calculating the angle between the spectra by treating them as vectors in a space with a dimensionality equal to the number of spectral bands. The smaller the resulting angle, the higher is the spectral similarity. While for each reference spectrum, a SAM output image containing the angle values originally results from the algorithm, it is possible to convert these output images into one classification map where all pixels are assigned to the class with the smallest angle, as long as the angle is below a specified threshold (Jensen, 2016; ENVI, 2002).

This supervised classification algorithm was applied extensively to all available radiance images. Since a threshold was defined for each evaluation, masking of the image subsets was not required. **Reference spectra** were derived directly from the images by manually defining so-called Regions Of Interest (ROI's) in each of the image subsets, consisting of 20 – 30 and 4 – 12 pixel values each for the APEX images and the AVIRIS-NG images, respectively. These ROI's contain all image pixels from the 3 PET test areas as well as a selection of surrounding water pixels with similar average water depths. For each image, the mean of these ROI's were calculated in MATLAB and stored in the SPECCHIO database for repeated use (and evaluation). They were then imported into ENVI again as SLIB (spectral library) files and used as reference spectra for the algorithm. For classification, a specified maximum spectral angle threshold was applied: After evaluating the rule images of several threshold variations, a single **threshold of 0.08 radians** for all classes was defined. The class colours were manually assigned using the meanwhile standardized red, orange, and yellow colours for the PET test field abundances. In view of the result discussion, various factors were then varied: The maximum spectral angle threshold; the spatial subset area; and - analogous to the k-means and minimum-distance evaluations - the spectral range was constrained.

For **assessing the accuracy** of the algorithm results, another MATLAB script was developed to analyse all results based on the reference images and to create the accuracy metrics plots. For the Greifensee location, the same reference image was used as for the Minimum Distance method. For the Irchel and Hallwilersee locations, reference images were derived based on the relevant vector files and distinguishable brightness differences in the histogram stretched images. The evaluation logic was – as described in the previous examples (*Sections 0 and 3.3.3*) – again adapted to the peculiarities of this unusual classification problem. However, this time the user accuracies were evaluated for each of the PET abundancies separately, because here the exact allocation to the PET abundancy class, according to the reference pixel, is expected. This makes the result values less clear, but they allow differentiated assessments of the individual abundancies.

3.4.2 Continuum Removal

In the previous Hydrocarbon Index evaluation (*Section 3.3.2*), the only reference information on the plastic absorption features consisted in selecting certain spectral bands as input for the algorithm. Now, the shape and size of the (normalized) absorption features, as defined by the spectral curve in that relevant spectral region, are also taken into account. This relates to the method category (iv), as outlined at the beginning of *Section 3.1*. Therefore, while using the same spectral absorption region, better results can be expected here than with the index calculation. This advantage however requires spectrally continuous imaging spectroscopy data, which is not a strict requirement for index calculations in general.

Continuum Removal (CR) analysis is a method usually applied to L2 reflectance imagery (Jensen, 2016; Qu and Liu, 2017). It allows identification and comparison of individual absorption features and utilizes spectral data subsets of the relevant wavelength regions as input. This method enhances subtle absorption features and may improve separability of spectrally similar classes (Jensen, 2016), as is the case here for the mixed water and PET pixels of the test areas. Although this method is intended for reflectance spectra, it has also been specifically applied - for the very detection of floating plastic debris - on radiance data (Garaba and Dierssen, 2018). Radiance data is preferable in order to avoid the loss of information by the usual atmospheric correction algorithms over water surfaces. Consequently, the CR method is systematically applied here to both data products.

A convex hull fit over the top of a spectrum defines the continuum, with straight line segments connecting local spectrum maxima (ENVI, 2002). CR normalizes spectra from this common baseline, that is, the local peaks in the spectrum (absorption shoulders). These should be the first and last bands in the spectral subset and are set equal to 1.0 for normalization of the continuum-removed spectrum (Jensen, 2016).

The continuum-removed spectral bands were computed for the plastic absorption features at 1215 nm and 1665 nm, using ENVI's Continuum Removal spectral mapping function. Subsequently, ENVI's Band Math tool was used to integrate the area inside the continuum-removed curve under the hull between the two absorption shoulders. Equation (4) for AUC (area under curve) was used where n is the number of spectral bands of the spectral subset, $1-CR_j$ and $1-CR_{j+1}$ are the values at the j and $j+1$ spectral bands, and λ_j and λ_{j+1} are the band wavelengths [nm]¹³.

(4)

The selected spectral subset of the HI₁₂₁₅ absorption region consists of 9 AVIRIS-NG bands (1193 – 1233 nm, bands 164 – 172) and 5 APEX bands (1194 – 1233, bands 133 - 137), respectively. For the PET-I₁₆₆₅ absorption region, 11 AVIRIS-NG bands (1624 – 1674 nm, bands 250 – 260) and for the HI₁₇₃₂ region, 5 APEX bands (1702 – 1737 nm, bands 187 - 191) were selected. The first and last band of each spectral subset correspond to those that were used as input bands for the index calculations. The defined spectral ranges, bands, and AUC calculation formulas are compiled in the table below.

Table 3-3: Spectral subset definitions and ENVI Band Math formulas for CR calculations.

Spectral subset	feature	spectral range	bands	ENVI Band Math formula
APEX (L)	HI ₁₂₁₅	1194 - 1233 nm	133 - 137	AUC=(((1204.1230-1194.4000) * ((1-float(b2))+1-float(b1)))) + ((1213.9430-1204.1230) * ((1-float(b3))+1-float(b2)))) + ((1223.7581-1213.9430) * ((1-float(b4))+1-float(b3)))) + ((1233.4690-1223.7581) * ((1-float(b5))+1-float(b4)))))*0.5
APEX (L)	HI ₁₇₃₂	1702 - 1737 nm	187 - 191	AUC=(((1711.0100-1702.2740) * ((1-float(b2))+1-float(b1)))) + ((1719.7460-1711.0100) * ((1-float(b3))+1-float(b2)))) + ((1728.4830-1719.7460) * ((1-float(b4))+1-float(b3)))) + ((1737.2190-1728.4830) * ((1-float(b5))+1-float(b4)))))*0.5
AVIRIS-ng (L, R)	HI ₁₂₁₅	1193 - 1233 nm	164 - 172	AUC=(((1198.2800-1193.2700) * ((1-float(b2))+1-float(b1)))) + [...] + ((1233.3400-1228.3300) * ((1-float(b9))+1-float(b8)))))*0.5
AVIRIS-ng (L, R)	PET-I ₁₆₆₅	1624 - 1674 nm	250 - 260	AUC=(((1629.0300 – 1624.0200) * ((1-float(b2))+1-float(b1)))) + [...] + ((1674.1100 – 1669.1000) * ((1-float(b11))+1-float(b10)))))*0.5

¹³ This approach, including the integration formula, is based on exercise 10 (chlorophyll content estimation) within the framework of the lecture «Geo442 - Spectroscopy of the Earth System» at RSL / UZH, 2017.

As for the index calculations, no quantitative **result evaluation** was performed, since no obvious CR value ranges were able to clearly separate the pixels containing plastic. However, for the APEX results, density slicing was applied to highlight one specific finding. The density slicing range definitions are summarized below:

Table 3-4: Defined CR value ranges for selected density slice ranges of the APEX result images.

Feature	image	CR result range	Density slice ranges		Assigned colours	
CR _{1194 - 1233}	(c)	0 - 5.4679	3 - 4	4 - 6	yellow	red
CR _{1702 - 1737}	(d)	0 - 7.3647	3 - 4	4 - 8	yellow	red

3.4.3 Spectral Mixture Analysis

Not only floating plastic items become part of spectrally mixed pixels. Essentially, the spectrum of any remotely sensed image pixel is a mixture of so-called endmembers, that is, spectrally pure pixels containing the spectral signal of physically meaningful scene materials (Manolakis et al., 2016; Kneubühler et al., 2007). Therefore, the analysis of mixed spectra is an important application for image interpretation and subpixel target detection in imaging spectrometer images. Two general questions are tackled with this method: (a) what materials are contributing to a mixed pixel, thus, what are the spectra of these endmembers? And (b) what are the proportions of these individual endmembers?

This approach seems to fit perfectly to the situation here, because the plastic bottles searched for represent small proportions of mixed pixels covering mainly lake water. For this reason, the use of methods based on spectral mixture analysis was considered to be the methodologically "most correct" approach from the outset.

But the evaluation planned here turned out to be a bigger hurdle than expected. This was mainly because the available data do not sufficiently fulfil the basic conditions for the application of such methods specifically designed for mixed pixels analysis. The first and most crucial step in spectral unmixing analysis is to find "good" endmembers which are typically determined from the image data. However, spectra must be spectrally distinct (linearly independent) from one another because collinear endmembers lead to "numerically unstable unmixing" (Manolakis et al., 2016). Moreover, the **Linear Spectral Unmixing** method requires all endmembers of materials that are present in the image (ENVI, 2002). Since these conditions could not be met for both the Greifensee and the Hallwilersee locations, another similar method seemed more applicable: **Mixture Tuned Matched Filtering** (MTMF) is a partial unmixing approach where not all of the endmembers in the image need to be known, providing a means of detecting specific materials based on matches to endmember spectra. However, this method requires the MNF transformed image bands and input spectra must be pure and spectrally extreme endmembers that are equally transformed (ENVI, 2002). Since previous mapping results with the MNF transformed image data yield substandard results and reference endmembers could not be extracted from the transformed image (at least not for the PET material which does not occur as "extreme and pure" pixels within the image), this option was only applied using a semi-automated process (ENVI's Mapping Wizard) which allows minimal user control over the entire evaluation process. Since the result was indeed disappointing and not worth documenting, it is only the infeasibility information from that approach that was added to the results section for pointing towards the limits of this approach.

Finally, the **Matched Filtering** method was applied, where there is a risk of more false positives for rare materials, but no MNF transformed image data is required as input. It is a somewhat simplified variant of the MTMF, in which however the potentially meaningful infeasibility image is not generated as the result

component (ENVI, 2002). The problem of the not pure and non-uniform water spectra remained. However, the relevant endmember reference spectrum for PET could be derived from field measurements. This was done despite the explicit warning that comparing remotely sensed spectra with reference measurements from another location, measured under different illumination conditions and with yet a different sensor “is no small matter” (Jensen, 2016) and requires “considerable experience with the pertinent application” (Manolakis et al., 2016). For the implementation here, the use of radiance data represents an additional hurdle, since it is not possible to fall back on standard reflectance reference spectra that are insensitive to illumination variations. The radiance endmember for PET material with the APEX sensor’s spectral resolution was calculated as described in the spectral mixing model (*Section 3.5.1*), then stored in the SPECCHIO spectral database for documentation and repeated use, and extracted as spectral library file (ENVI SLIB file format).

3.4.4 Outline

The results of the methods chosen in this section contain some surprising findings. Comparisons of equivalent outcomes on APEX and AVIRIS-NG data may not be a priority with regard to the research questions, but they are certainly interesting in terms of the radiometric quality of these sophisticated instruments. Expectations of better mapping results were rather disappointed. Yet the studies conducted so far do form a good basis for assessing the detectability options and also indicated possible further directions with regard to augmented test data and experimental environment requirements. The last chapter on methods accordingly concentrates on complementary theoretical approaches.

3.5 Spectroscopic models

In this concluding method part, theoretical analyses based on reference spectra are added. To pick up again the subject of satellite data and in order to evaluate the minimum requirements for spatial resolution, a previous discrimination approach is carried out again on spatially upscaled APEX data.

Here, the focus lies on the following points:

- ◁ **Sensors and data products:** Selected APEX radiance spectra and ASD field reference spectra are investigated.
- ◁ **Methods:** A linear spectral mixing model was created to model abundance variations of water and PET between 0% – 100%. Based on this model, the PET abundancies of the three test areas could then be verified. Derivative spectroscopy was further applied in exploratory approaches for spectral feature determination and plastic absorption band position evaluation: The method, results, and discussion thereof are documented in Appendix B since this approach provides a tool for further analysis rather than a new finding in this instance.
- ◁ **Research focus:** The verification of the test area abundancies is an important part regarding research question (1) which now can be answered more precisely, and the spatial scaling experiment concerns research question (2).

3.5.1 Spectral mixing model

A spectral mixture model is physically based on pure spectra or endmembers. Mixed spectra of these endmembers are then modelled as combinations of them (Manolakis et al., 2016). Most spectra of remotely

sensed data contain a mixture of surface materials, as is the case for the floating PET bottles on the water surface. The proportion in which these materials contribute to the resulting image pixels are called fractional abundances (Keshava and Mustard, 2002). Usually in spectral mixing, a linear model is applied using the equation formula (5) for a linear mixing of m components where \mathbf{s}_k is the spectrum of each endmember and \mathbf{a}_k its fractional abundance. The residual \mathbf{e} includes measurement error, noise, and contributions from any endmember that may add to the mixed pixel signal but has been left out in the endmember selection. This residual is relevant due to the sum-to-one (and nonnegativity) constraints of this model (Manolakis et al., 2016).

(5)

Using ASD field reference spectra, a linear spectral mixing model was computed in MATLAB to model mixing variations of water and PET mixtures in steps of 1% from 0% PET and 100% water to 100% PET and 0% water abundance. The computational steps included: Selection of a Spectralon ASD radiance with best approximation of the illumination conditions of the day, time, and location of airborne data acquisition from the SPECCHIO database. This reference spectrum was corrected using a correction vector¹⁴ specific for the near-perfect reflectance properties of the white Spectralon panel. Also, the field reference measurements (*Section 2.2.4*) of floating PET bottles (that totally covered the water surface) were selected from the SPECCHIO database and their mean reflectance spectrum was calculated. Based on these ASD spectra, the PET radiance spectrum was determined in accordance with the illumination conditions of the day of airborne data acquisition and interpolated to the APEX sensor's spectral resolution.

Based on this linear mixing model, the **plastic fractions of the 3 PET test fields** were then evaluated by comparing the mean radiance spectra from the APEX image data with the most similar mixture variants. The calculated radiance endmember spectrum for PET material was also used as reference for the Matched Filtering method in spectral mixture analysis (*Section 3.4.3*).

3.5.2 Spatial scaling

As expected, no systematic difference between the relevant pixels of the water surface area could be found in the satellite data, as can be seen in the visualisations of the bands with best spatial resolution of 10 m (*Figure 3-3 (b)* for a RGB visualisation, and *Figure 4-6 (c)* for a CIR visualisation). However, it has not yet been verified whether the cause lies in the low spatial resolution or the lower spectral resolution. Therefore, as is usual with such research designs, one of the two varying parameters is held static while the other is scaled in such a way that different datasets can be compared with a resolution difference in only one dimension.

For this purpose, the APEX subset was spatially upscaled, resulting in a still hyperspectral subset with the lower spatial resolution of satellite data. The k-means classification as applied previously based on the same three selected spectral bands was applied again. Using a range of upscaled pixel sizes (and thus slightly varying image subset sizes), the clustering algorithm results were again evaluated by another algorithm specially developed for this purpose. The classification results are presented together with the accuracy metrics in *Figure 4-17*.

¹⁴ This correction file was provided in the context of exercise 1 within the framework of the lecture «Geo442 - Spectroscopy of the Earth System» at RSL / UZH, 2017.

4 RESULTS

4.1 Data preprocessing and quality assessment

4.1.1 Data preprocessing

Data preprocessing is illustrated exemplarily for the defined water masks at Irchel location, because here, spatial resolution has an evident impact. It is also recognisable how water surfaces in general can be distinct from land in the NIR range of the spectral signal. Furthermore, the position accuracy of the derived test field corner positions can be compared.

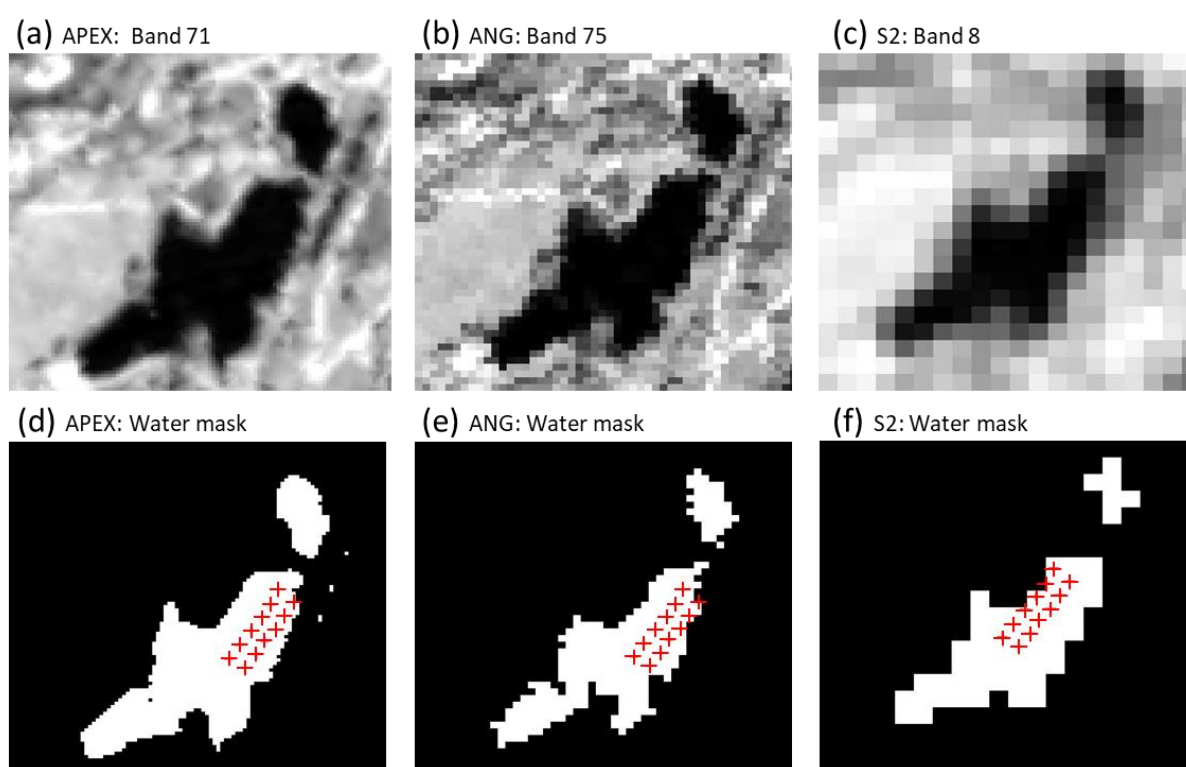


Figure 4-1: Binary water masks for the Irchel location with superimposed position vectors of the test fields.

4.1.2 Initial image quality assessment

Irchel test field corner position determination resulted in a geocoded image of high accuracy. Model residuals were acceptably small in the range of 0.032 – 0.174 and 0.009 – 0.360 for the X and Y coordinates, respectively. In the water masks (Figure 4-1), these corner positions are overlaid.

Geometry accuracy: Visual comparison of the PET test area pixels with the derived corner positions of each test field revealed a consistent shift vector of approximately 5 – 10 m at the Irchel location. Surprisingly, while this shift vector was of the same length for all data products, its position orientation differs between data products. As can be seen on the drone image (Figure 3-2 (a)), the PET areas were placed exactly in the middle of the water body. For the APEX Greifensee data, the GPS position accuracy is excellent with an estimated

uncertainty below 1 m. And for the AVIRIS-NG Hallwilersee data, a GPS position displacement vector of approximately 6 meters is present, comparable to the Irchel location. In the rescaled satellite subsets, the deviation is estimated a maximum of 1 - 2 pixels, resulting from image overlay.

Radiometric accuracy revealed no major issue in data quality, but one important fact regarding the imaging spectroscopy data became obvious: Due to the L2 preprocessing step for atmospheric correction, reflectance data contains fewer spectral bands, as summarised in *Table 4-1* below. Another important observation concerns the APEX radiance data of the Greifensee location: Since these data were acquired over a larger water body with an average depth of 20 m in the section of interest, a sensor and processing artefact along the flight line over the water surface was clearly visible in many bands, especially in the VIS region of the spectrum. Furthermore, these sensor artefacts were accentuated when image transformation was applied. No faulty bands were identified in the radiance image apart from this observation. The APEX reflectance image contains further artefacts following certain image lines in a horizontal east-west direction. For this reason, analysis was done using the radiance data only. Regarding the satellite data, no obvious quality limitation was observed, except for the uncertain geometric accuracy.

Table 4-1: Image spectroscopy data product image band assessment.

Data Product	Bands	Interpolated bands for L2 products	Omitted spectral ranges	Bad bands
L1 APEX Radiance	299	none	none	band 299 (noise) (artefacts)
L2 APEX Reflectance	284 (15 omitted)	73 – 77; 102 – 110; 120 – 128; 142 – 163; 190 – 227	377 - 398 nm; 2432 - 2515 nm	(artefacts)
L1 AVIRIS-NG Radiance	425 bands	none	none	none
L2 AVIRIS-NG Reflectance	372 bands (53 omitted)	1; 195 – 211; 281 – 315	381 nm; 1343 – 1433 nm 1747 – 1954 nm	none

4.1.3 Data transformation

MNF data transformation as a preparatory step for evaluations with reduced data volume did not show the expected result, and MNF bands were not further used for subsequent analysis – with one exception. The relevant variation at the test locations was only discernible in one single MNF band (band 4), as highlighted below, while spatial image (and artefact) patterns could be found in as many as the first 100 MNF bands. The sensor artefacts along the scan line (from south-east to north-west direction) were strongly accentuated in the first 10 bands. The resulting first bands containing the most relevant image variability are presented here.

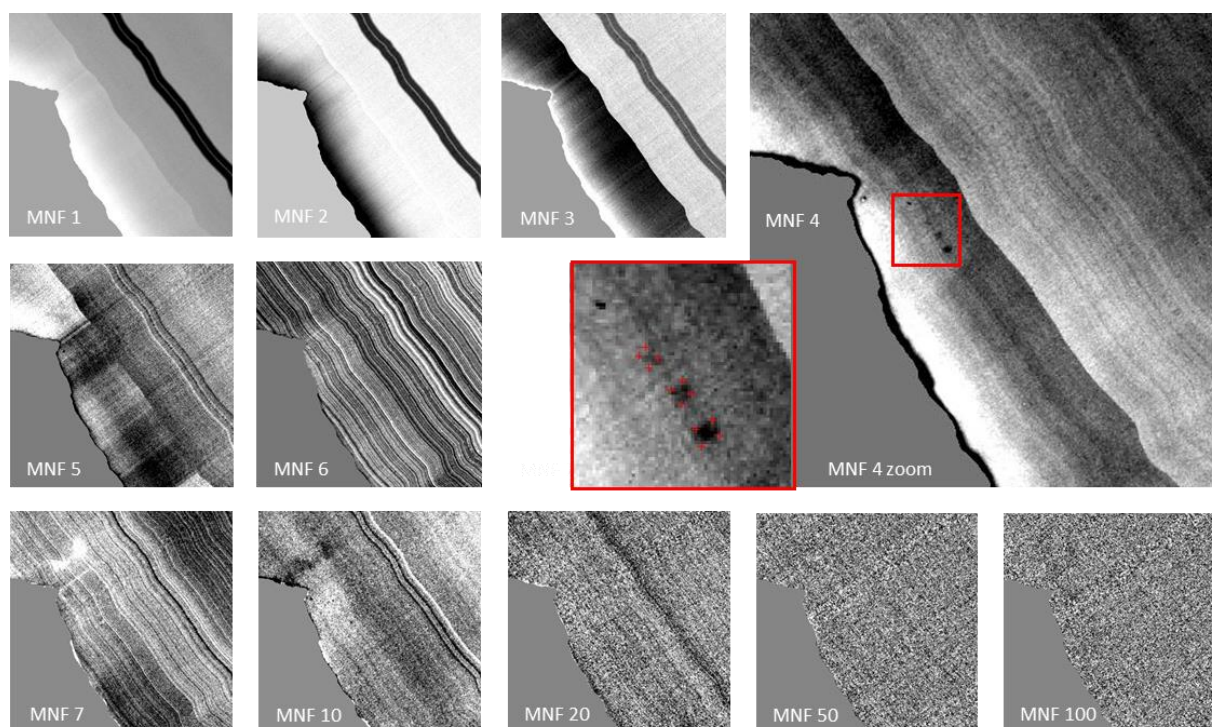


Figure 4-2: MNF bands of the masked APEX radiance subset. The red symbols highlight the PET test area corner positions.

4.2 Basic image evaluation

4.2.1 Spectral and spatial profiles

In *Figure 4-3* reflectance spectra of all sensors are displayed with the goal of providing a first impression of the different sensor characteristics as well as reflectance value ranges. Not all three mean PET surface abundance values are plotted but only the densest one for easier comparison with the water reflectance spectra of the same sensor. Typically, the water surfaces containing PET show slightly higher reflectance values than the surrounding water surface over the entire spectrum. However, this observation does not hold true for the satellite spectra in all bands. The most obvious differences between the sensor data are observed at the edges of the covered spectral range.

For the representation of the **satellite band values**, the individual band values are visualized over the wavelength ranges to emphasize the corresponding different width of these bands. This was also done to highlight that multispectral satellite images usually do not contain continuous spectral values over the whole range. In the plot, the thin lines between the band values constitute only interpolation lines and are not to be confounded with the band value ranges (thick horizontal lines).

In *Figure 4-4*, only image spectroscopy spectra are plotted, both reflectance and radiance data, and this time, all PET test areas are visualized. Particularly in the AVIRIS-NG data, a **gradient** between water and highest plastic content is easily recognizable (for the APEX data, values overlap in this visualisation but also become distinguishable if the representation is sufficiently enlarged). In the radiance plots, the prominent atmospheric water vapor absorption bands around 940, 1130, 1400, and 1850 nm (Richter and Schläpfer, 2016) are recognisable due to very low values.

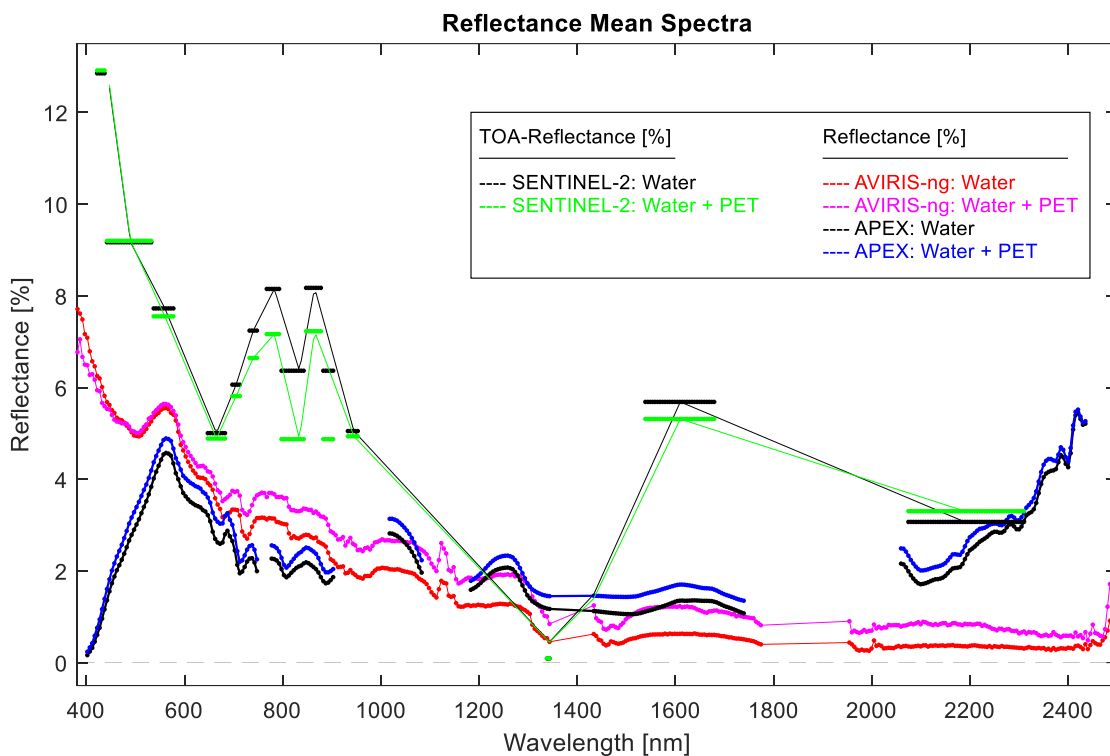


Figure 4-3: Reflectance signals of the APEX, AVIRIS-NG, and Sentinel-2 sensors.

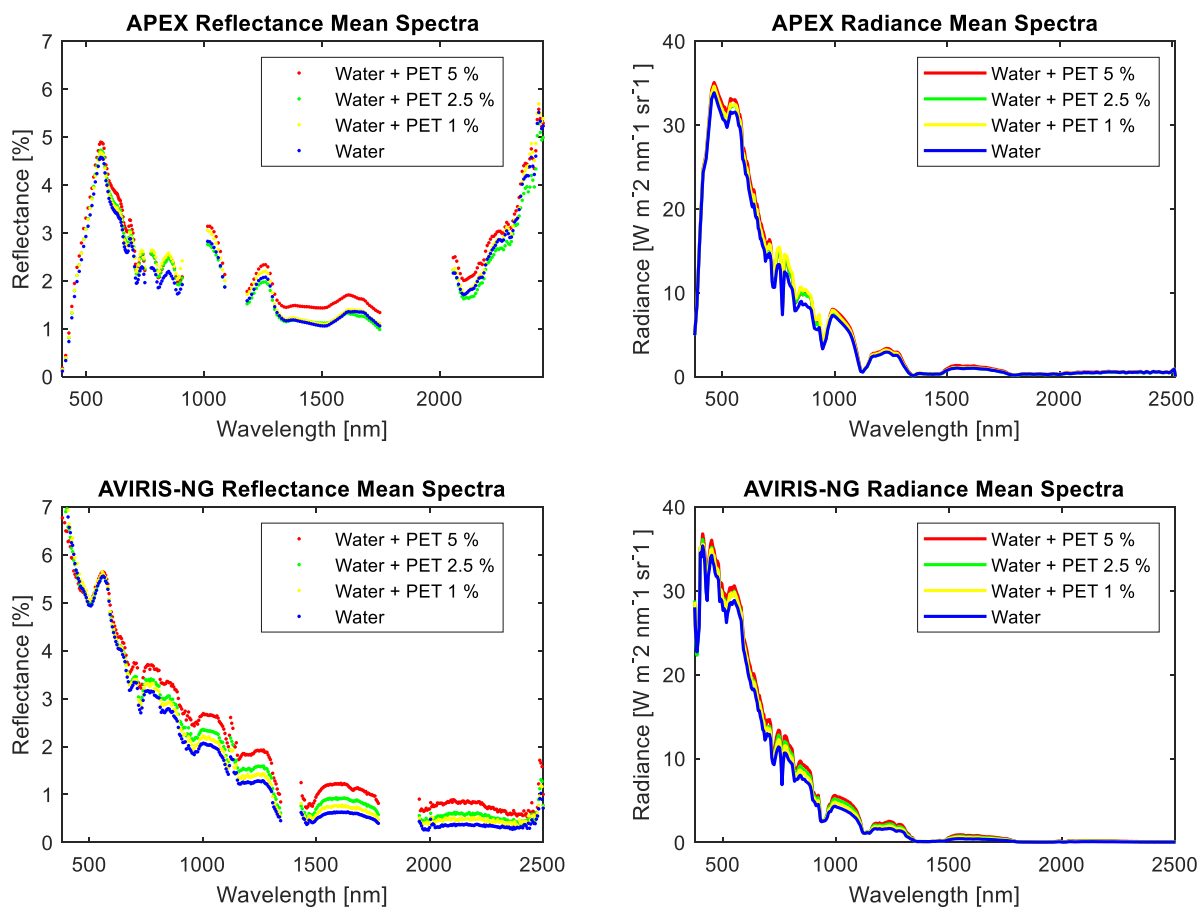


Figure 4-4: Spectral profiles of water and PET test area reflectances as well as radiances, both from the APEX and AVIRIS-NG sensors.

Figure 4-5 shows the enhanced image subset with the defined transect line (white line) through the brighter test areas A, B and C. The corresponding band values of the pixels under this transect line are visualized in the **spatial profiles** plot. These band value plots contain the spatial profiles of each image band. The chosen profile colours correspond to the displayed bands (RGB). For all three test fields, approximated dashed lines indicate the corresponding increase in pixel value.

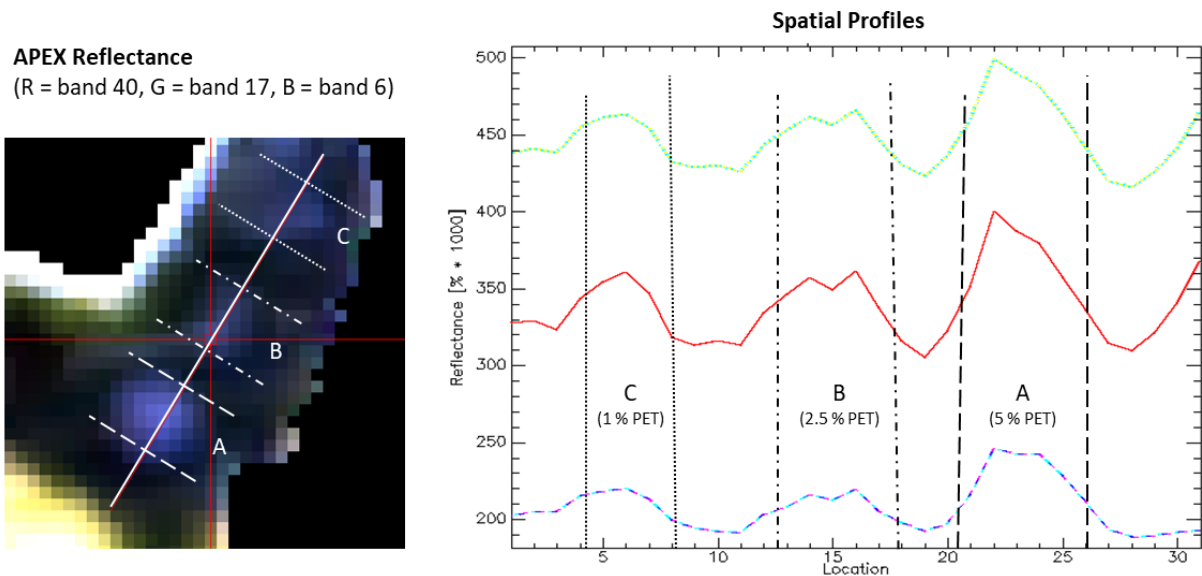


Figure 4-5: Spatial profile of the APEX reflectance RGB bands (ENVI visualizations with overlaid lines indicating the PET test areas). Location values on the x axis refer to pixel numbers along the defined profile line.

4.2.2 Image enhancement approaches

Figure 4-6 contains for each of the sensor images two masked reflectance visualizations where histogram stretching was applied on selected bands. The APEX band 92 (at 849 nm in the NIR) showed the largest spectral difference (a). Colour infrared images (CIR) also highlight spectral characteristics in the NIR (b, c). However, this common visualization option focusses on vegetation information and is not particularly suited for water surfaces. Still, the reddish pond margins indicate higher vegetation, which largely corresponds with reed growth at these positions. The histogram stretching approaches (c – e) simply expand the original band brightness values to make use of the whole dynamic display ranges, using various mathematical equations. Thus, these methods are only to apply for visualisation enhancement, as was the purpose in this methods part.

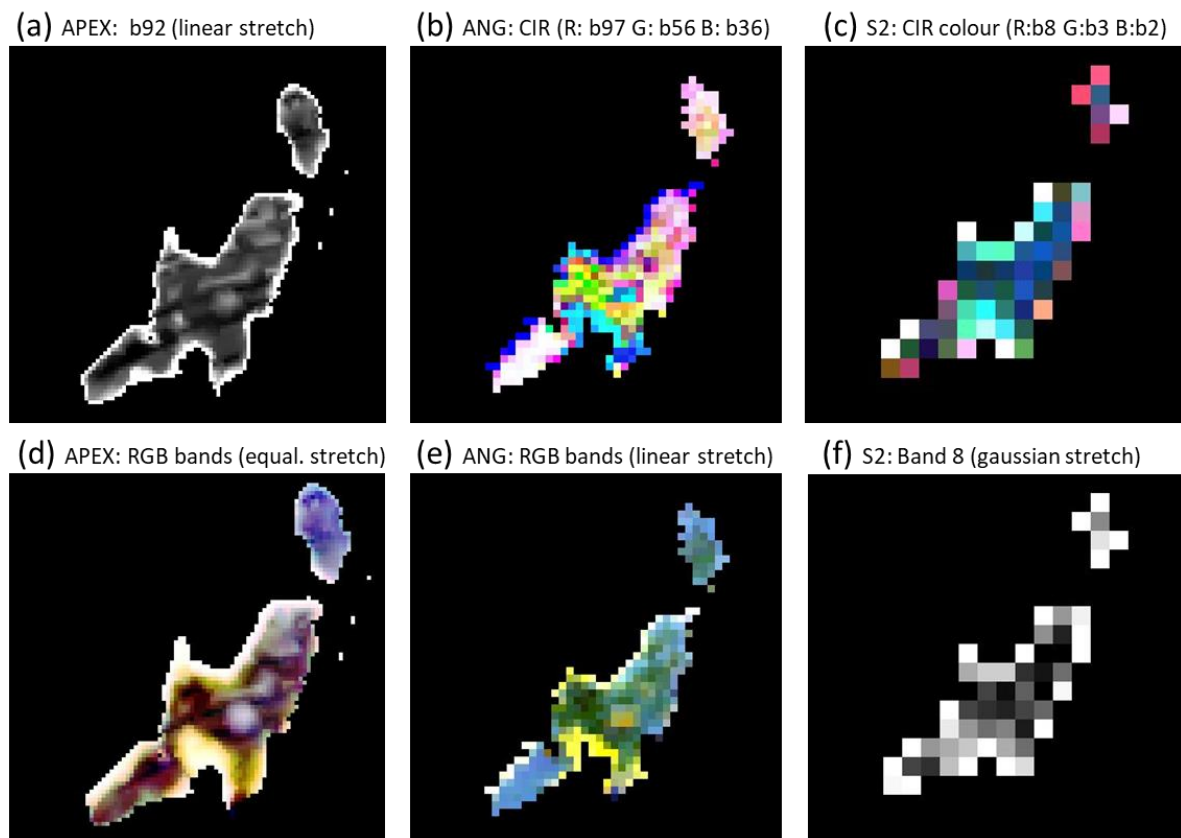


Figure 4-6: Enhancement methods: Histogram stretching for masked single band, true colour and false colour images.

4.3 Discrimination approaches

4.3.1 Clustering

In *Figure 4-7*, only selected results of the k-means algorithm using all image bands (a) – (c), and using only selected image bands around the known 1730 nm plastic absorption feature (d) – (f), are displayed. Choosing 7 cluster classes led to the best results with the selected bands, as can be seen in both the classified image as in the accuracy metrics. All classified images are overlaid with the test field corner positions for easier identification. The accuracy assessment results, calculated based on the manually defined reference file, are plotted for all (12) cluster class numbers that were evaluated.

For any thematic map, quality considerations should contain information about the nature of the accuracy assessment problem, the classes of interest and of course about the result accuracy and sources of error (Jensen, 2016). Since the problem is unusual for this method, the results were not thematically classified afterwards. Only the most dominant cluster covering the PET areas was interpreted as the class of interest in each result image. This was always the last cluster class with the highest cluster number, thus covering the least pixels. Since PET abundance differences might result in more than one classes – as it is the case in *Figure 4-7 (f)* – an accuracy assessment based on only one class of interest gets biased considering the abundance difference that can be seen in this result.

However, it was the main goal of this unsupervised clustering approach to find a general answer (and possibly a trend) to whether there are statistical differences in the data that can be found without any given image parameter relating to plastic targets. It was not primarily focused on PET abundance differences, although in the accuracy metrics, the three PET test areas were evaluated separately for producer accuracy, resulting in an expected increase in producer accuracy with higher PET abundance. At this location, the ground reference pixels perfectly fit the visible brighter target patches in the data (estimated location uncertainty < 1 m).

Explanatory notes to the accuracy metrics: Calculation of the **producer accuracies** is orientated at the reference class definitions. The count of all correctly classified pixels in the class are divided by the total count of pixels in the same reference class, thus its errors relate to omitted pixels (omission errors) that should have been classified in the same class but were not. The calculation of the **user accuracies** however is orientated at the classification results. It is usually done for each of the classes as well, by dividing all correctly classified pixels in the class by the count of all classified pixels in this class. Errors relate to pixels that were classified in a class but should not have been (commission error). Therefore, this accuracy measure yields the relevant information on how well a classified class matches with the reality (Jensen, 2016).

The **overall accuracy** might seem rather misleading, since it is calculated by dividing all correctly classified pixels by the total pixel number of the classified image. Typically, this metric is very high for images where the relevant pixels only cover a small part of the image, as it is the case for the present water subset image. Most of the image pixels are water pixels and therefore were classified correctly. And consequently, the mean accuracy also shows high values, because it is calculated by averaging the mean user accuracies and the overall accuracy (Congalton and Green, 2009).

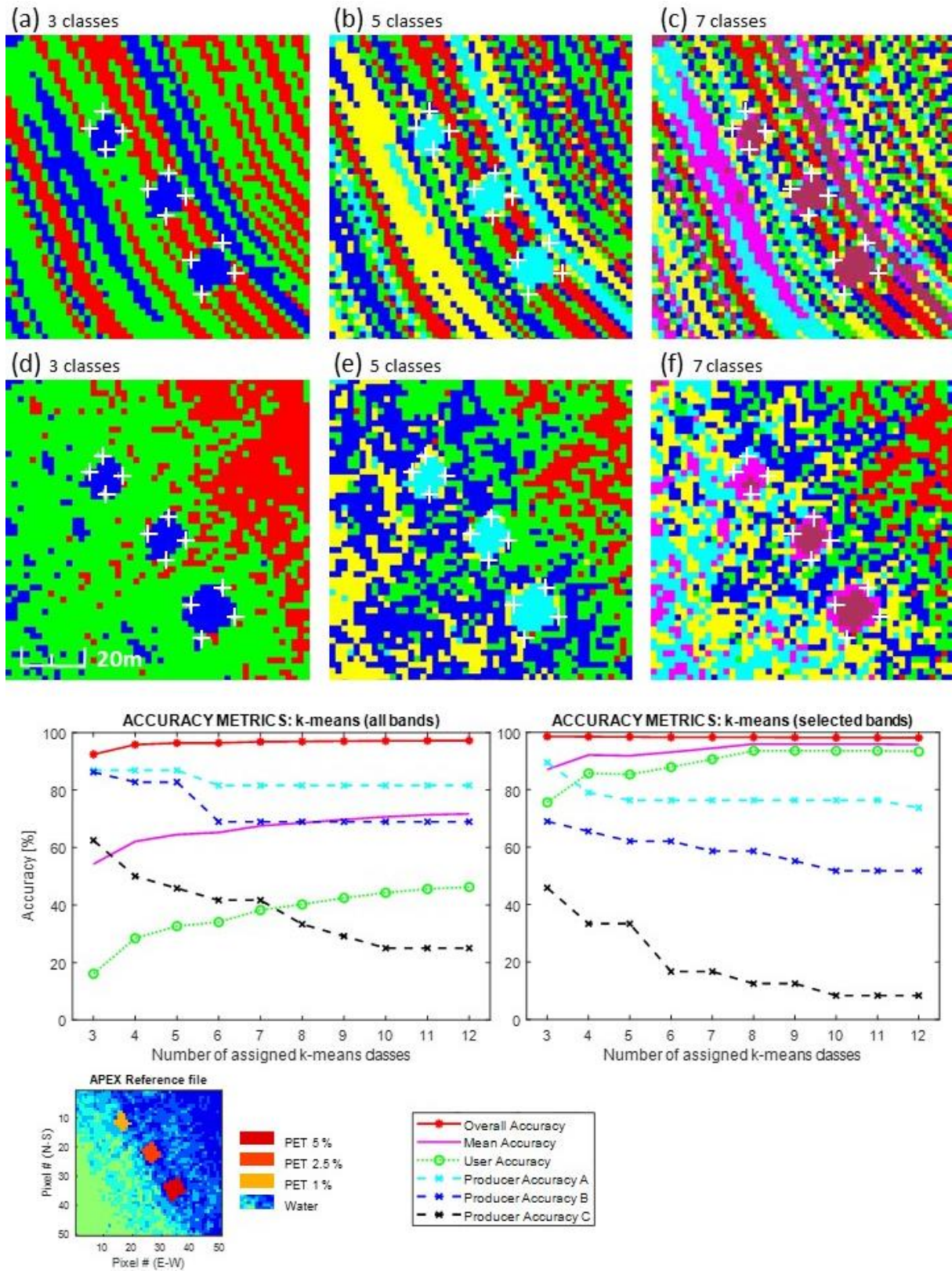


Figure 4-7: K-means results of the APEX radiance subset data, using all spectral bands (a) - (c) and using only selected bands (d) - (f) for evaluation. The accuracy metrics are based on the reference file definitions.

4.3.2 Band ratioing and indexing

The indices using three bands of a known absorption feature each were applied on both APEX and AVIRIS-NG radiance data. The greyscale result images (*Figure 4-8: a, d, g and Figure 4-9: a, d*) were histogram stretched for better visual judgment, and the PET areas are greatly enlarged and marked with plus signs (*Figure 4-8: c, f, i, and Figure 4-9: c, f*). While the grey scale results already allow a good estimation of their relevance, the added coloured value ranges confirm their heterogeneity (*Figure 4-8: b, e, h, i*). Although the PET Index results are the only ones that show a clear distinction of the plastic-containing pixels and even the PET abundances, it is to be noted that the density slicing (range values as defined in *Table 3-2*) was carried out with the best "matching" range values and is therefore only tuned to the current image subsets.

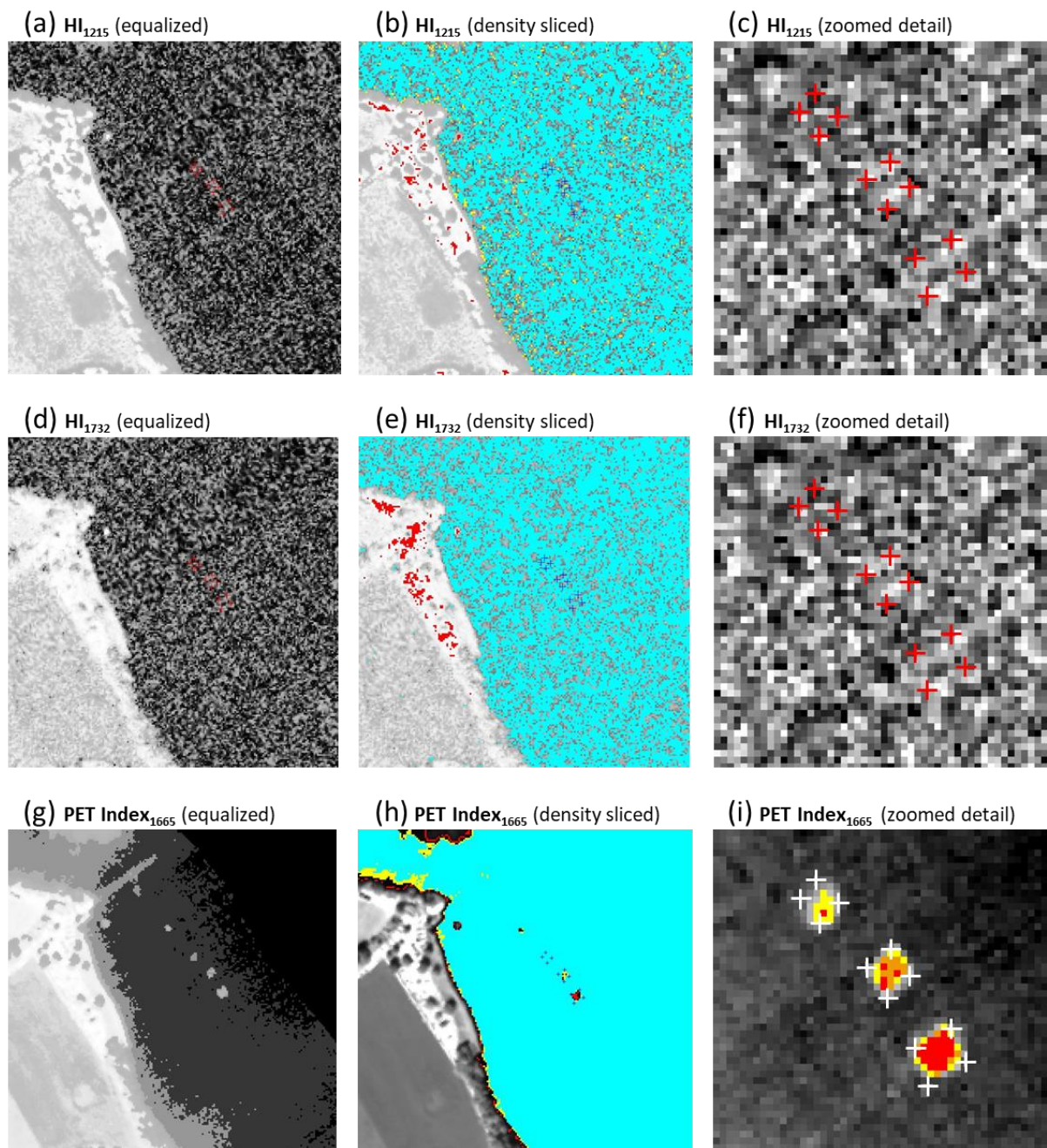


Figure 4-8: Index results for APEX radiance data.

The coloured results of the AVIRIS-NG data were density sliced in a similar way as for the APEX results, with additionally applying the green colour for the land zone. It is to be noted that at this location (*presented in Section 3.4*), only 2 of the PET test fields were deployed.

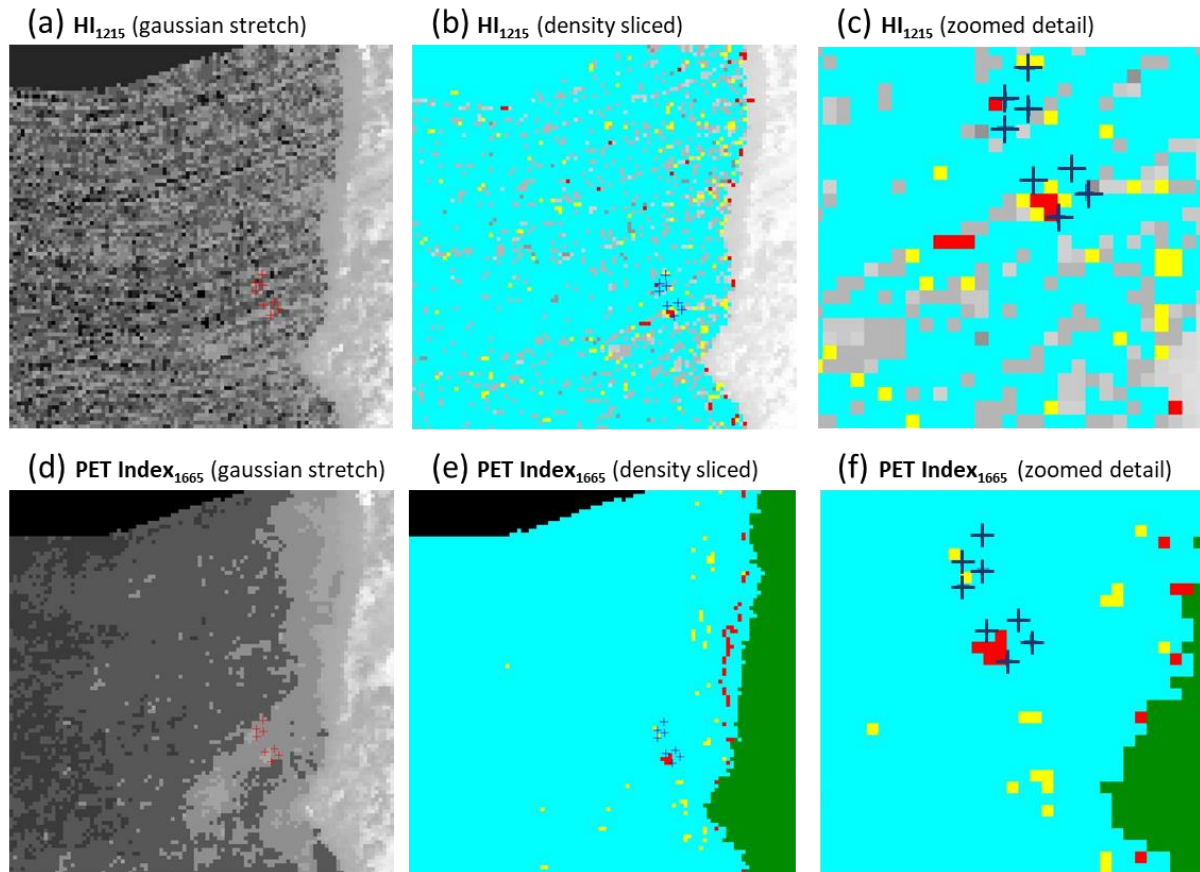


Figure 4-9: Index results for AVIRIS-NG radiance data (Hallwilersee location with only 2 PET test areas).

4.3.3 Supervised Classification

The results from the Minimum Distance classifications are displayed in *Figure 4-10* where only the water pixels were to distinguish from the plastic containing test fields, and in *Figure 4-11* where scaling results were in the focus additionally. All differences between these two figures stem from the disparate reference classes used as input variables for the algorithm.

Colouring for the classified images was chosen again using red, orange, and yellow for the decreasing plastic abundancies. The reference class pixels are depicted on a black background, and the defined ground reference pixels (showing slightly darker colours as the corresponding reference classes) are both plotted based on the evaluated layer stack data.

The accuracy metrics were calculated as described in *Section 4.3.1*. Bar plot diagrams were chosen for display, because the individual evaluations per run do not follow a specific scaling (as was the case for the k-means evaluations) but are to serve only as a basis for comparison. It seems appropriate to focus on the user's accuracy values, displayed as bright green bars, rather than the potentially misleading overall or mean accuracies.

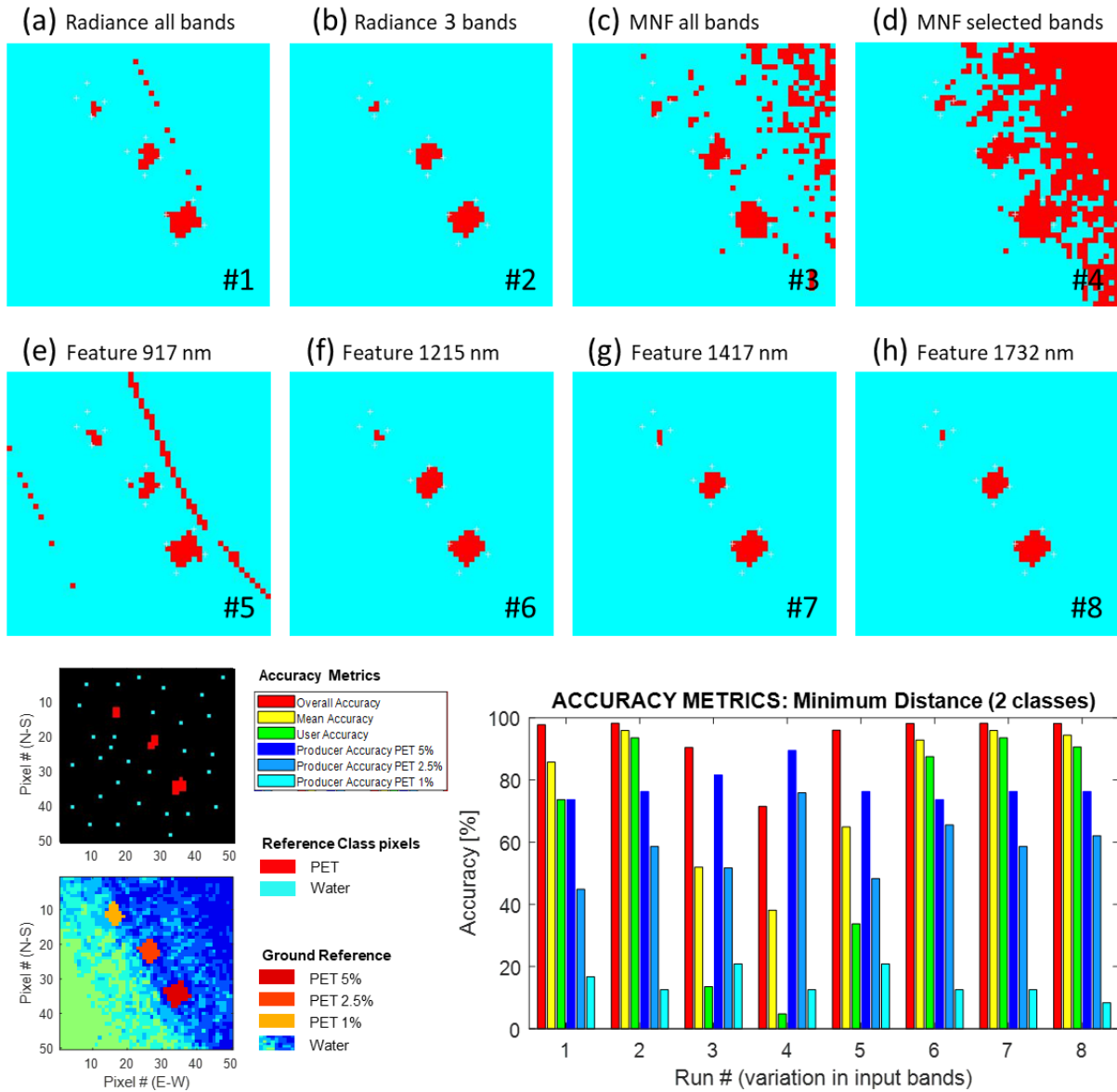


Figure 4-10: Results of supervised classification using only 2 reference classes: Water and water + PET mixed, as indicated in the Reference Class legend.

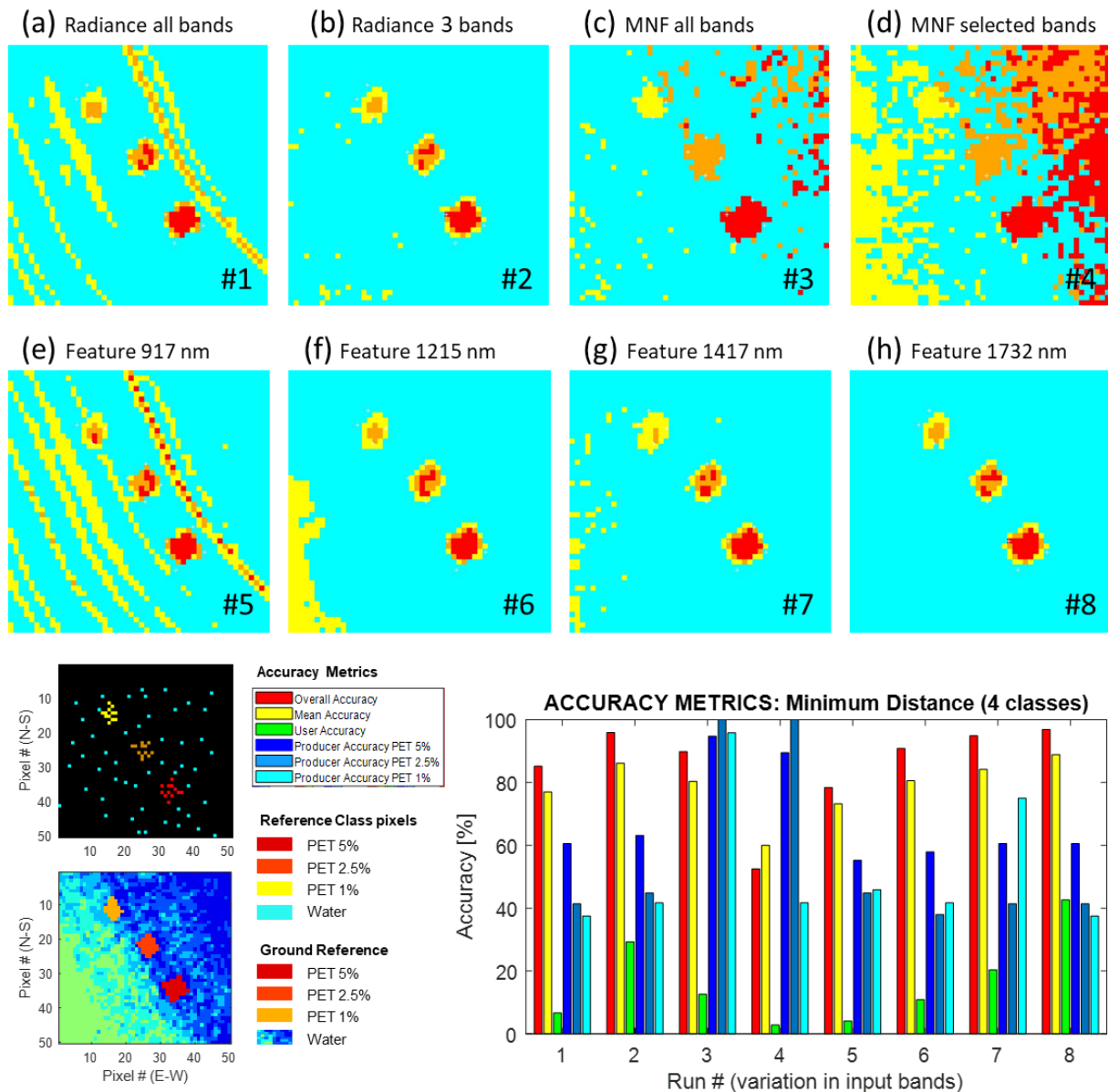


Figure 4-11: Results of supervised classification using 4 reference classes, as indicated in the Reference Class legend.

4.4 Plastic identification

4.4.1 Spectral Angle Mapper

Result images (a) – (d) of *Figure 4-12* on the next page show the classification based on only two reference classes with the red pixels being classified as PET containing water and blue pixels referring to water only. The result images (e) – (h) show the classification results based on all PET abundance classes. For comparison, the GPS corner positions of the test areas are indicated. Black pixels refer to unclassified areas where the difference between reference spectra and pixel spectra was larger than the defined threshold. The bar diagrams containing the accuracy metrics show gaps for the medium PET abundancies due to the lack of this test area at location #3.

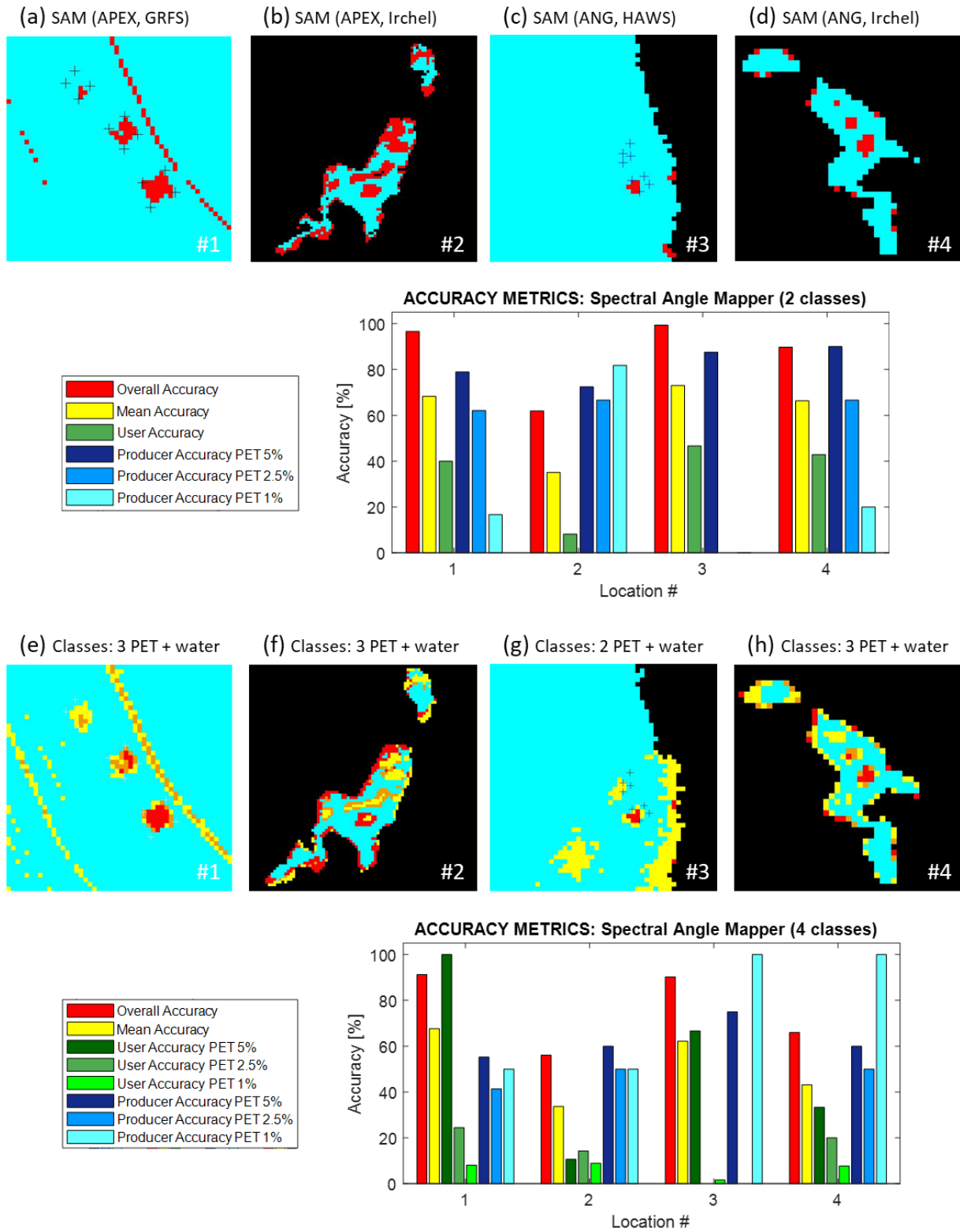


Figure 4-12: SAM results for all locations and both AVIRIS-NG and APEX data.

4.4.2 Continuum Removal

In the Continuum Removal result images, bright values represent higher absorption feature areas, therefore, the pixels should be bright at all plastic locations.

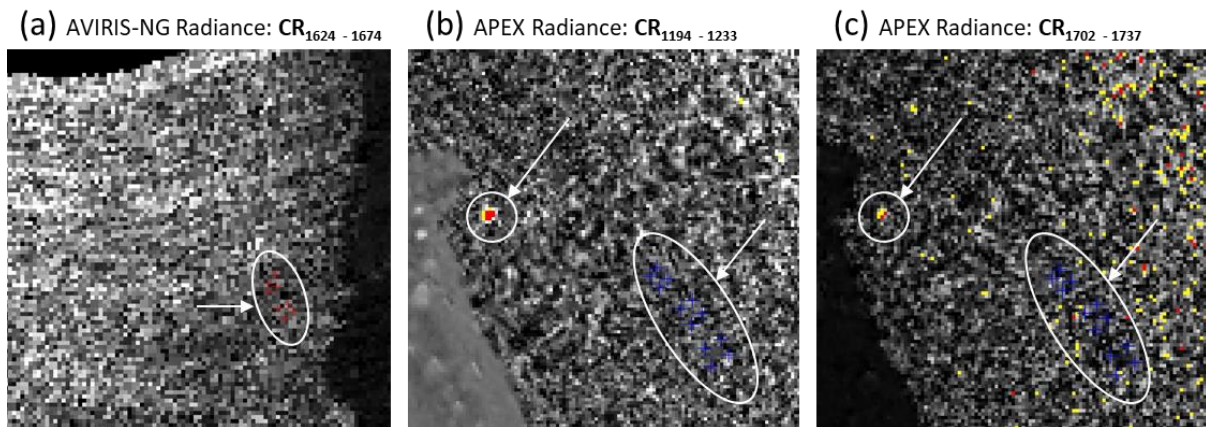


Figure 4-13: Continuum Removal results for the Hallwilersee location (a) and the Greifensee location (b, c).

For the Hallwilersee location, the method was applied on both the radiance and reflectance data and for the 1215 as well as for the 1665 absorption feature. Here, only one of the result images is shown, since all must be regarded as equally disappointing: In the greyscale result image with highlighted PET locations (Figure 4-13 (a)), the CR radiance differences are somewhat more pronounced compared to reflectance data evaluation (not shown), but in all result images, higher (brighter) CR values are scattered all over the water surface area. The indicated test fields show even lower values than those areas on the lake that were more exposed to the wind. All these results are far away from a clear distinction of materials.

For the Greifensee location, the results were density sliced to draw attention to one particular finding: While again there is no clear distinction for the PET areas, the indicated image position with highest CR values highlighted in red - especially in the 1215 absorption feature result (Figure 4-13 (b)) - indicates the plastic raft in the image. Besides, this plastic raft is documented in the foreground of the early morning picture presented in Figure 2-1 (c). The result of the 1665 PET absorption region again is not presented here since it yields the same useless results for the test areas while not indicating the raft of another plastic type.

4.4.3 Spectral Mixture Analysis

Applied methods based on spectral mixture analysis were Mixture Tuned Matched Filtering (MTMF) and the comparable Matched Filtering (MF) algorithm, the results of which are documented here (Figure 4-14). Results of the MF method consist in a series of greyscale images for each endmember. Here, only the image for the PET endmember is presented, although the result of the water endmember was slightly different. In (a) and (b), this greyscale image provides a first impression of relative matching degree to the reference spectrum. However, the targeted material is only present in the brightest pixels while medium values (medium grey colour) represent background material (ENVI, 2002). For this purpose, only values > 0.002 were selected for histogram stretching (c) showing only pixels containing the targeted plastic material. The few bright pixels in the image all are located within the campground area.

Since the results here are rather unexpected, the infeasibility image from the MTMF approach has been added (d). This is methodically not quite correct, but it may be helpful as a hint for interpretation.

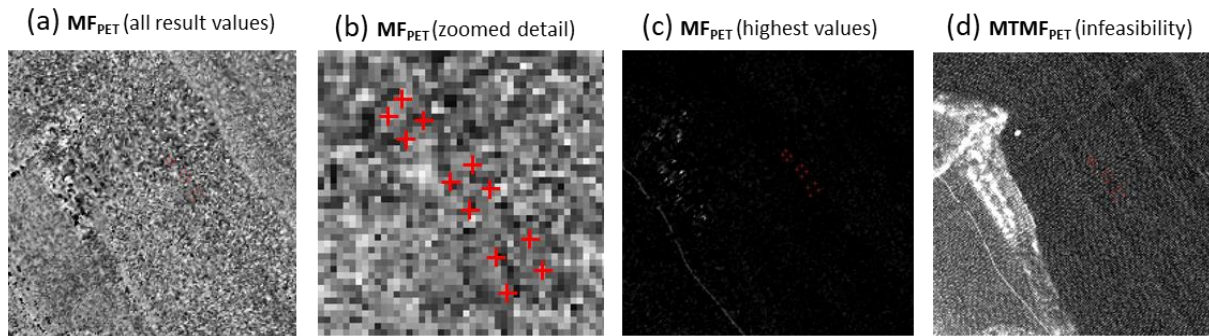


Figure 4-14: Matched Filtering results (APEX, Greifensee) with indicated test field locations (red).

4.5 Spectroscopic models

4.5.1 Spectral mixing model

The linear spectral mixing model (Figure 4-15) is based on radiance spectra and illustrates the spectral characteristics of mixtures from dry PET endmember spectra and mean water spectra in steps of 1%. The highest spectral curve represents the radiance spectrum of PET, while the lowest curve represents the spectral signal from water, which in this case is representative for the smooth water surface of the Greifensee location.

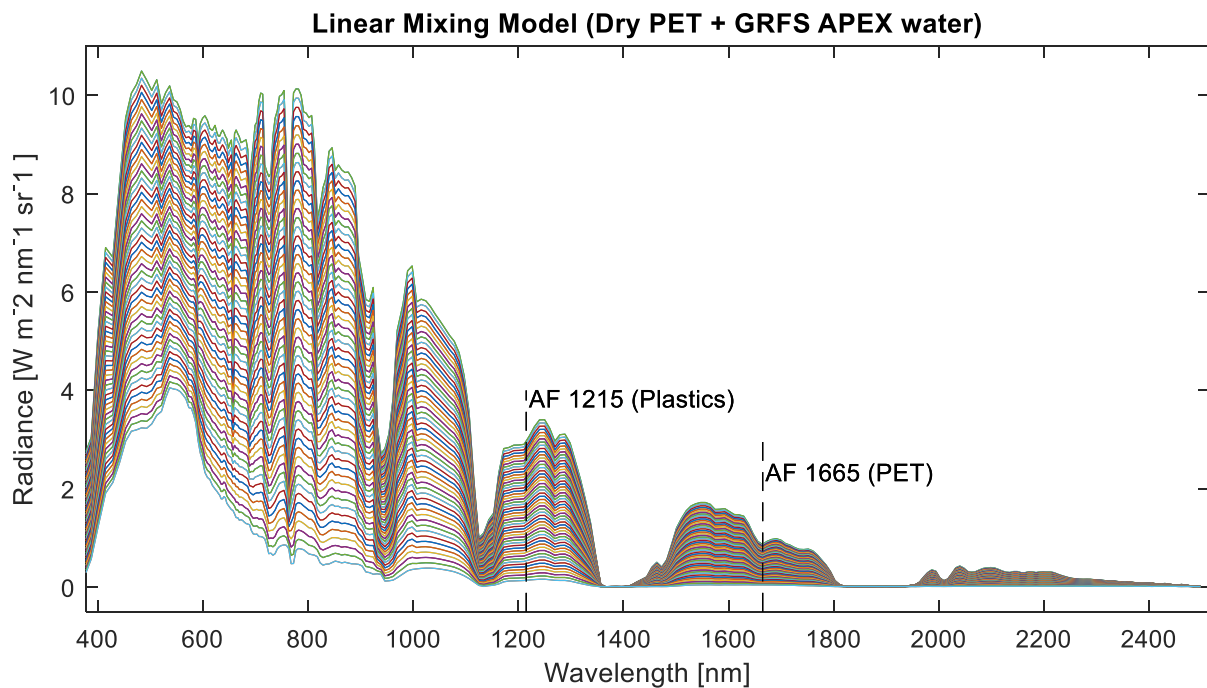


Figure 4-15: Spectral mixing model with APEX water (Greifensee) and ASD-PET spectra. The precise location of the most promising absorption features are indicated.

Although the small differences between the two extremes cannot be seen in detail in the plot, the PET spectrum shows not only generally higher values, but also more pronounced features than the curve shape of the water, which is mainly due to atmospheric absorption bands (at 930, 1150, 1400, 1850 nm).

This mixing model approach offers the possibility to finally verify the estimated plastic abundancies of the three test fields. *Figure 4-16 (b)* shows the best match determined between the model's abundance fractions and the mean image spectra from the reference fields.

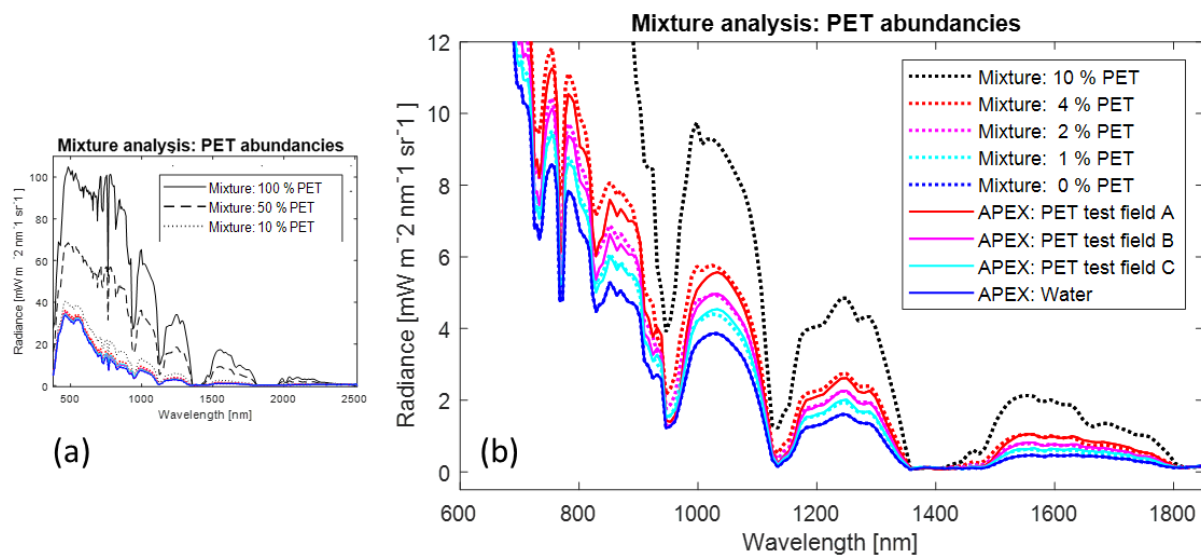


Figure 4-16: Approximation of PET abundancies in the 3 test fields based on mixture analysis. In (a) the whole spectral range is plotted with high PET abundancies for comparison while (b) highlights a zoomed range of best matching spectra from the linear mixing model with mean image spectra of the test fields.

4.5.2 Spatial scaling

The same result colouring and accuracy visualization as for the clustering results (*in Section 4.3.1*) are applied also to the pixel size scaling experiment, as presented in *Figure 4-17*. Here, an additional linear trendline highlights the (green) user accuracy decrease with larger pixel size in the accuracy metrics diagram for all 10 conducted and evaluated variants of the pixel size (again, only a selection of the result images is displayed).

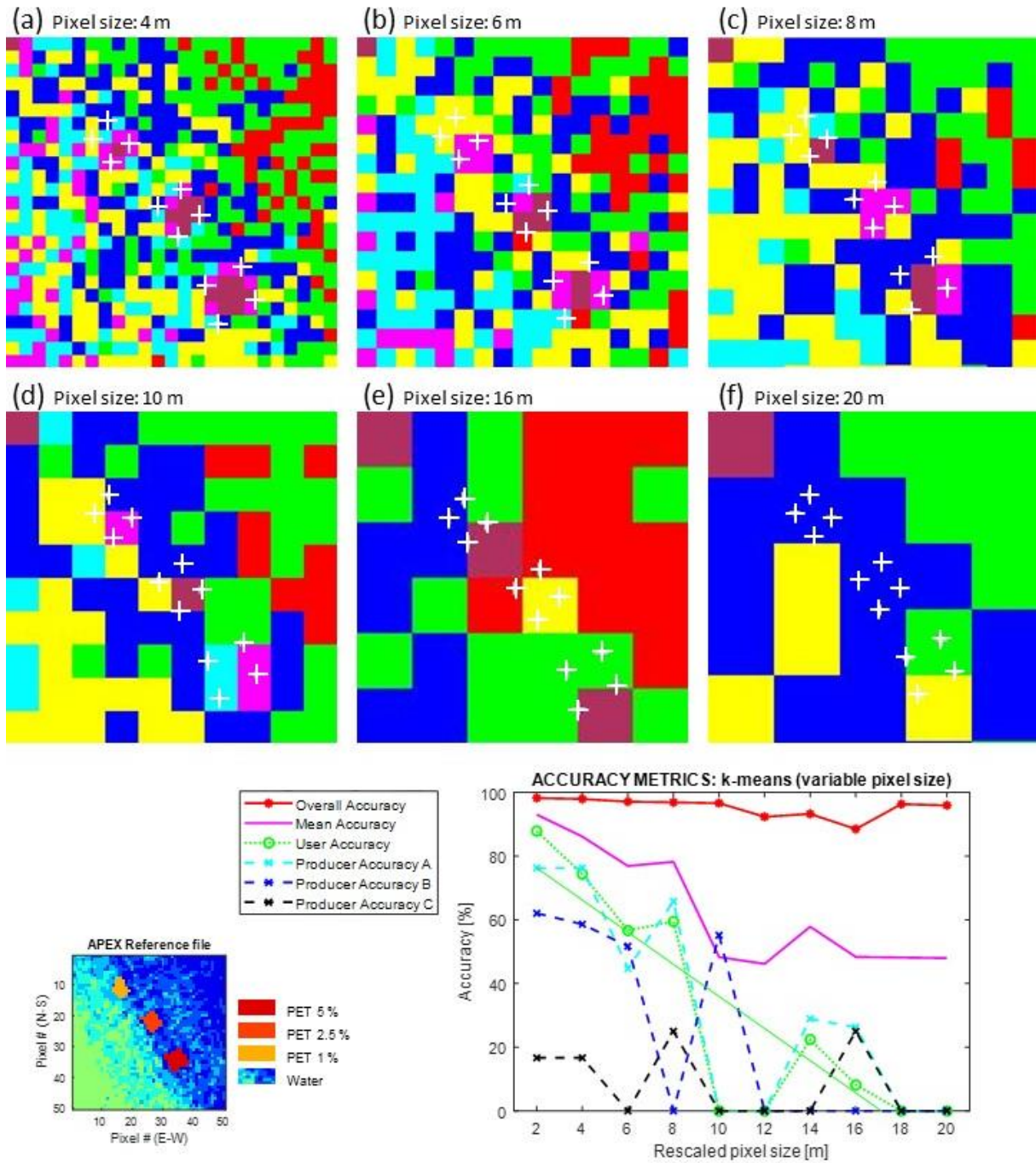


Figure 4-17: K-means results of spatially upscaled APEX data, using the same selected spectral bands for evaluation as in the step above (Figure 4-7 (d) – (f)).

5 DISCUSSION

This section discusses the research and data exploration results as presented in chapter 4. While its structure is oriented on the methods subsections, selected results are summarized and discussed together where comparable approaches are concerned. The last subsection additionally focuses on more theoretical considerations in relation to the whole complex of factors influencing optical detectability of floating ocean waste, thus discussing the obtained outcomes with respect to the suitability of the experimental setting and its restrictions with regard to the more complex situation in reality.

5.1 Data preprocessing and quality assessment

Geometry accuracy of the images from the Irchel location, as compared with the derived test field corner positions, is regarded as helpful for identifying the exact test area positions on the lakes where no drone data were acquired because drone flights at the chosen locations were banned for environmental reasons. The systematic discrepancy in geometric accuracy of about 10 m for all datasets of the Irchel location is of no further consequence for the data analysis here. Geometry accuracy is regarded an issue only for the satellite data. Therefore, evaluation of the satellite data was only possible to a very limited extent, due to its geometric uncertainty of about one pixel - i.e. the area in which an entire PET test field would be contained. This uncertainty of +/- 1 satellite pixel (10 m) could be estimated adequately thanks to the small water area of the Irchel pond.

Since the **MNF data transformation** did not yield the expected advantages, the transformed data was not applied as expected (e.g. for MTMF). However, evaluating MNF transformed data possibly works better for homogenous ocean water areas. It seems advisable to reconsider this approach, as its advantages of noise reduction and reduced data volume are likely to be of great use.

5.2 Basic image evaluation

First indications based on **spectral profiles** suggest a higher radiometric accuracy of the AVIRIS-NG sensor data, compared to the APEX data. This can be seen in a higher distinction of the spectra with varying PET abundance in both the reflectance and the radiance plots, as well as in a more detailed curve characteristic, which is due to the sensor's higher spectral resolution. It is also apparent that the two imaging spectroscopy sensors show great differences at both ends of their spectral range. However, this observation is unlikely to have any effect on plastic detection, as the spectral ranges in focus do not affect these wavelengths. And as was to be expected due to the band configuration of the Sentinel-2 satellite, the reflectance curve of this sensor clearly shows the big difference between multispectral and hyperspectral sensors. The generally higher reflectance values of the satellite data are related to atmospheric scattering that makes up a share of the spectral signal sensed at the top of atmosphere (TOA).

Sensor and data product selection: It is likely that satellite data are not suitable for further analysis. As far as imaging spectroscopy sensors are concerned, these initial data analyses show that the evaluation of radiance products offers the most promising basis, as it is also recommended in respective papers (Garaba and Dierssen, 2018; Goddijn-Murphy et al., 2018). The basic radiometric accuracy assessment revealed the unwanted consequences of the atmospheric preprocessing step generally applied to L2 data. While in remote sensing

applications this is the data product of choice for the vast majority of problems, this common procedure is not appropriate for water surface analysis, basically for atmospheric correction algorithms reasons. Therefore, mostly L1 radiance data is considered for all further analytical steps in the subsequent method subsections.

Essentially, the data situation looks promising, since already in basic image enhancement approaches - as well as most clearly in the spatial profile - not only the three test areas were recognizable, but even a certain gradation between these test areas. Despite this, it is important to point out the very low reflectance values of a few percent only, especially in the NIR. These low values are typical for water leaving reflectance since water nearly absorbs all irradiance (Odermatt, 2011). Such low values generally lead to less favourable SNR values, which requires high radiometric performance of a sensor.

5.3 Discrimination approaches

Quite some rather unexpected findings resulted from the application of common image analysis and classification techniques. Overall, the PET test areas were identified surprisingly well, but the question remains as to what these achievements are attributable to. Are they only differences in brightness – or can they actually be attributed to specific material properties?

5.3.1 Clustering

The striped artefact patterns, detected in the previous subsection already, highly influence the result in an undesired way, but the focus lies on the small plastic abundance in certain water pixels. First impressions of these early results (*Figure 4-7*) may look quite striking. It is important, however, to point out that the small image subset covers an area of 100 m x 100 m only, with rather homogenous water depth, quality, and surface structure. Therefore, the same k-means algorithm was applied again for 7 clusters and run over 3 iterations on the same dataset, but this time with a larger (masked) subset area.

The optimistic intermediate result is highly relativized when clustering the larger area of the subset, as documented in *Figure 5-1*: Here, it can be clearly seen that especially in a shallow water zone near the shore, the main differences in the spectral vectors are mostly bathymetry related (a). The resulting k-means clusters using all spectral bands show again the stripe pattern in the direction of flight (b) which stems from the detected sensor artefact inherent in the data (*visualized in Figure 3-3 (a) and (c)*). This is much more obvious in the VNIR range of the spectrum than around 1700 nm (the region of the selected bands). When selecting the same 3 spectral bands for classification, the zoomed result (c) shows again a specific cluster assigned only to the pixels containing floating plastic targets.

So, here it becomes obvious that the algorithm's accuracy highly depends on the chosen image subset extent, and clustering is ambiguous for the plastic targets. Logically, as the resulting clusters highlight the main image data content, they cannot be expected to identify any rare variability of plastic signals in mixed pixels.

Furthermore, the accuracy metrics must be interpreted with care, since it rather gives an idea about statistical differences in the imaging spectroscopy data than describing the mapping accuracies with undistorted numbers. This applies in particular to the boundary areas of the plastic areas, where lower abundance classes may be classified more correctly than was possible in the manually defined reference fields. Therefore, the result images possibly provide a more precise impression.

After all, since the selected bands relate to a known plastic absorption feature, the positive results in this methods subsection give reason to come back to these interim results and to analyse this absorption feature in subsequent method parts with a more specialised approach.

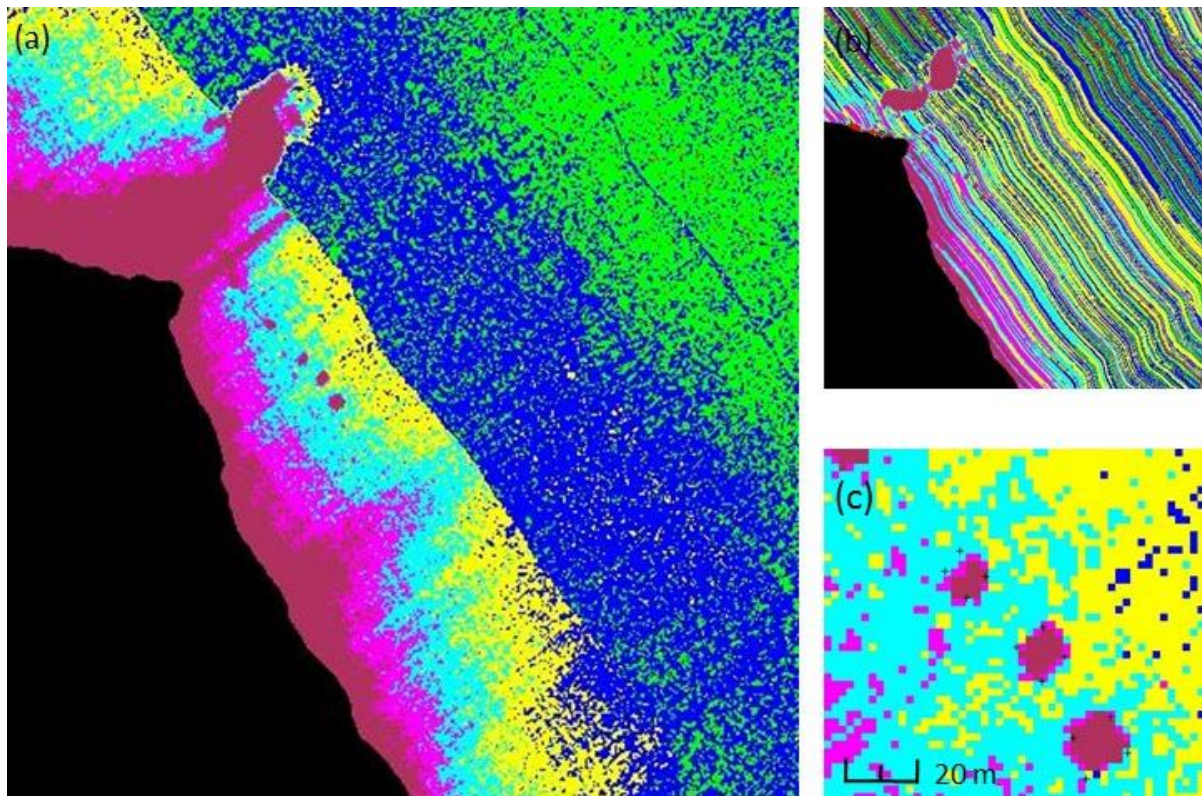


Figure 5-1: K-means results using the whole spatial subset area for evaluation. For (a) and its zoomed detail (c), only selected bands were used as input, while (b) shows the result of the same method applied on all spectral bands.

5.3.2 Band ratioing and indexing

When comparing the index results, it is noticeable that the index variability for HI_{1215} and HI_{1732} is very large in the water range and that no indications of the PET test areas are discernible in the respective detail sections (Figure 4-8 (c) and (f)). This impression is also confirmed by the colouring for selected index value ranges (Figure 4-8 (b) and (e)), where the water surface shows very heterogeneous values. At least the water area can be clearly distinguished from the land area. In addition, high concentrations of plastic are now visible through the red colouring. This concerns the area of the campsite, where some of the values highlighted in red seem to refer to tents containing plastic surface materials. However, these results are not unambiguous. But the more important observation is: For the few pixels at the plastic raft location, the indices show acceptable results.

This is also the case for the PET Index results which combine band value differences (due to curve characteristics) with the overall higher band values in plastic containing signals. However, it must be admitted that the density sliced index image colouring is ambiguous as well. This is most evident for the scaling effect (Figure 4-8 (i)) where the chosen index ranges for denser PET areas (red) and medium PET abundance overlap (Table 3-2). And the smoke clouds at the upper image section are misclassified, an effect that did not occur as strongly with the other indices.

As for the AVIRIS-NG index results (*Figure 4-9*), the established Hydrocarbon Index calculations (c) resulted in a better result than with the APEX data, but the PET Index results were less distinct. This may partly be due to the general conditions at this third location, where only two of the three PET test fields were deployed and the bottles were mostly wet or even submerged. On the other hand, all these indices did not provide unambiguous results. This must probably be explained mainly by the fact that the PET abundances of all test areas are barely high enough for the spectral curves of these mixed pixels to show the required feature. This must be assumed all the more since the indices are said to be applicable both for reflectance data and - as applied here - for radiance data (Kühn et al., 2004). Still, reports on detection limits are scarce and vague due to limited studies. The closest estimate found in the literature relates to the application of the HI₁₇₃₂ for oil spill detection on coasts with variations between 2.5 and 25% (Asadzadeh and Souza Filho, 2017).

In order to verify this assumption, reference is made to the **spectral curve sections** shown in *Figure 5-5* (*Section 5.4.2*), where the bands for the index calculations are specially marked by datatips. The different performance of the HI₁₂₁₅ can thus be attributed to sensor differences: While the highest spectral resolution of the AVIRIS-NG sensor reveals a corresponding small absorption feature (a), this is missing in the APEX spectrum (c). However, it is distinct for the high plastic abundance in the raft signal (e). The absorption feature at 1665 nm, in contrast, is discernible in the signals of both sensors (b) and (d). Finally, when considering the scaling of the y-axis in these plots, it is only for the plastic raft signal (f) where larger radiance value differences can be observed between the three bands and compared to the generally very low water leaving radiance values.

Outline: Despite these observations, these indices seem to be a highly promising approach. It would be revealing to investigate the performances on an open water surface not restricted by near land areas and bathymetry and with higher plastic abundance. It is then probable that the material-specific absorptions features will come to bear more clearly. The most important question to be answered is about the detection limit. This is defined as the smallest areal extent of a target material within a pixel that is detectable spectrally (Asadzadeh and Souza Filho, 2017). If the difference is lost in the noise, the detection limit is reached, which seems to be the case for the applied indices with a plastic proportion of 5% or less.

5.3.3 Supervised Classification

The results of both the classifications with 2 and 4 defined reference classes show similar results: The stripe patterns (#1) and (#5) are especially striking where spectral bands in the VIS and NIR regions were evaluated. The high proportion of incorrectly classified water pixels is generally easy to detect, especially for the disappointing MNF applications, where the stripe pattern could be suppressed to some extent by excluding a few bands where these features seemed to constitute the main image variability. Insofar, this data transformation approach may well have potential. Nevertheless, the MNF bands were no longer considered for the present work with the focus on plastic discrimination and identification. Quite astonishingly, the input band ranges around the specific absorption regions show very good results, including very high accuracy with regard to density variation (*Figure 4-11*). The highest accuracy resulted from the spectral subset containing 20 bands amply covering the the most prominent plastic absorption feature within the 1650 – 1800 nm spectral range (#8).

Outline: A concluding answer to the guiding question in this method subsection can explicitly be answered in the affirmative: Not only the test surfaces could be identified with different methods, but also a grading of the plastic proportion has been mapped successfully. Still, it is important to point out that the differences found – even with very high accuracy – may only be a result of reflections due to target surface geometry factors. So far, especially results of the hydrocarbon index approach, suggest that plastic materials have not been identified by

these common classification methods. Therefore, the next steps must focus on more refined methods using imaging spectroscopy for subpixel information extraction.

5.4 Plastic identification

5.4.1 Spectral Angle Mapper

The results of this method reveal some interesting findings. This is also due to the fact that only here, both images from the Irchel location were evaluated, making a comparison between the two imaging spectroscopy sensors possible since they captured the very same target within 40 minutes only.

Sensor comparison: Although the AVIRIS-NG sensor has a spatial resolution of 4.1 m (compared to 2.0 m for APEX), the comparisons between (b) and (d) show striking differences in favour of the AVIRIS-NG sensor where less commission errors result. In addition to some misclassifications at the shore, the three test areas have been clearly identified, whereas with the APEX image the test areas can only be identified with goodwill. When comparing the results with all PET reference classes in (f) and (h), the classification results do not differ as much, but a diagonal misclassified pattern in the middle of the pond is only visible in the APEX image. This might have the same cause as the stripe patterns on the Greifensee (which are due to a sensor artefact), since the orientation of this effect coincides to the E-NE – W-SW flight direction.

Classification success: While there are again numerous misclassifications that must be explained by brightness differences due to surface geometry and reflexion rather than by surface material properties, the results must be judged as rather disappointing with regard to the expected plastic identification. Even with this method, it does not seem possible to unambiguously identify the plastic material in the tested surface proportions - whereas discrimination was successful even for the lowest plastic abundance of approximately 1%. This assessment applies in particular to the lake areas. Nevertheless, image (c) is regarded as the possibly best hit of all evaluations in this study. Two of the three identified plastic spots can easily be explained: First there is the denser test field, and then there is the kayak (polyurethane surface material which is a plastic as well) which was positioned at the very edge of the gravel delta during the overflight – as is documented in *Figure 2-1 (a)* (the empty material bags were mostly covered by treetops). And what if the third clue does uncover illegally dumped plastic waste? Unfortunately, the corresponding ground reference is not available, since this position is within the inaccessible reed belt of a nature conservation zone, which can neither be observed from the lake nor from the shore and where drone data acquisition is prohibited.

Figure 5-2 points at a most relevant issue related to the SAM classification images: Based on the Hallwilersee location (and the AVIRIS-NG sensor data), it visualizes the relevance of the chosen classification threshold. The higher the allowed difference between image pixel spectrum and reference spectrum, the higher the chance to “find” the targeted material (high producer accuracy). However, misclassifications then also increase (low user accuracy). On the other hand, with very low thresholds, the risk of misclassification can be greatly avoided. The choice of the thresholds depends on the data analyst, who weighs this trade-off and through his individual decision strongly influences the mapping result. In order to avoid numerous unclassified picture areas, numerous reference classes would have to be defined. For the existing lakeshore areas, this seems extremely difficult. In the open sea, however, where the water surface shows neither bathymetry nor shore and thus adjacency effects, significantly better results are expected.

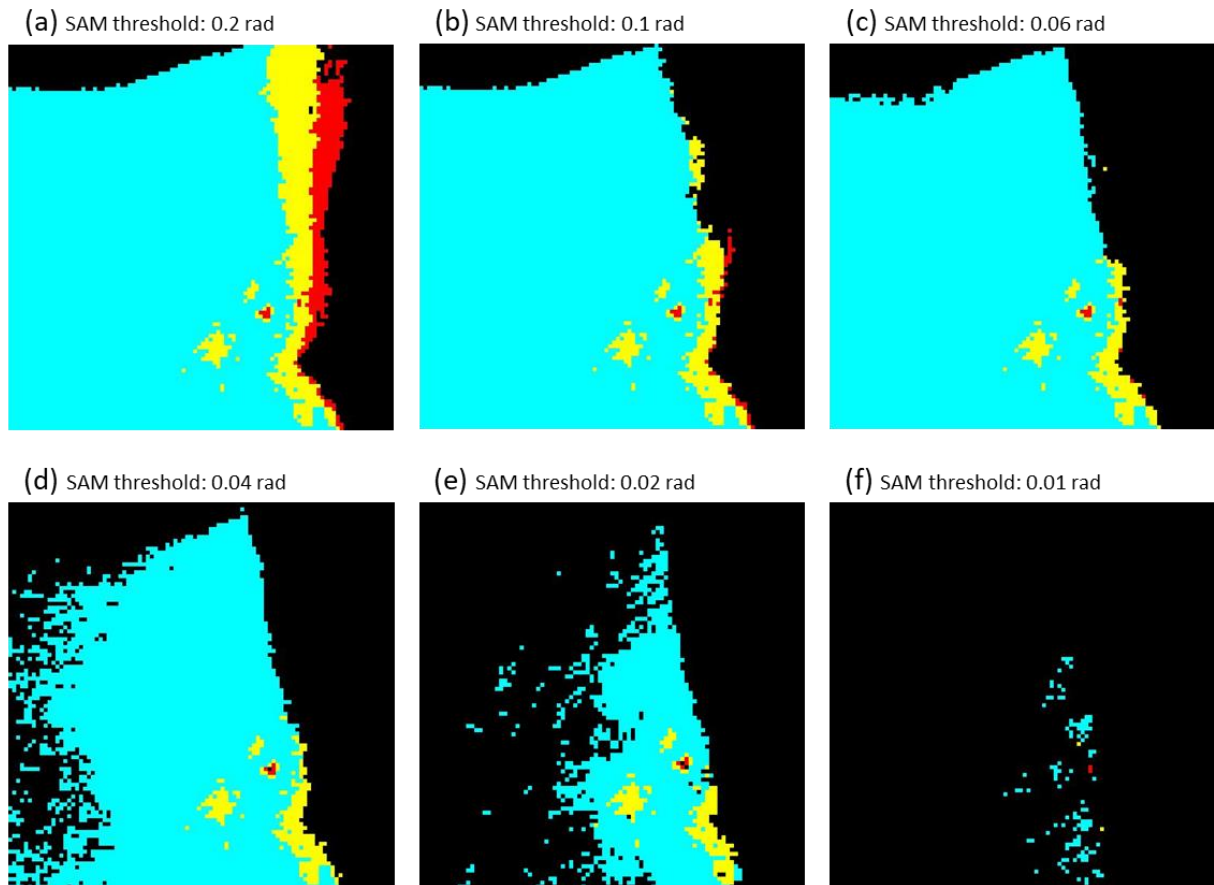


Figure 5-2: Threshold considerations for the SAM results (AVIRIS-NG image at Hallwilersee location).

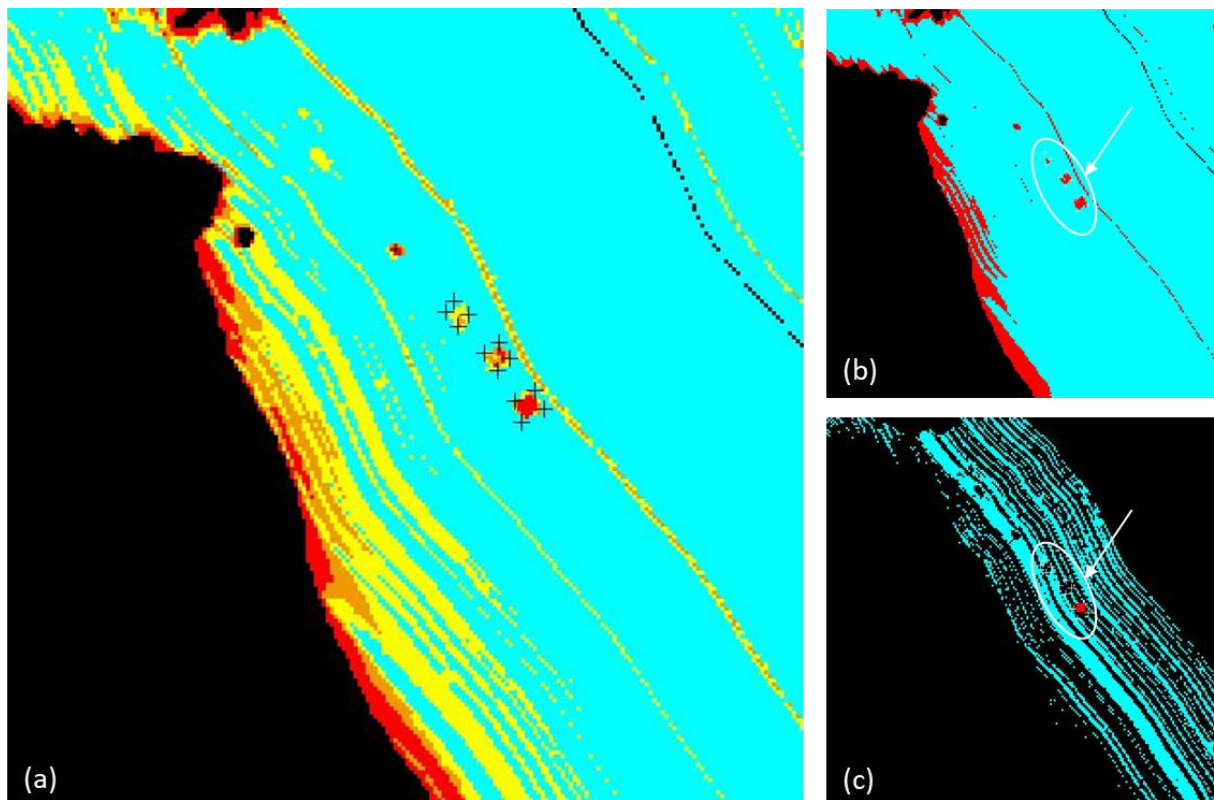


Figure 5-3: Spatial subset extent considerations for the SAM results (APEX image at Greifensee location).

A similar relativization was also conducted for the APEX results from the Greifensee location (*Figure 4-12 (e)*). Except for the sensor artefact, the results of the small subset seemed accurate. Considering a larger area (*Figure 5-3 (a)* for all PET reference classes and *(b)* for only two reference classes), however, numerous misclassifications become visible in the shore area and the smoke patches. These misclassifications again are much higher than by the AVIRIS-NG sensor in the Hallwilersee shoreline. Nevertheless, again as in the example above, with very small threshold definitions (for *(c)* a threshold of 0.03 rad was defined), such misclassifications can be greatly avoided. Again, the results in open water are expected to be considerably better without influences from the land area and shallow waters.

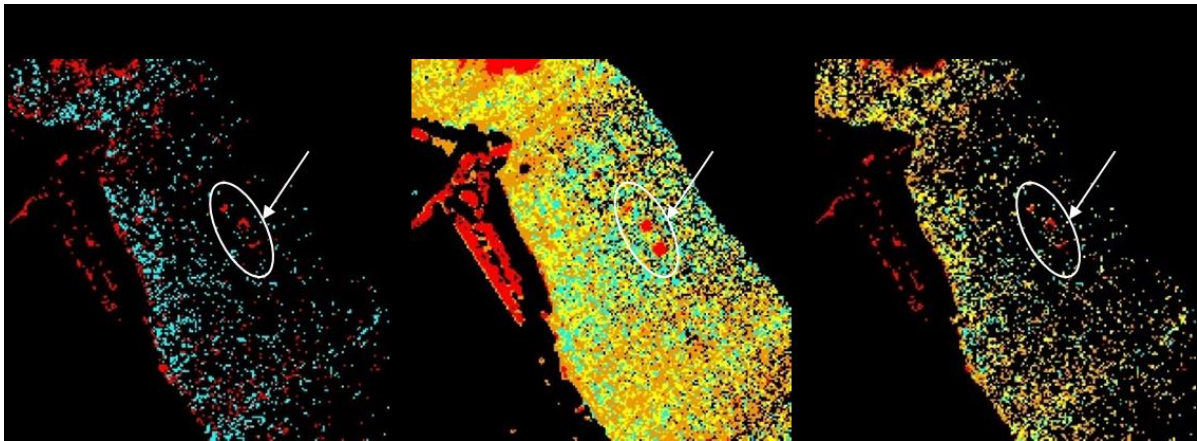


Figure 5-4: Spectral subset considerations for the SAM results (APEX image at Greifensee location).

Further modification was made based on the findings obtained with the Minimum Distance algorithm, where a **restriction of the spectral range** provided significantly better results (*Figure 4-10 (h)* and *Figure 4-11 (h)*). In addition, a reduced volume of input data would in principle be desirable for any evaluation for performance reasons. Therefore, the SAM algorithm was applied with 35 bands only, on the broadly defined spectral subset around specific plastic absorption features (APEX bands 165 – 199, 1504 – 1804 nm). Selected results are presented in *Figure 5-4*. This approach is regarded as surprisingly disappointing, because a strong reduction of the thresholds or a further restriction to only 5 spectral bands (APEX bands 187 - 191 as used in the CR application) did not improve the classification of the experimental areas. In all, at a comparable threshold, much fewer pixels were classified at all, indicating that this algorithm ideally takes the entire spectrum as basis for comparison. This observation, however, makes an efficient application to large volumes of data questionable.

Accuracy metrics: Considering all the above factors, the accuracy metrics of the classification results must be consulted with care. It is the user accuracy that yields the most informative measure, since mean and overall accuracies are rather misleading for rare target mapping. In addition, as is the case for all accuracy evaluations in this project, the reference file contains certain uncertainties, since the definition of the pixels belonging to a certain reference class could only be defined based on the visible differences (in combination with the GPS vertices). This uncertainty is particularly increased for edge pixels of the test areas.

5.4.2 Continuum Removal

If the results of the index calculations and the CR calculations are compared, no clear improvement is noticeable, thus, the expectations in applying the image spectroscopy method was not fulfilled. What might be the reason for this observation?

In *Figure 5-5*, the shape details of the spectral absorption regions are plotted for the image pixels of interest. While the inserted datatips highlight the band positions used for the index calculations, the green areas highlight the AUC for the densest PET pixels, hence the measure for the present results. Only radiance spectra are shown, since both methods can be applied on both radiance and reflectance data, and for CR, the features are generally normalized prior to calculation.

- ◁ In (a), the AUC is slightly more pronounced for the plastic containing spectrum, however the curve characteristics are very similar. In (b), no AUC was discernible in the water spectrum, but the radiance values are at an extremely low level in these wavelengths where spectral variations might contain mostly noise signals. These observations might explain the poor results for the Hallwilersee data.
- ◁ In (c), the inexistent curve features explain the negative results
- ◁ However in (d), the curve characteristics rather contradict the results, since a very small AUC feature is visible in the PET spectrum. But again, the radiance values are so low that these variations could be caused by noise only.
- ◁ In (e) and (f), the same water and PET spectra are plotted again, but differently scaled since the **plastic raft** spectrum is included here in addition. Now it becomes obvious how tiny the curve variability is in the water spectrum, compared to the raft signal. And according to the positive result identifying the plastic raft, the largest AUC is found for the 1215 nm region. This is all the more true as the absolute radiance values are significantly higher at these wavelengths.

It must be concluded that the PET abundance on the test fields are far too low for successful application of these methods. In case the plastic abundance comes close to 100%, the method using the 1215 nm region works best. This finding corresponds with the newest Hydrocarbon Index findings (Garaba and Dierssen, 2018).

A further fundamental consideration of the specific plastic features must be pointed out here: On the one hand, a too low plastic proportion in the signal has been suggested so far for the disappointing results (both for the indices and here for the CR approach). On the other hand, a spectral feature should ideally fulfil certain conditions. In addition to a material-specific exclusivity, this also includes a minimum strength (approx. 5%), a minimum spectral width (at least 5 nm) and a special peculiar shape (Kneubühler et al., 2007). A further analysis would have to systematically evaluate all these factors of different plastic materials - in combination with the respective band quality factors such as SNR and uncertainty budget as well as with all possible plastic abundancies of mixed spectra. Furthermore, based on laboratory research, it is explained that “due to the shape and transparency of PET samples, some of the spectral signatures may be influenced by reflections on the sample surface or from the background” (Moroni et al., 2015).

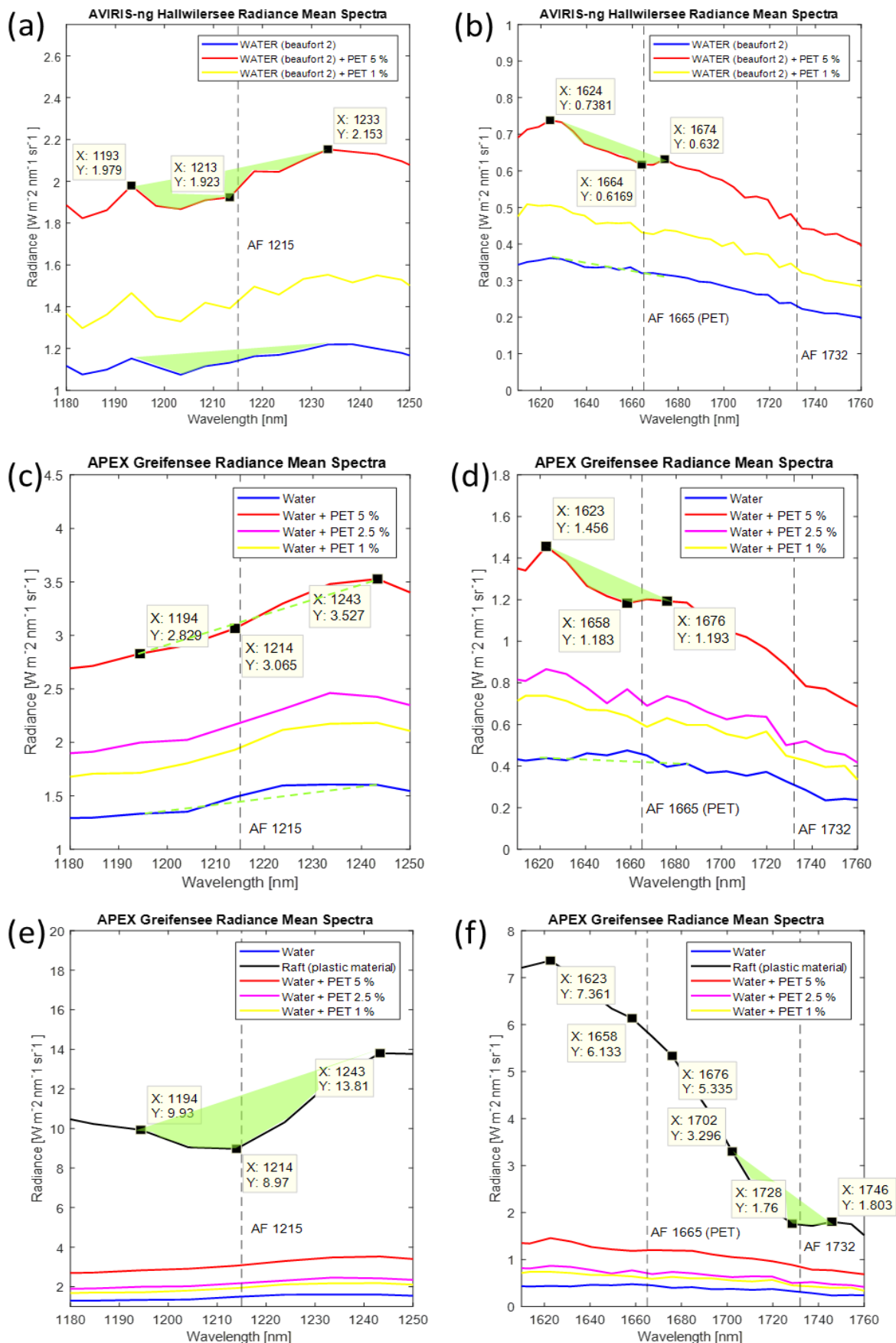


Figure 5-5: Spectral curves at absorption feature positions. Highlighted in bright green are the areas under the (not normalized) curve: the larger this area, the more distinguished the CR result should be for the selected surface materials.

5.4.3 Spectral Mixture Analysis

The results of this approach ask for explanations as to why they do not appear useful. First of all, it is assumed that the selected number of only 2 endmember spectra are insufficient to adequately represent the dominant materials on the lake surface. But “three to seven EMs are usually adequate to model any given area of an image” (Manolakis et al., 2016). Using a so-called “shade” endmember containing very low values in all bands is sometimes suggested to account for illumination variations (Jensen, 2016). However, the practical requirements appear to be disproportionately high or even impossible to meet, since the image-specific materials do not occur in so-called pure pixels in the data itself. Even if for this purpose corresponding material areas could be placed in the image section, such a procedure would not (or at best only with difficulty) be realizable for real situations with unknown targets.

As can be barely recognized in the relevant result image (c), the pixels with higher abundance of PET material are identified within the campground area only. This seems plausible since tent surfaces, chairs or camping tables, among other items, may be made of plastic materials. For a precise evaluation however, appropriate ground reference is not available. As for the floating PET bottles and contrary to expectations, no increase in this material was indicated, compared to the surrounding water. The expected pattern would be visible as brighter pixels in (b), which is not the case.

Finally, the infeasibility image is only used as an indication that allows two correct observations. High (bright) values indicate poor mapping options based on the reference endmembers being used. Correctly, this is generally more true for the land area. And the bright point in the water corresponds to the raft. Apparently, the algorithm has identified there an entirely different material than water or pet, which is correct. But it seems astonishing that only almost a maximum abundance seems meaningful enough for the method to yield meaningful results.

A more fundamental consideration is added to the context of spectral mixture approaches, in particular because the endmember spectrum used for water consisted of an average value of image retrieved water pixels near the test sites. Does the lake water fulfil so little the requirement for spectrally pure pixel signals? A method to determine the purity of spectral pixel signals is given by the **Purest Pixel Index** (PPI) algorithm. This was applied twice, once on a complete image subset including the land area, and once on a masked image to focus on the water area. In order to make a potential result pattern visible, individual value ranges were again coloured using the density slicing option. Colouring was applied from highest to lowest PPI values: green – cyan - blue – yellow – orange - red – white (unclassified pixels are black).

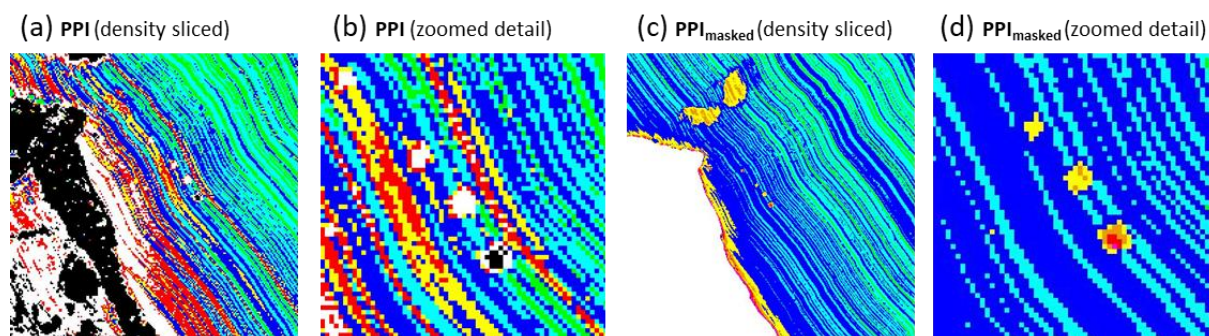


Figure 5-6: Pixel Purity Index for the APEX image at Greifensee location.

In *Figure 5-6* it can be seen that most of the water surface shows comparably high purity values (coloured in green, cyan, and blue), although the values between the test areas and the shore are somewhat lower (a). Correctly, the test areas (white and black in (b)) are clearly identifiable with lower purity values. Furthermore, as was highlighted in (d), higher PET abundancies resulted in even lower purity index values. This gradual index measure is regarded a possibility that could be used in future multi-level mapping approaches, since lower purity might indicate any floating item on a otherwise homogenous (spectrally pure) water surface.

5.5 Spectroscopic models

5.5.1 Spectral mixing model

A spectral mixing model illustrates spectral characteristics of all mixing fractions and can provide the basis for further evaluations (e.g., for absorption feature strength assessment) and in particular for modelling approaches. For the present work, the generated model was particularly important to determine the **PET abundancies in the test fields** as accurately as possible. The highly relevant findings are listed here again and compiled in the table below, supplemented with a rough estimate of the uncertainty range. From the kayak (*Figure 2-1 (b) and (d)*) the test fields seemed to have a much higher plastic density than these values now reveal. However, a very flat viewing angle is always deceptive, and since the calculated abundances fit the original calculations surprisingly well, the estimated uncertainty range may even be too cautious. Due to the close fit, the planned density is consistently mentioned in this paper. What can now be said with certainty: the test area C contains an average plastic abundance of 1% and slightly less in the marginal pixels. And it was possible to discriminate them with different algorithms.

Consequently, the detection limit for floating plastic is below 1%! This result thus falls within the one and only expected value range documented in the research literature: Based on a laboratory experiment, the lower limit of sub-pixel detection was expected "between 2.5 % and 0.3125 %" (Bochow, 2013). Our research now provides the first results obtained in a natural setting (under almost windless conditions) and can significantly narrow the laboratory-based detection limit and adjust it to a lower range.

Table 5-1: PET abundancies in the experimental test fields.

Test field	PET content	planned PET abundance	mixing model abundance	actual abundance
A	2 x 1.5l PET per m ²	5%	4%	3% - 5%
B	1 x 1.5l PET per m ²	2.5%	2%	1.5% - 2.5%
C	2 x 0.5l PET per m ²	1%	1%	0.5% - 1.5%

5.5.2 Spatial scaling

The pixel size scaling experiment, using the k-means algorithm, aims at providing information on the necessary spatial resolution. The good classification results for larger pixel sizes **indicate that typical pixel sizes of satellite images do not seem to constitute a fundamental constraint for floating plastic detection**. The spatial distribution area and of course the surface abundance of plastic will certainly be more decisive. Therefore, with regard to satellite data analysis, further investigation should evaluate spectral data of floating plastics from the WorldView-3 satellite, since simulations have demonstrated that its band configuration may be

of use for direct hydrocarbon detection when using the bands coinciding with “HC’s 1700 nm feature” (Asadzadeh and Souza Filho, 2017).

5.6 Plastic target characteristics at sea

At the end of this discussion chapter, it seems appropriate to put the findings into a larger context: To what extent can the results from the experimental setup be transferred to the realistic situations at sea? Or asked the other way: Which other factors that could not be considered within the framework of the available experimental data or which are beyond the scope of this thesis influence the detectability of plastics at sea? These theoretical considerations contribute to the answer to the research question (4) on environmental influences on floating plastic detectability.

The only floating plastic items I’ve seen at sea recently were two white plastic bottles – which turned out to be there purposely for marking the position of a crab trap at the seafloor – and one single floating plastic bag. More precisely, it was three quarters of a bright blue plastic bag, ragged, and floating an estimated 20 cm below the water surface in the Atlantic Ocean. Another three small (5 cm) objects and two almost transparent plastic sheets (20 - 50 cm) were observed on another occasion in the Aegean Sea. Again, the plastic sheets clearly drifted a few cm below the water surface. These observations were recorded within the framework of a standardized visual transect during 60 minutes, whereby 90° of the water surface is continuously monitored visually from the bow of a sailing yacht. By the way, this is exactly the procedure with which the measured concentrations of floating macro plastics are collected, serving as the basis for oceanic waste distribution modelling.

These random examples highlight two important facts when it comes to automatically detect plastic waste: First, many floating plastic items like small buoys may look exactly like rubbish (and consist of plastic material) while they are not, with their local position not necessarily indicated on even the most detailed sea chart, and with only local fishermen or sailors being aware of their position. Second, large amounts of floating plastic material float slightly below the water surface due to their individual specific weight and wave action. This observation is accurate and has already been well documented (Kukulka et al., 2012; Mace, 2012). But incoming light is not reflected fully back into the atmosphere from within the water body.

Water film scaling experiment: This theoretical knowledge was verified by means of a small laboratory experiment and must be mentioned here in a complementary way. The experiment was carried out together with Andy Hueni already in the preliminary stages of this study, and the reflectance measurements made are stored in the SPECCHIO spectral database at RSL (campaign name: Water Absorption Experiment). The purpose was to gain initial insights into the influence of water on plastic and to what extent spectral signals from a submerged plastic item could still be measured. The background for this were just such observations of submerged floating plastics. For this purpose, spectral measurements of a white plastic plate were made in the RSL laboratory with an ASD fields spectrometer. The plate was first wetted and then filled with water in increasing intervals of 0.5 – 2 mm up to a water coverage of 15 mm on the plastic material.

The most important observation when comparing spectral reflectance was that from a water film of 3 mm thickness on, almost all signals in the SWIR range > 1400 nm are suppressed. Thinner water films in this spectral region caused greatly reduced signals. Furthermore, in the NIR range (800 – 1000 nm), all signals were remarkably reduced. Only in the VIS range, the reflectance property of wet and slightly submerged plastic was only slightly attenuated. These findings are particularly important because it means that detection approaches based on the promising plastic absorption features can only be effective if the plastic target is not washed over or

submerged in water. However, as found in the analysis approaches with data from the Hallwilersee location, wetness of the (smooth) PET bottle surfaces alone did not significantly affect the results. This finding somehow contradicts the fact that "reflectance of wet particles decreased on average by 56 +/- 23% compared to dry particles with a spectral dependence increasing with wavelength from 12% in the UV to nearly 90% in the SWIR" (Garaba and Dierssen, 2018). As our field reference measurements have shown, the mean reflectance values of wet PET bottles are about 10% higher than those of dry material, an observation that is probably due to geometric factors and specular reflection. Hence, several contradicting factors may have an effect on the signal strength.

Material properties: Alterations of the target surfaces were not covered by this study, but they are well documented in the literature and include both physical and chemical weathering as well as biological processes that can lead to the development of biofilm or even to coverage with small organisms such as bivalves (*as shown in Figure 1-2 (g)*). How for example biofilms affect the optical properties of plastics is still an open research question (Goddijn-Murphy et al., 2018).

Oceanographic, atmospheric, and related acquisition geometry factors: As with all passive remote sensing methods, atmospheric conditions are decisive. Regarding the ideal viewing geometry factors, it is suggested that a viewing zenith angle of 40° and a flight direction perpendicular to the solar plane make an ideal compromise among conflicting requirements (Mobley, 1999). In addition to ideal illumination factors and good visibility, wind speed also plays an important role, since it affects sea surface geometry, sea state, vertical mixing in the upper water column (Kukulka et al., 2012) and can cause whitecaps and surface foam formation. Generally, such water surface issues, also including ocean surface reflection, sun glint, and sky glint, should be avoided (Emberton et al., 2016).

Further considerations also need to include inherent water properties, all other objects floating on the water surface, and considerations of the acquisition geometry and of the radiative transfer at the water-air interface as well as within the water body. **Inherent optical properties of water** comprise the air-water interface, water properties such as water colour ("ocean colour") and transparency, and the underwater light field (Mobley, 1999). Typical applications of optical ocean remote sensing focus on water quality and water constituents (dissolved and suspended organic and inorganic matter), and are summarized under the term "ocean colour". However, relevant optical parameters influencing the spectral signal from water surfaces – and thus the detectability of floating plastic items - concern the air-water interface where incident light is reflected (and can be measured by optical sensors) or refracts into the water body. But light that enters the underwater light field is greatly absorbed (Odermatt, 2011). This physical fact explains why water leaving radiance in the NIR (> 800 nm) is practically zero.

But it would be far too far to take a closer look at all these factors, which are undoubtedly relevant for practical application of future remote sensing approaches in ocean debris detection. Therefore, the above notes form the final part of this discussion chapter.

6 CONCLUSIONS

In this last section, selected findings are summarised with a focus on answering the research questions posed in the introduction. *Table 6-1* compiles the methods that have been applied and highlights the most promising approaches and results, exclusively referring to imaging spectroscopy data. The findings, which are based on the evaluated data from the experimental setup, are then set in a larger context: To what extent can these results be applied to the real situation of drifting plastic waste in the oceans, and what are the restrictions of the present study? Finally, the research questions posed at the beginning will be answered as far as this can be substantiated by the given data and investigations. Further research steps are sketched out, which appear to be advisable on the basis of the experience with the present work.

6.1 Summary of research work results

Table 6-1: Scored summary of the applied methods and results.

Analysis			Valuation	
Section	Method	Spectral subset	Score	Substantiation
3.1.3	Data transformation (MNF)	(all)		advantages of noise elimination and data volume reduction possibly better results from deeper water (-) supervised classification: large commission errors
3.2	Visual data enhancement	RGB		(+) discrimination of test fields (+) scaling effect of plastic abundance
3.3.1	Clustering (k-means)	SWIR (abs. feat.)		(+) spectral cluster for PET test areas with high accuracy
		(all)		(-) confounding bathymetry information in the VNIR bands
3.3.2	Established Hydrocarbon Indices	abs. feat.		(-) plastic surface fraction must assumingly be much higher than the tested 5% (estimation: ~ 50%)
	Specifically developed PET Index	abs. feat.		(+) material specific absorption feature position considered (-) required minimum surface fraction unknown (+) high producer accuracy for small surface fractions (< 5%) (-) ambiguous results, possibly for surface geometry/reflection reasons
3.3.3	Supervised classification (Minimum Distance)	(all)		high accuracies (~80% UA) for 2 classes; lower accuracies if small surface fractions are also classified
		MNF bands		(-) large commission errors
		abs. feat.		(+) very high accuracies (90 - 100%) for higher wavelength regions
3.4.1	Spectral Angle Mapper	(all)		(+) very high accuracies on lake surfaces (-) results highly depend on parameter definition (-) confounding shore areas result in commission errors especially for the smallest PET abundance class
	Spectral Angle Mapper	abs. feat.		(-) no useful mapping results
3.4.2	Continuum Removal	abs. feat.		(+) plastic identification only for very high abundance (-) generally inferior results in comparison to index calculation
3.4.3	Spectral mixture analysis	(all)		(-) very elaborate and challenging approach; risk of unknown endmembers
3.5.1	Spectral mixing model	(all) + reference spectra		(+) allows estimation of plastic fraction if reference spectra is known
3.5.2	Pixel size scaling model	(all)		(+) provides indications of minimum pixel size requirement
5.4.3	Pixel Purity Index	(all)		(+) provides a measure for multi-level mapping approaches
B	Derivative Spectroscopy	(all)		(+) method for absorption feature localisation

6.2 Answers to the research questions asked

As was already apparent during the discussion of the individual evaluation results, our research questions can not be conclusively answered here. This applies in particular to the surface fraction, for which the experimental data does not offer all necessary evaluation options. However, on the basis of the analyses made, the following answers can be given regarding the research questions already posed in the introduction:

(1) What plastic surface densities on water bodies can be identified from spectral data?

An answer to this question can only be incomplete. However, here, a most relevant finding of this thesis can be highlighted: Our results, achieved for the first time for small surface fractions of floating plastic under real conditions, allow to significantly lower and narrow the detection limit range based on laboratory data and documented in the research literature (Bochow, 2013): **A surface fraction of less than 1% plastic can be distinguished from the surrounding water in imaging spectroscopy data.**

But the surface density is not as relevant as the signal's plastic fraction. And since the spectral signal is acquired for each image pixel, this question is directly related to the sensor's spatial resolution. With the AVIRIS-NG sensor, it was possible to detect PET abundancies of about 1% in pixels covering a surface area of 16 m². If the imaging spectroscopy data acquisition from the Zeppelin had been successful from the short distance of 150 m above the water, the resulting HyperSpec pixel area would have covered about 50 cm² (Table 2-1). Thus a single plastic cap floating on the Irchel pond should have been identifiable. Unfortunately, this theoretical estimation could not be verified.

(2) What spatial resolution is needed for detection?

This factor is directly related to the surface density of the targeted material. It has been shown that a pixel size up to about 10 m does not seem to be a limiting factor. One single PET bottle can be detected in a pixel area of 1 m². Thus, theoretically, if 100 bottles were afloat on a surface area of 100 m² (the area typically covered by a satellite pixel), they could possibly be detected from space - depending, however, on the spectral resolution and radiometric quality of the sensor.

(3) What spectral information (spectral range and resolution) is relevant to distinguish between water and plastic surfaces?

It is obvious that for material distinction, only imaging spectroscopy data are useful, consisting of very narrow spectral bands of ideally 5 – 10 nm. The NIR region of the spectrum is best for specific material identification, however, the relevant spectral signals in this range are lost as soon as the targets are even only minimally under water. Specific absorption features in plastic spectra vary slightly with material type and material surface condition, but the most important spectral ranges are around 1215 nm and 1660 – 1730 nm.

Furthermore, it is most relevant to clearly separate two goals: Simple detection of a slightly different spectral signal might at best point to any floating item on an otherwise homogeneous water surface. But for specific material identification, much higher sensor requirements seem to apply.

(4) Which factors influence the detectability?

This question was only touched upon with the practical analyses, since most of the relevant parameters are not covered by the available experimental data. In theory, however, there are several known factors. The most direct influence on optical detectability probably comes from material properties (specific weight,

degraded surface, hitchhikers, biofilm) on the one hand and physical environmental factors such as sea state and atmospheric conditions on the other.

Restrictions of this study: Here it seems appropriate to emphasize again the limitations of this study, because the answers to the research questions are based on an experimental setup which was not intended to correspond precisely to the real situation of the floating plastic debris in the oceans. Unlike ocean debris, only one plastic type (PET) without surface degradation or biofouling effects was investigated on shallow water bodies with smooth water surfaces. The tested plastic surface abundancies probably correspond only to extreme situations and do not reflect typical ocean waste concentrations. In addition, possibly relevant factors of acquisition geometry and illumination factors were not further considered, as they could not be influenced for the collected imaging spectroscopy data.

6.3 Outlook on further research steps

While assessing the current situation of this research topic early in the project process, it became apparent that the research questions asked concern many more factors and open research questions than can be investigated within the framework of a master's thesis. It is also becoming apparent that a combined approach would probably be more suitable than focusing on one specific processing methodology. Incorporating knowledge based information about e.g. sea state and floating item positions (ships, icebergs, buoys) with spectral feature analysis might be a sound approach. Elaborate radiation transfer models might provide the theoretical basis to break down the apparent optical properties of the sea surface in order to identify those variabilities caused by minimal plastic fractions. And in particular, optimized atmospheric correction algorithms over water surfaces are to be mentioned here.

Finally, the need for combined approaches has already been pointed out several times: To develop the capability for detection and ultimately removal of derelict fishing gear (or floating debris in general) from the open ocean, several studies have proposed combined strategies (Morishige and McElwee, 2012; Pichel et al., 2012; McElwee et al., 2012). Such approaches typically include:

- ◁ characteristics of the targeted objects (e.g., material type, size, colour, and spectral signatures)
- ◁ indirect estimation of likely locations using oceanographic modelling, combined with data on sea state and atmospheric conditions (wind force and direction)
- ◁ and direct observation of the sea surface using remote sensing observation techniques.

And it is the latter aspect that relates to the study presented here. Therefore, this outlook on further research summarizes those factors which will most likely need to be considered in subsequent works with regard to a possibly realistic solution development. Based on the findings in this thesis it is suggested to focus on these subsequent research steps:

Proposals for further investigation:

- ◁ Inclusion of further **plastic materials:** Experimental use and spectral analysis of other typical plastic materials, ideally consisting of real marine debris (degraded, brittle, biofilm coated). Identification of their specific absorption features (*cf. Appendix B*) which may be at slightly different wavelength positions depending on material properties.

- ◁ Comprehensive investigation of specific **absorption features** for different plastic proportions in the spectral signal, and determination of detection limits for all common plastic types (*as discussed in Section 5.4.2*).
- ◁ Experimental data acquisition **in open water** where no undesired adjacency effects from nearby land and bathymetry signals influence the plastic detection approaches in an undesired way. It is expected that even lower surface density (< 1%) can be identified with higher accuracy (*cf. Sections 5.1 and 5.4.3*).
- ◁ In case of very promising results with consideration of the plastic absorption features: Evaluation of **satellite** data with high spectral resolution at these wavelength regions (e.g., WorldView-3). Alternatively, determination of required spectral range and resolution for floating plastic waste identification, at best in view of the technical possibilities for satellite sensor development.

Further ideas are aiming at the development of an algorithm for the automatic detection of larger floating plastic items. To this end, a variety of additional information would have to be integrated, such as on wind and sea state, ship positions, drift ice, to name only the most obvious. Methodological and technological approaches that are currently the subject of research would also need to be taken into account. This includes general approaches of ocean remote sensing using imaging spectroscopy, because remote sensing applications have typically been focused on land areas while ocean colour satellites have coarse spatial resolution – a situation which is changing with the further development of imaging spectroscopy satellites by now (Giardino et al., 2018).

While the present work is concluded with this optimistic outlook, ideally its findings possibly contribute another small puzzle stone in research for necessary solutions to the pressing environmental problem of ocean plastic pollution.

APPENDIX A: SCIENTIFIC LITERATURE

Table A-1: Scientific papers addressing marine pollution detection and identification. While all papers relating to remote sensing approaches are included, only a selection of surveys applying the visual transect or net trawl sampling methods are included as examples.

Scientific Paper			Observation			Achievements	
Reference	Location	Debris	Category	Platform	Sensor	Method	Results
(Acuña-Ruz et al., 2018)	Shoreline (Chile)	beached macro plastic	spectral data	satellite	World View-3	SVM classification using spectral library references	OA of 88% for 50 tons of beached debris classification
(Aoyama, 2016)	Sea of Japan	floating macro debris	spectral data	satellite	World View-2	SAM (using 4 spectral bands: RGB + NIR)	identification of pixels containing possible marine debris (spectral variations found)
(Biermann, 2019)	Coastal waters	Aggregated floating debris	spectral data	Satellite	S2	Floating Debris Index in combination with NDVI: "Evidence that aggregated materials that include floating plastics are detectable by Sentinel-2, even on subpixel scales."	
(Chambault et al., 2018)	Azores, Madeira (Atlantic)	floating macro plastics	visual transects	(ship)		documentation of distribution and item category	
(Eriksen et al., 2013)	South Pacific subtropical gyre	floating plastics	manta net trawls	(ship)		average abundance: 26'898 (max. 396'342) particles/km ² ; average mass: 70.96 g/km ²	
(Feygels, V., Aitken, J., Ramnath, V., 2017)	GPGP (Pacific)	large (>0.5m) floating items	integrated fullwave lidar, RGB camera, and spectral instrument	Airborne 400 m (AGL)	Optech T-4800; ITRES SASI	Possibility shown in using lidar waveforms to transform two-dimensional estimates of plastic abundance into three-dimensional estimates of plastic volume	
(Garaba et al., 2018)	GPGP (Pacific)	large (0.6 – 6.8 m) floating ocean debris	Spectral data and aerial photo	Airborne 400 m (AGL)	RGB; SASI-600	Selection of largest floating items in RGB photos; spectral feature comparison for the largest objects in the SWIR.	Suggesting "that, at 5% pixel coverage, the 1732 nm feature might not be appropriate for detecting ocean plastics".
(Garaba and Dierssen, 2018)	plastic bearing material on land	marine-harvested micro and macro plastics	spectral data	airborne	AVIRIS (classic)	Imaging spectroscopy approaches with focus on spectral absorption features around 1215 and 1732 nm	Spectral measurements "provide a foundation for advances towards remote detection of plastics from various platforms"
(Goddijn-Murphy et al., 2018)		floating marine macro plastic	spectral signal	(concept model)		Theoretical reflectance model of sunlight interacting with a sea surface littered with plastic based on geometrical optics and spectral signatures	

Scientific Paper			Observation			Achievements	
Reference	Location	Debris	Category	Platform	Sensor	Method	Results
(Goddijn-Murphy and Dufaur, 2018)		EPS, HDPE, and PET samples	spectral signal	Field and laboratory	ASD Fieldspec Pro	Spectral reflectance measurements with plastic abundancies of 25%, 50%, 75% and 100% applied on a single-band algorithm (850 nm) and a dual-band algorithm (1660 – 1730 nm) showed some trends.	
(Goddijn-Murphy and Williamson, 2019)			Emissivity values of different polymers & water	(radiative transfer theory)	thermal infrared	"Thermal infrared (TIR) sensing could potentially monitor plastic water pollution but has not been studied in detail."	
(Kako et al., 2012)		floating debris		airborne (50 – 150 m AGL)	RGB camera	Low-altitude remote sensing system using a balloon equipped with a digital camera; data analysis using colour-space transformations	"estimate the number of objects from the photographs"
(Kako et al., 2018)	Oregon coast (USA): shoreline	beached macro marine debris			local webcam	Time series	temporal variability of beached marine debris abundance
(Kataoka et al., 2018)	Vancouver Island (Canada): shoreline	beached macro marine debris	shoreline aerial photos	airborne (500m - 1000m AGL)	RGB camera (Nikon D750)	pixels of marine debris identified based on colour differences from beaches	percent cover of debris was significantly related to Ekman offshore flows and winds
(Kylili et al., 2019)		floating macro plastics	aerial photo	(UAV or from ship)	RGB camera	Deep Learning algorithm to automatically identify three types of large floating plastic items (bottles, buckets and straws)	
(Mace, 2012)	Open sea		integrated approach	Satellite and airborne radar	various	Combined approach using models, satellite and airborne radar data and visual surveys to detect potential accumulation zones for direct search	
(Morishige and McElwee, 2012)	Hawaiian Archipelago	derelict fishing gear	integrated approach	UAV from ship (pilot project failed) - unknown applicability		strategy outline (need for development in the RS field)	
(Moy et al., 2018)	Hawaiian Islands	beached debris (> 0.05 m ²)	aerial photo	airborne (610 m AGL)	RGB cameras	aerial photographs (and visual analysis using a GIS)	total 20'658 debris items identified on 176 km coastline
(Pichel et al., 2012)	Gulf of Alaska (GoA pilot survey 2003)	Derelict fishing gear in coastal waters and open sea	Visual observation	airborne		Strategy outline: integrated approach (convergence zones, buoy tracking, satellite data on wind and weather, airborne sighting)	
(Ryan, 2014)	Open ocean (South Atlantic)	Floating macro plastic		(ship)		Shipboard sighting surveys	281 items during 79 h and 1963 km of transects
(Topouzeli et al., 2019)	Coastal waters (Greece)	artificial targets (PET, LDPE, derelict fishing nets)	feasibility study	UAV and satellite	RGB; S2	Demonstrated usefulness of UAV in improving geo-referencing of satellite images. The "identification of the plastic types and shapes will require multi- to hyperspectral imaging"	

APPENDIX B: DERIVATIVE SPECTROSCOPY

Differentiation – the mathematical function to define the slope of a curve – is called derivative spectroscopy if applied to spectroradiometer derived curves. Its application on the continuous slopes of spectra involves the conversion of a normal spectrum into its first, second, or higher derivative spectra. While this method cannot provide more information than is contained in the original spectrum, it can be used to highlight subtle details of a curve and resolve overlapping spectral features while suppressing or eliminating unwanted information or noise (Jensen, 2016; Tsai and Philpot, 1998). Moreover, derivatives of second or higher order have the advantage of being insensitive to illumination variability (Dehnavi et al., 2017; Borengasser et al., 2008).

This method was originally developed in analytical chemistry for application on laboratory reflectance spectra. In the field of remote sensing, its application has been limited because of the differences between the laboratory and field settings. Not all of the methods can be transferred easily to remote sensing data, especially because of atmospheric absorption of the solar illumination, varying illumination parameters, topography influence and mixed pixels in the natural environment (Jensen, 2016). While in remote sensing application, first order derivatives have been used for target discrimination (Dehnavi et al., 2017), first-order and second-order derivatives of the continuum-removed spectrum were used in combination with continuum removal in a novel spectral shape fitting method (Qu and Liu, 2017). The method was also applied for canopy nitrogen content estimation (Mitchell et al., 2012) and bathymetry information (Louchard et al., 2002). It was also applied in absorption feature position detection (Garaba and Dierssen, 2018; Tsai and Philpot, 1998). Its main advantage related to the detection of floating plastics is seen in analysing the wavelengths of absorption features specific to plastic materials, as it has been applied by in Garaba and Dierssen (2018).

Here, two approaches in the context of plastic spectra detection were selected and implemented using MATLAB: First, a rather exploratory approach was chosen with the purpose of finding subtle differences between selected image pixels containing plastic materials and pixels of water surface. In a second approach, a derivative analysis algorithm to extract absorption band positions was applied to pure reference spectra as developed by Huguenin and Jones (1986).

In the **first approach**, mean radiance spectra from the Greifensee location were calculated for the densest PET test area and for the surrounding water surface. These spectra were then plotted together with their calculated first derivatives. Furthermore, the difference of the resulting first derivatives was plotted in order to have a new view on the spectral differences for visual analysis.

The **second approach**, based on the only concisely documented algorithm for absorption position determination found in the literature (Huguenin and Jones, 1986) was applied as proposed, using reference spectra of floating PET targets from the SPECCHIO spectral database. This method usually is applied on reflectance spectra where preparing smoothing and interpolating steps are applied first (Tsai and Philpot, 1998). First, the mean PET reflectance spectrum was calculated and smoothed afterwards using a moving linear average filter with a span of 10 nm. This chosen filter window size lies in the middle between the applied spans (Huguenin and Jones, 1986; Garaba and Dierssen, 2018) and seemed reasonable after visual inspection. Interpolation was not necessary as the ASD fieldspectrometer measurements are acquired in regular steps of 1nm bands. Then, first to fifth derivatives of the smoothed spectrum were calculated, applying the same smoothing filter for each derivative again, since smoothing is required continually to minimize signal distortion (Huguenin and Jones, 1986). Finally, those wavelength positions were selected as candidates for absorption feature maxima where several conditions were met, as proposed by Huguenin and Jones (1986).

Since the documented procedures yield no convincing result, own ideas were additionally implemented: Candidates for absorption features were determined based on rules of differential calculation. The second condition for locale curve minima was defined - after the optimal span has been iteratively narrowed down - in a range of +/- 0.002 instead of 0 in order to take the discontinuous spectral curve characteristic into account.

While derivative spectroscopy is usually calculated for reflectance data, a first impression of the spectral characteristics can be gained from radiance spectra as well, provided the atmospheric influences are considered. In all subplots of *Figure B-1*, both the mean radiance of the densest PET test area as well as of the raft – which is presumably made of PE – are used for comparison. The plastic raft spectrum was considered because the mixed PET pixel might not contain the necessary plastic signal fraction. The vertical dotted lines indicate those wavelengths where specific plastic absorption features are known: 931, 1215, 1471, 1732, and 2310 nm.

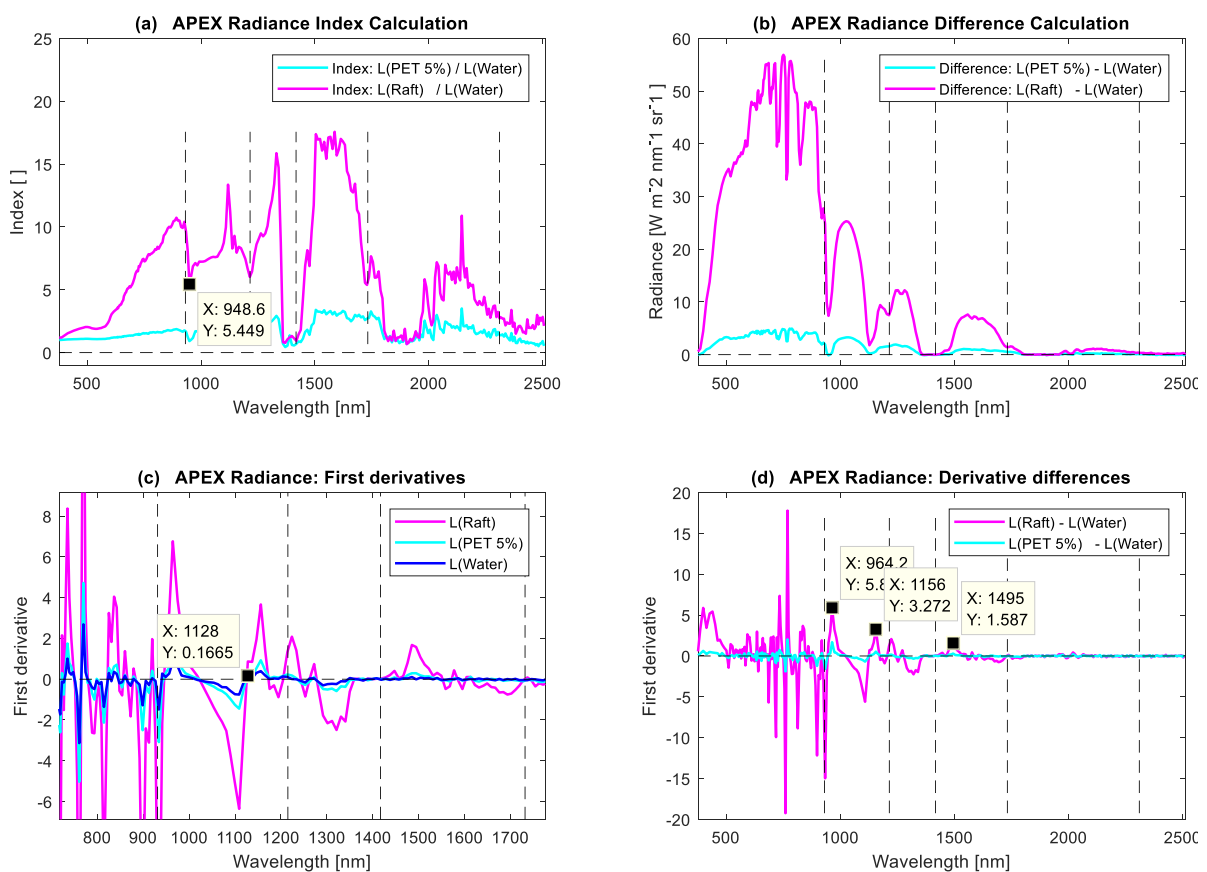


Figure B-1: First impressions of the spectral characteristics using index, difference, and first derivative calculation plots

In both the radiance difference and radiance index calculations, low values occur at these positions at 1215, 1417, and 1732 nm. The indices expected at 931 nm show a shift towards 948 nm (datatip), whereas the 1417 nm absorption feature is lost due to the atmospheric water vapor absorption band where very low values result for all materials. The 2310 nm absorption feature is also lost in extremely low values due to atmospheric absorption with the index showing mostly noise. For the differences in subplot (b), the expectation was at best to find a hitherto unknown anomaly. However, the difference plot seems to more or less reflect the atmospheric transmissibility which is highest in the visible spectral range. Still, the differences between water and plastic raft

radiance show dissimilar curves at the known features at 931, 1215 and 1732 compared with the difference curve for the 5% PET surface. Subplot (c) shows an enlarged part of the first spectral derivatives. According to the fundamentals of differential calculus, local minima of a curve can be found at positions where its first derivative equals zero and the second derivative is positive (Storrer, 1992). The 1128 nm (datatip) is of interest where the known features meet this criteria most obviously. Subplot (d) shows local maxima at 964, 1156 and 1493 nm (datatips) where the curve gradient differs the most.

Differences in the radiance-difference plot (*Figure B-1, subplot (b)*) indicate once more that the 5% PET abundance might not be sufficient to successfully interpret the plastic absorption features or even to identify the material, since the spectral signal shows an expected variation only for the plastic raft (with an estimated abundance close to 100%) at the specific plastic absorption positions.

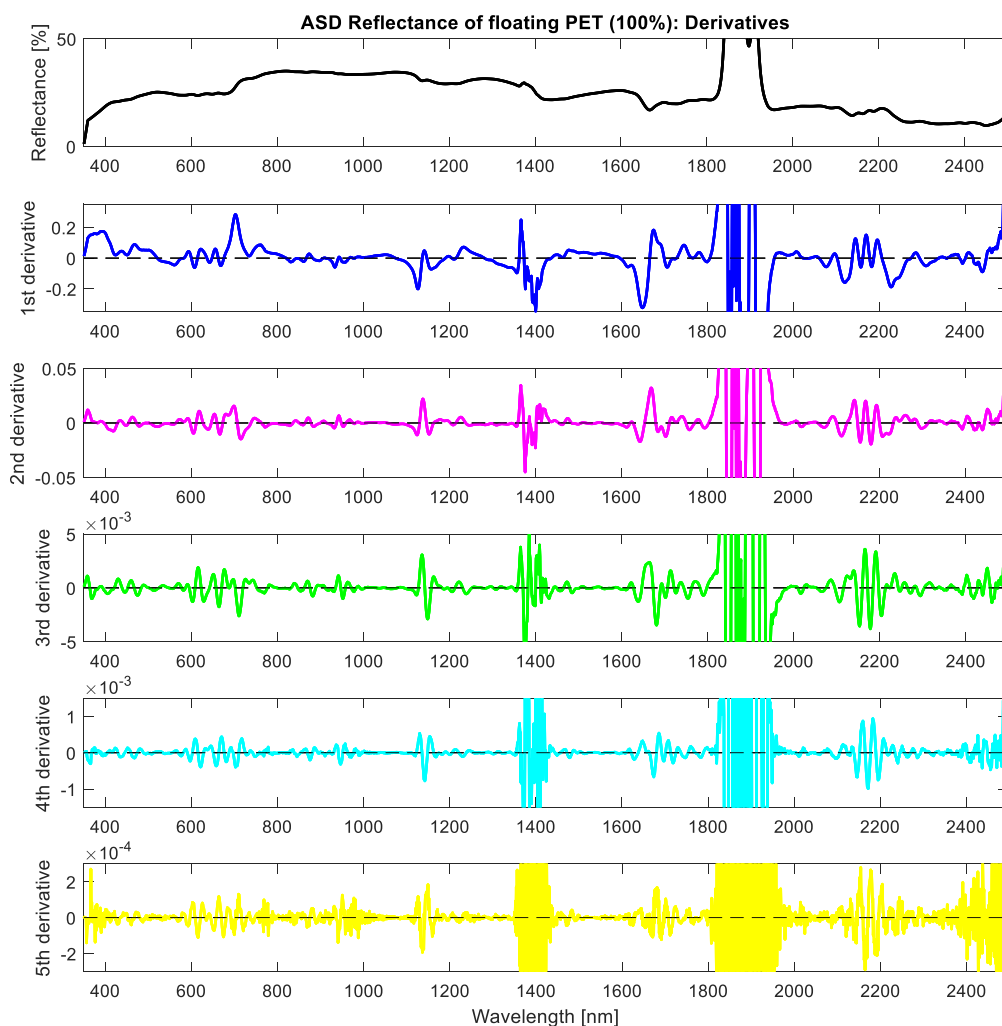


Figure B-2: First order to fifth order derivatives calculated for the mean PET reflectance spectrum.

In *Figure B-2*, the Y-scales of the derivatives are scaled differently so that even minimal variations became visible. It is important to note that the atmospheric absorption features around 1400 and 1850 nm were partially obscured by the mean value calculation of the reflectance spectrum. Therefore, these regions should be considered accordingly in the interpretation as they were not blanked out in the plots.

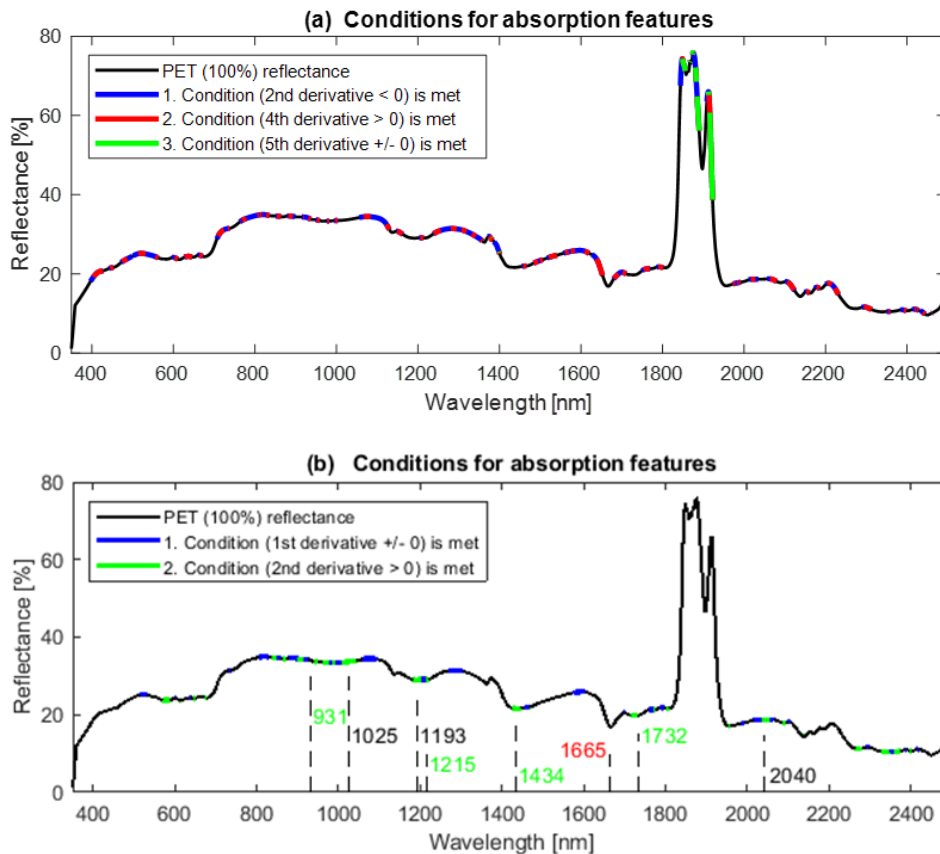


Figure B-3: Coloured spectral ranges of the mean PET reflectance where certain conditions for absorption features are met.

Figure B-3 illustrates not only the spectral ranges of absorption feature candidates following the conditions defined in the literature (a) but also the conditions defined according to mathematical rules (b). In both plots, only those spectral regions highlighted in green meet all the conditions, which is only in the prominent atmospheric absorption feature around 1850 nm in the first case (a) but for several regions in (b), where the most obvious in the NIR are indicated with dotted lines. The wavelength regions annotated in green correspond precisely to well-known plastic absorption features, while the annotated (in red colour) feature at 1665 nm was expected to be identified – since it is present in the spectrum, as documented in Figure 5-5 (b) and (d)), but was not indicated by this approach. Further wavelength positions for absorption feature candidates at 1025, 1193 and 2040 nm were visually investigated in the spectrum, but no distinguishable feature could be detected, partly due to very low values possibly superimposed with noise.

Surprisingly, the **method for absorption feature candidate locations** did not yield any result except for the atmospheric absorption region around 1850 which cannot be counted. However, the mathematical conditions were met e.g. for the regions at 1217, 1437 (atmospheric absorption) and 1725, where the well-known plastic absorption features could be confirmed. However, it is irritating that the feature at 1715 - 1733 nm for the PET spectrum was found at this position and not closer to the 1665 nm range where the index calculations (Section 3.3.2) and the CR calculations (Section 3.4.2) pointed to this shifted feature position for the specific PET plastic material.

ACKNOWLEDGMENTS

This work would not have been possible without a great deal of support, particularly in connection with the experimental data collection. Right from the preparatory phase, I was able to experience the great goodwill that this research project received from all sides. This began with the gathering of hundreds of PET bottles, with which I was supported first and most helpfully by Priska Fäh and her friendly team at Spar Weesen. The Volg team in Beinwil am See and the employees of the Recyclingparadies in Reinach AG showed the same uncomplicated readiness to help. At that time no one had any idea what role these bottles still had to play.

I am also grateful to various official bodies. In particular, Mr Sebastian Meyer from the Office for Landscape and Water Management (BVUALG) for the permit on Hallwilersee, Mr Hanspeter Tschanz from the Office for Landscape and Nature for the special permit issued for the V-C protection zone on Greifensee, and Mr Hanspeter Schmid from the municipality of Aesch LU for the access permit are to be mentioned here.

I am also very grateful to many scientists of the RSL team. The installation of these 492 PET bottles on the waters would hardly have been possible without the dedicated support and material transport by Simon Trim at the Hallwilersee location and the great help of Rogier de Jong with his canoe on Greifensee. During all these days of flight data collection Andy Hueni kept me informed about the short-term planning, he always found time for my practical and organizational concerns and helped me in many ways on that eventful summer day in the Irchel park. I thank Felix Morsdorf for the drone flights over the Irchel pond, Philip Joerg for all the helpful advice, and Mathias Kneubühler knows how happy I was for his transport services.

My thanks also go to Daniel for his great support and Mark for his valuable feedback on the text. Above all, my sincere thanks for his valuable guidance go to my supervisor Andy, who has encouraged and supported me since my first question on the chosen topic.

DANKSAGUNG

Diese Arbeit wäre nicht möglich gewesen ohne vielfältige Unterstützung, insbesondere im Zusammenhang mit der experimentellen Datenerhebung. Bereits während der Vorbereitungsphase durfte ich die grosse Hilfsbereitschaft erfahren, die diesem Forschungsprojekt von überall her entgegengebracht wurde. Es hat mit der Beschaffung von hunderten PET-Flaschen begonnen, bei der mich zuallererst im Spar Weesen Priska Fäh und ihr freundliches Team hilfsbereit unterstützt haben. Dieselbe unkomplizierte Hilfsbereitschaft haben auch das Team vom Volg in Beinwil am See und die Mitarbeitenden des Recyclingparadieses in Reinach AG gezeigt. Damals hat wohl noch niemand geahnt, welche Rolle diese Flaschen noch spielen würden.

Für die Durchführung der Experimente bin ich auch verschiedenen amtlichen Stellen zu Dank verpflichtet. Hier sind insbesondere Herr Sebastian Meyer vom Amt für Landschaft und Gewässer (BVUALG) für die Bewilligung auf dem Hallwilersee, Herr Hanspeter Tschanz vom Amt für Landschaft und Natur für die erteilte Sondergenehmigung für die Uferschutzzone V-C auf dem Greifensee sowie Herr Hanspeter Schmid von der Gemeinde Aesch LU für die Zufahrtserlaubnis zu nennen.

Auch vielen Wissenschaftlern vom RSL bin ich zu Dank verpflichtet. Die Installation dieser 492 PET-Flaschen auf den Gewässern wäre ohne die engagierte Unterstützung und den Materialtransport durch Simon Trim am Hallwilersee und durch die grosse Hilfe von Rogier de Jong mit seinem Kanu auf dem Greifensee kaum machbar gewesen. Während all diesen Tagen der Flugdatenerfassung hat mich Andy Hueni nicht nur über die kurzfristige Planung auf dem Laufenden gehalten, er hat immer auch für meine praktischen und organisatorischen Anliegen Zeit gefunden und an jenem ereignisreichen Sommertag im Irchelpark mannigfaltig mitgeholfen. Felix Morsdorf danke ich für die Drohnenflüge über den Irchelteich, Philip Joerg für all die hilfreichen Tipps, und Mathias Kneubühler weiss wie froh ich um seine Transportdienste war.

Mein Dank gilt auch Daniel für seine grosse Unterstützung und Mark für sein wertvolles Feedback zum Text. Und schliesslich gilt mein ganz besonderer Dank Andy, der diese Arbeit begleitet und mich seit meiner ersten Frage zum gewählten Thema immer ermutigt und unterstützt hat.

REFERENCES

- Acuña-Ruz, T., Uribe, D., Taylor, R., Amézquita, L., Guzmán, M.C., Merrill, J., Martínez, P., Voisin, L., & Mattar B., C. (2018). Anthropogenic marine debris over beaches: Spectral characterization for remote sensing applications. *Remote Sensing of Environment*, 217, 309–322.
- Andrady, A.L. (2011). Microplastics in the marine environment. *Marine Pollution Bulletin*, 62, 1596–1605.
- Aoyama, T. (2016). Extraction of marine debris in the Sea of Japan using high-spatial-resolution satellite images. In R.J. Frouin, S.C. Shenoi, & K.H. Rao (Eds.), *Remote Sensing of the Oceans and Inland Waters: Techniques, Applications, and Challenges* (p. 987817): SPIE.
- Asadzadeh, S., & Souza Filho, C.R. de (2017). Spectral remote sensing for onshore seepage characterization: A critical overview. *Earth-Science Reviews*, 168, 48–72.
- Auta, H.S., Emenike, C.U., & Fauziah, S.H. (2017). Distribution and importance of microplastics in the marine environment: A review of the sources, fate, effects, and potential solutions. *Environment international*, 102, 165–176.
- Bailey, S.W., Franz, B.A., & Werdell, P.J. (2010). Estimation of near-infrared water-leaving reflectance for satellite ocean color data processing. *Optics express*, 18, 7521–7527.
- Barnes, D.K.A., Galgani, F., Thompson, R.C., & Barlaz, M. (2009). Accumulation and fragmentation of plastic debris in global environments. *Philosophical transactions of the Royal Society of London. Series B, Biological sciences*, 364, 1985–1998.
- Bertschi, S. (2018). Plastic in aquatic systems - dimensions of a global pollution problem. UWW163: Literature research semester paper (unpublished). University of Zurich. Zürich.
- Biermann, L. (2019). *Detecting Floating Debris. Towards a method for detecting macroplastics in coastal waters using data collected by earth observation satellites*. EGU General Assembly 2019. Vienna.
- Bochow, M. (2013). *Potential of imaging spectroscopy for mapping plastic litter in the marine environment. A laboratory experiment*. EARSel, 2013.
- Borengasser, M., Hungate, W.S., & Watkins, R. (2008). *Hyperspectral remote sensing. Principles and applications*. Boca Raton, Fla.: CRC Press.
- Brach, L., Deixonne, P., Bernard, M.-F., Durand, E., Desjean, M.-C., Perez, E., van Sebille, E., & Ter Halle, A. (2018). Anticyclonic eddies increase accumulation of microplastic in the North Atlantic subtropical gyre. *Marine Pollution Bulletin*, 126, 191–196.
- Chambault, P., Vandeperre, F., Machete, M., Lagoa, J.C., & Pham, C.K. (2018). Distribution and composition of floating macro litter off the Azores archipelago and Madeira (NE Atlantic) using opportunistic surveys. *Marine Environmental Research*, 141, 225–232.
- Cloutis, E.A. (1989). Spectral reflectance properties of hydrocarbons: remote-sensing implications. *Science (New York, N.Y.)*, 245, 165–168.
- Congalton, R.G., & Green, K. (2009). *Assessing the accuracy of remotely sensed data. Principles and practices*. (2nd ed.). Boca Raton, Fla.: CRC Press.
- Cozar, A., Echevarria, F., Gonzalez-Gordillo, J.I., Irigoien, X., Ubeda, B., Hernandez-Leon, S., Palma, A.T., Navarro, S., Garcia-de-Lomas, J., Ruiz, A., Fernandez-de-Puelles, M.L., & Duarte, C.M. (2014). Plastic debris in the open ocean. *Proceedings of the National Academy of Sciences*, 111, 10239–10244.
- Cressey, D. (2016). The Plastic Ocean. Scientists know that there is a colossal amount of plastic in the oceans, but they don't know where it all is, what it looks like or what damage it does. Bottles, bags, ropes and toothbrushes: the struggle to track ocean plastics. *Nature*, 536, 263–265.

- Dehnavi, S., Maghsoudi, Y., & Valadan-zoej, M. (2017). Using spectrum differentiation and combination for target detection of minerals. *International Journal of Applied Earth Observation and Geoinformation*, 55, 9–20.
- Demšar, U., Harris, P., Brunson, C., Fotheringham, A.S., & McLoone, S. (2013). Principal Component Analysis on Spatial Data: An Overview. *Annals of the Association of American Geographers*, 103, 106–128.
- Emadian, S.M., Onay, T.T., & Demirel, B. (2017). Biodegradation of bioplastics in natural environments. *Waste management (New York, N.Y.)*, 59, 526–536.
- Emberton, S., Chittka, L., Cavallaro, A., & Wang, M. (2016). Sensor Capability and Atmospheric Correction in Ocean Colour Remote Sensing. *Remote Sensing*, 8, 1.
- ENVI (2002). *ENVI User's Guide. ENVI Version 3.6 December, 2002 Edition.*
- Eriksen, M., Lebreton, L.C.M., Carson, H.S., Thiel, M., Moore, C.J., Borerro, J.C., Galgani, F., Ryan, P.G., & Reisser, J. (2014). Plastic Pollution in the World's Oceans: More than 5 Trillion Plastic Pieces Weighing over 250,000 Tons Afloat at Sea. *PLoS one*, 9, e111913.
- Eriksen, M., Maximenko, N., Thiel, M., Cummins, A., Lattin, G., Wilson, S., Hafner, J., Zellers, A., & Rifman, S. (2013). Plastic pollution in the South Pacific subtropical gyre. *Marine Pollution Bulletin*, 68, 71–76.
- ESA (2018). ESA investigating detection of floating plastic litter from orbit.
https://www.esa.int/Our_Activities/Preparing_for_the_Future/Discovery_and_Preparation/ESA_investigating_detection_of_floating_plastic_litter_from_orbit.
- European Space Agency (2015). SENTINEL-2 User Handbook. European Space Agency.
<https://sentinel.esa.int/web/sentinel/user-guides/sentinel-2-msi/document-library>.
- Feygels, V., Aitken, J., Ramnath, V. (2017). Coastal zone mapping and imaging lidar (CZMIL) participation in the ocean cleanup's aerial expedition project. OCEANS 2017 - Anchorage, 1-7. Oceans MTS/IEEE conference; Marine Technology Society; Oceanic Engineering Society; OCEANS 17 Anchorage; MTS/IEEE OES OCEANS.
- Frouin, R.J., Shenoi, S.C., & Rao, K.H. (Eds.) (2016). Remote Sensing of the Oceans and Inland Waters: Techniques, Applications, and Challenges: SPIE.
- Gao, B.-C., Montes, M.J., Davis, C.O., & Goetz, A.F.H. (2009). Atmospheric correction algorithms for hyperspectral remote sensing data of land and ocean. *Remote Sensing of Environment*, 113, S17-S24.
- Garaba, S.P., Aitken, J., Slat, B., Dierssen, H.M., Lebreton, L., Zielinski, O., & Reisser, J. (2018). Sensing Ocean Plastics with an Airborne Hyperspectral Shortwave Infrared Imager. *Environmental science & technology*.
- Garaba, S.P., & Dierssen, H.M. (2018). An airborne remote sensing case study of synthetic hydrocarbon detection using short wave infrared absorption features identified from marine-harvested macro- and microplastics. *Remote Sensing of Environment*, 205, 224–235.
- Giardino, C., Brando, V.E., Gege, P., Pinnel, N., Hochberg, E., Knaeps, E., Reusen, I., Doerffer, R., Bresciani, M., Braga, F., Foerster, S., Champollion, N., & Dekker, A. (2018). Imaging Spectrometry of Inland and Coastal Waters: State of the Art, Achievements and Perspectives. *Surveys in Geophysics*, 11, 2873.
- Goddijn-Murphy, L., & Dufaur, J. (2018). Proof of concept for a model of light reflectance of plastics floating on natural waters. *Marine Pollution Bulletin*, 135, 1145–1157.
- Goddijn-Murphy, L., Peters, S., van Sebille, E., James, N.A., & Gibb, S. (2018). Concept for a hyperspectral remote sensing algorithm for floating marine macro plastics. *Marine Pollution Bulletin*, 126, 255–262.
- Goddijn-Murphy, L., & Williamson, B. (2019). On Thermal Infrared Remote Sensing of Plastic Pollution in Natural Waters. *Remote Sensing*, 11, 2159.
- Gregory, M.R. (2009). Environmental implications of plastic debris in marine settings--entanglement, ingestion, smothering, hangers-on, hitch-hiking and alien invasions. *Philosophical transactions of the Royal Society of London. Series B, Biological sciences*, 364, 2013–2025.

- Hafeez, S., Sing Wong, M., Abbas, S., Y. T. Kwok, C., Nichol, J., Ho Lee, K., Tang, D., & Pun, L. (2019). Detection and Monitoring of Marine Pollution Using Remote Sensing Technologies. In H. Bachari Fouzia (Ed.), *Monitoring of Marine Pollution*: IntechOpen.
- Hörig, B., Kühn, F., Oschütz, F., & Lehmann, F. (2001). HyMap hyperspectral remote sensing to detect hydrocarbons. *International Journal of Remote Sensing*, 22, 1413–1422.
- Hueni, A., & Bialek, A. (2017). Cause, Effect, and Correction of Field Spectroradiometer Interchannel Radiometric Steps. *IEEE Journal of Selected Topics in Applied Earth Observations and Remote Sensing*, 10, 1542–1551.
- Hueni, A., Damm, A., Kneubuehler, M., Schlapfer, D., & Schaepman, M.E. (2017). Field and Airborne Spectroscopy Cross Validation—Some Considerations. *IEEE Journal of Selected Topics in Applied Earth Observations and Remote Sensing*, 10, 1117–1135.
- Hueni, A., Nieke, J., Schopfer, J., Kneubühler, M., & Itten, K.I. (2009). The spectral database SPECCHIO for improved long-term usability and data sharing. *Computers & Geosciences*, 35, 557–565.
- Huguenin, R.L., & Jones, J.L. (1986). Intelligent information extraction from reflectance spectra: Absorption band positions. *Journal of Geophysical Research*, 91, 9585.
- Jambeck, J.R., Geyer, R., Wilcox, C., Siegler, T.R., Perryman, M., Andrady, A., Narayan, R., & Law, K.L. (2015). Marine pollution. Plastic waste inputs from land into the ocean. *Science (New York, N.Y.)*, 347, 768–771.
- Jensen, J.R. (2016). *Introductory digital image processing. A remote sensing perspective*. (4th ed.). Glenview, Ill.: Pearson Education.
- Kako, S.'i., Isobe, A., Kataoka, T., Yufu, K., Sugizono, S., Plybon, C., & Murphy, T.A. (2018). Sequential webcam monitoring and modeling of marine debris abundance. *Marine Pollution Bulletin*, 132, 33–43.
- Kako, S.'i., Isobe, A., & Magome, S. (2012). Low altitude remote-sensing method to monitor marine and beach litter of various colors using a balloon equipped with a digital camera. *Marine Pollution Bulletin*, 64, 1156–1162.
- Kataoka, T., Murray, C.C., & Isobe, A. (2018). Quantification of marine macro-debris abundance around Vancouver Island, Canada, based on archived aerial photographs processed by projective transformation. *Marine Pollution Bulletin*, 132, 44–51.
- Keshava, N., & Mustard, J.F. (2002). Spectral unmixing. *IEEE Signal Processing Magazine*, 19, 44–57.
- Kneubühler, M., Koetz, B., Nieke, J., & Schlapfer, D. (2007). *Bildspektrometrie. Skript Fernerkundung IVb*. Zürich: Remote Sensing Laboratories, Department of Geography, University of Zurich.
- Koelmans, A.A., Kooi, M., Law, K.L., & van Sebille, E. (2017). All is not lost: deriving a top-down mass budget of plastic at sea. *Environmental Research Letters*, 12, 114028.
- Kühn, F., Oppermann, K., & Hörig, B. (2004). Hydrocarbon Index – an algorithm for hyperspectral detection of hydrocarbons. *International Journal of Remote Sensing*, 25, 2467–2473.
- Kukulka, T., Proskurowski, G., Morét-Ferguson, S., Meyer, D.W., & Law, K.L. (2012). The effect of wind mixing on the vertical distribution of buoyant plastic debris. *Proceedings of the National Academy of Sciences*, 39, n/a-n/a.
- Kylili, K., Kyriakides, I., Artusi, A., & Hadjistassou, C. (2019). Identifying floating plastic marine debris using a deep learning approach. *Environmental science and pollution research international*, 26, 17091–17099.
- Lavers, J.L., Opiel, S., & Bond, A.L. (2016). Factors influencing the detection of beach plastic debris. *Marine Environmental Research*, 119, 245–251.
- Law, K.L., Morét-Ferguson, S.E., Goodwin, D.S., Zettler, E.R., Deforce, E., Kukulka, T., & Proskurowski, G. (2014). Distribution of surface plastic debris in the eastern Pacific Ocean from an 11-year data set. *Environmental Science & Technology*, 48, 4732–4738.
- Lebreton, L., Slat, B., Ferrari, F., Sainte-Rose, B., Aitken, J., Marthouse, R., Hajbane, S., Cunsolo, S., Schwarz, A., Levivier, A., Noble, K., Debeljak, P., Maral, H., Schoeneich-Argent, R., Brambini, R., & Reisser, J. (2018). Evidence that the Great Pacific Garbage Patch is rapidly accumulating plastic. *Scientific Reports*, 8, e1700782.

- Lebreton, L.C.-M., Greer, S.D., & Borrero, J.C. (2012). Numerical modelling of floating debris in the world's oceans. *Marine Pollution Bulletin*, 64, 653–661.
- Leser, H. (Ed.) (2001). *Diercke-Wörterbuch allgemeine Geographie*. (12th ed.). Braunschweig, München: Westermann; Dt. Taschenbuch-Verl.
- Li, W.C., TSE, H.F., & FOK, L. (2016). Plastic waste in the marine environment: A review of sources, occurrence and effects. *The Science of the total environment*, 566-567, 333–349.
- Lillesand, T.M., Kiefer, R.W., & Chipman, J.W. (2008). *Remote sensing and image interpretation*. (6th ed.). Hoboken, NJ: Wiley.
- Liubartseva, S., Coppini, G., Lecci, R., & Clementi, E. (2018). Tracking plastics in the Mediterranean: 2D Lagrangian model. *Marine Pollution Bulletin*, 129, 151–162.
- Louchard, E., Reid, R., Stephens, C., Davis, C., Leathers, R., Downes, T., & Maffione, R. (2002). Derivative analysis of absorption features in hyperspectral remote sensing data of carbonate sediments. *Optics express*, 10, 1573–1584.
- Mac Arthur, A., & Robinson, I. (2015). A critique of field spectroscopy and the challenges and opportunities it presents for remote sensing for agriculture, ecosystems, and hydrology. In C.M.U. Neale, & A. Maltese (Eds.), *Remote Sensing for Agriculture, Ecosystems, and Hydrology XVII* (p. 963705): SPIE.
- Mace, T.H. (2012). At-sea detection of marine debris: overview of technologies, processes, issues, and options. *Marine Pollution Bulletin*, 65, 23–27.
- Maes, T., Barry, J., Leslie, H.A., Vethaak, A.D., Nicolaus, E.E.M., Law, R.J., Lyons, B.P., Martinez, R., Harley, B., & Thain, J.E. (2018). Below the surface: Twenty-five years of seafloor litter monitoring in coastal seas of North West Europe (1992-2017). *The Science of the total environment*, 630, 790–798.
- Manolakis, D., Lockwood, R., & Cooley, T. (2016). *Hyperspectral Imaging Remote Sensing*. Cambridge: Cambridge University Press.
- Martin, S. (2014). *An Introduction to Ocean Remote Sensing*. (2nd ed.). Cambridge: Cambridge University Press.
- Maximenko, N., Chao, Y., & Moller, D. (2016). Developing a Remote Sensing System to Track Marine Debris. *Eos*.
- McElwee, K., Donohue, M.J., Courtney, C.A., Morishige, C., & Rivera-Vicente, A. (2012). A strategy for detecting derelict fishing gear at sea. *Marine Pollution Bulletin*, 65, 7–15.
- Miller, R.L. (Ed.) (2005). *Remote sensing of coastal aquatic environments. Technologies, techniques and applications*. Dordrecht: Springer.
- Milton, E.J. (1987). Principles of field spectroscopy. Review Article. *International Journal of Remote Sensing*, 8, 1807–1827.
- Milton, E.J., Schaepman, M.E., Anderson, K., Kneubühler, M., & Fox, N. (2009). Progress in field spectroscopy. *Remote Sensing of Environment*, 113, S92-S109.
- Mitchell, J.J., Glenn, N.F., Sankey, T.T., Derryberry, D.R., & Germino, M.J. (2012). Remote sensing of sagebrush canopy nitrogen. *Remote Sensing of Environment*, 124, 217–223.
- Mobley, C.D. (1999). Estimation of the remote-sensing reflectance from above-surface measurements. *Applied optics*, 38, 7442–7455.
- Morishige, C., & McElwee, K. (2012). At-sea detection of derelict fishing gear in the North Pacific: an overview. *Marine Pollution Bulletin*, 65, 1–6.
- Moroni, M., Mei, A., Leonardi, A., Lupo, E., & La Marca, F. (2015). PET and PVC separation with hyperspectral imagery. *Sensors (Basel, Switzerland)*, 15, 2205–2227.
- Moy, K., Neilson, B., Chung, A., Meadows, A., Castrence, M., Ambagis, S., & Davidson, K. (2018). Mapping coastal marine debris using aerial imagery and spatial analysis. *Marine Pollution Bulletin*, 132, 52–59.

- Odermatt, D. (2011). *Spaceborne inland water quality monitoring*. Zurich: Remote Sensing Laboratories, Department of Geography, University of Zurich.
- Pichel, W.G., Veenstra, T.S., Churnside, J.H., Arabini, E., Friedman, K.S., Foley, D.G., Brainard, R.E., Kiefer, D., Ogle, S., Clemente-Colón, P., & Li, X. (2012). GhostNet marine debris survey in the Gulf of Alaska--satellite guidance and aircraft observations. *Marine Pollution Bulletin*, *65*, 28–41.
- Potemra, J.T. (2012). Numerical modeling with application to tracking marine debris. *Marine Pollution Bulletin*, *65*, 42–50.
- Prost, G.L. (2014). *Remote sensing for geoscientists. Image analysis and integration*. Boca Raton, Florida: CRC Press.
- Qu, Y., & Liu, Z. (2017). Dimensionality reduction and derivative spectral feature optimization for hyperspectral target recognition. *Optik*, *130*, 1349–1357.
- Richards, J.A. (2013). *Remote sensing digital image analysis. An introduction*. (5th ed.). Berlin, Heidelberg: Springer.
- Richter, R., & Schläpfer, D. (2016). *Atmospheric / Topographic Correction for Airborne Imagery. ATCOR-4 User Guide, Version 7.1.0, September 2016*. DLR-IB 565-02/2016.
- Rogass, C., Spengler, D., Bochow, M., Segl, K., Lausch, A., Doktor, D., Roessner, S., Behling, R., Wetzel, H.-U., Urata, K., Hueni, A., & Kaufm, H. (2012). A Contribution to the Reduction of Radiometric Miscalibration of Pushbroom Sensors. In B. Escalante (Ed.), *Remote Sensing - Advanced Techniques and Platforms: InTech*.
- Ruiz-Orejón, L.F., Sardá, R., & Ramis-Pujol, J. (2016). Floating plastic debris in the Central and Western Mediterranean Sea. *Marine Environmental Research*, *120*, 136–144.
- Ryan, P.G. (2014). Litter survey detects the South Atlantic 'garbage patch'. *Marine Pollution Bulletin*, *79*, 220–224.
- Schaepman, M.E., Jehle, M., Hueni, A., D'Odorico, P., Damm, A., Weyermann, J., Schneider, F.D., Laurent, V., Popp, C., Seidel, F.C., Lenhard, K., Gege, P., Kuchler, C., Brazile, J., Kohler, P., Vos, L. de, Meuleman, K., Meynart, R., Schläpfer, D., Kneubühler, M., & Itten, K.I. (2015). Advanced radiometry measurements and Earth science applications with the Airborne Prism Experiment (APEX). *Remote Sensing of Environment*, *158*, 207–219.
- Siegel, D.A., Wang, M., Maritorena, S., & Robinson, W. (2000). Atmospheric correction of satellite ocean color imagery: the black pixel assumption. *Applied Optics*, *39*, 3582.
- Storrer, H.H. (1992). *Einführung in die mathematische Behandlung der Naturwissenschaften I*. Basel: Birkhäuser Basel.
- Teuten, E.L., Saquing, J.M., Knappe, D.R.U., Barlaz, M.A., Jonsson, S., Björn, A., Rowland, S.J., Thompson, R.C., Galloway, T.S., Yamashita, R., Ochi, D., Watanuki, Y., Moore, C., Viet, P.H., Tana, T.S., Prudente, M., Boonyatumanond, R., Zakaria, M.P., Akkhang, K., Ogata, Y., Hirai, H., Iwasa, S., Mizukawa, K., Hagino, Y., Imamura, A., Saha, M., & Takada, H. (2009). Transport and release of chemicals from plastics to the environment and to wildlife. *Philosophical transactions of the Royal Society of London. Series B, Biological sciences*, *364*, 2027–2045.
- Thompson, D.R., Boardman, J.W., Eastwood, M.L., Green, R.O., Haag, J.M., Mouroulis, P., & van Gorp, B. (2018a). Imaging spectrometer stray spectral response: In-flight characterization, correction, and validation. *Remote Sensing of Environment*, *204*, 850–860.
- Thompson, D.R., Gao, B.-C., Green, R.O., Roberts, D.A., Dennison, P.E., & Lundeen, S.R. (2015). Atmospheric correction for global mapping spectroscopy: ATREM advances for the HypsIRI preparatory campaign. *Remote Sensing of Environment*, *167*, 64–77.
- Thompson, D.R., Natraj, V., Green, R.O., Helmlinger, M.C., Gao, B.-C., & Eastwood, M.L. (2018b). Optimal estimation for imaging spectrometer atmospheric correction. *Remote Sensing of Environment*, *216*, 355–373.
- Thompson, R.C., Moore, C.J., Vom Saal, F.S., & Swan, S.H. (2009a). Plastics, the environment and human health: current consensus and future trends. *Philosophical transactions of the Royal Society of London. Series B, Biological sciences*, *364*, 2153–2166.
- Thompson, R.C., Swan, S.H., Moore, C.J., & Vom Saal, F.S. (2009b). Our plastic age. *Philosophical transactions of the Royal Society of London. Series B, Biological sciences*, *364*, 1973–1976.

- Topouzelis, K., Papakonstantinou, A., & Garaba, S.P. (2019). Detection of floating plastics from satellite and unmanned aerial systems (Plastic Litter Project 2018). *International Journal of Applied Earth Observation and Geoinformation*, *79*, 175–183.
- Tsai, F., & Philpot, W. (1998). Derivative Analysis of Hyperspectral Data. *Remote Sensing of Environment*, *66*, 41–51.
- van Sebille, E., Wilcox, C., Lebreton, L., Maximenko, N., Hardesty, B.D., van Franeker, J.A., Eriksen, M., Siegel, D., Galgani, F., & Law, K.L. (2015). A global inventory of small floating plastic debris. *Environmental Research Letters*, *10*, 124006.
- Vázquez-Guardado, A., Money, M., McKinney, N., & Chanda, D. (2015). Multi-spectral infrared spectroscopy for robust plastic identification. *Applied Optics*, *54*, 7396–7405.
- Venkatesan, R., Tandon, A., D'Asaro, E., & Atmanand, M.A. (Eds.) (2017). *Observing the oceans in real time*. Cham: Springer.
- Wilcox, C., van Sebille, E., & Hardesty, B.D. (2015). Threat of plastic pollution to seabirds is global, pervasive, and increasing. *Proceedings of the National Academy of Sciences*, *112*, 11899–11904.
- Worm, B., Lotze, H.K., Jubinville, I., Wilcox, C., & Jambeck, J. (2017). Plastic as a Persistent Marine Pollutant. *Annual Review of Environment and Resources*, *42*, 1–26.

PERSONAL DECLARATION

Personal declaration:

I hereby declare that the submitted thesis is the result of my own, independent work. All external sources are explicitly acknowledged in the thesis.

Weesen, 29.9.2019

J. Berthel

Place, Date

Signature